



Topological foundations of ferroelectricity

Igor A. Lukyanchuk^a, Anna G. Razumnaya^b, Svitlana Kondovych^c,
Yuri A. Tikhonov^a, Boris Khesin^d, Valerii M. Vinokur^{e,*}

^a Laboratoire de Physique de la Matière Condensée, Université de Picardie Jules Verne, Amiens, 80080, France

^b Jozef Stefan Institute, Jamova Cesta 39, Ljubljana, 1000, Slovenia

^c Institute for Theoretical Solid State Physics, Leibniz Institute for Solid State and Materials Research Dresden, Helmholtzstr. 20, Dresden, D-01069, Germany

^d Department of Mathematics, University of Toronto, 40 St. George Street, Toronto, ON M5S 2E4, Canada

^e Terra Quantum AG, Kornhausstraße 25, St. Gallen, CH-9000, Switzerland

ARTICLE INFO

Article history:

Received 27 October 2024

Accepted 17 January 2025

Available online xxxx

Editor: N. Nagaosa

Keywords:

Ferroelectrics

Topology

Vortices

Hopfions

ABSTRACT

The 21st century has witnessed a revolutionary shift in the understanding of properties of matter driven by the application of topological principles. While the traditional approach to material science has been focusing on local interactions, topology introduces a global, non-local description in which the geometry of a material profoundly influences its properties. Ferroelectric materials, with their spontaneous electric polarization, have long been essential for understanding fundamental physical phenomena, which have led to numerous practical applications. Recent discoveries have revealed that nanostructured ferroelectrics host a wealth of fundamental topological states, which effectively enrich the landscape of ferroelectric research. This Review explores the topological foundation of ferroelectricity, rooted in the electrostatic essence of these materials. Drawing upon the analogy between the hydrodynamics of incompressible fluids and the electrostatics of polarization fields, we establish a comprehensive framework for classifying the complex topological states observed in ferroelectrics. We demonstrate that the rich diversity of polarization structures can be exhaustively described using the advanced topological approach. By extending fundamental topological concepts such as helicity, fibration, foliation, and ergodicity, we offer a systematic analysis of the topological textures in ferroelectrics. This work provides a coherent framework for understanding and manipulating topological structures in nanostructured ferroelectrics, paving the way for innovations in materials science and technology.

© 2025 Terra Quantum AG. Published by Elsevier B.V. This is an open access article under the CC BY license (<http://creativecommons.org/licenses/by/4.0/>).

Contents

1. Introduction.....	3
2. Principles of topology.....	4
2.1. Topological states and spaces.....	4
2.1.1. Topological concepts.....	4
2.1.2. Topological manifolds.....	6
2.1.3. Vector fields on topological manifolds.....	7
2.2. Singularities of the vector field.....	8
2.2.1. Singular points.....	8

* Corresponding author.

E-mail address: vv@terraquantum.swiss (V.M. Vinokur).

2.2.2.	Classification of singular points.....	9
2.2.3.	Topology of singular points.....	10
2.2.4.	Poincaré-Hopf theorem.....	11
2.3.	Unit vector fields.....	12
2.3.1.	Order parameter space.....	12
2.3.2.	Vortices.....	13
2.3.3.	Skyrmions.....	14
2.3.4.	Merons.....	14
2.3.5.	Vector field tubes.....	15
2.3.6.	Real space Hopfions.....	15
3.	Ferroelectrics. Essential concepts.....	16
3.1.	Ginzburg–Landau–Devonshire approach.....	16
3.2.	Electrostatics of ferroelectrics.....	17
3.3.	Ferroelectricity versus magnetism.....	18
4.	Topological hydrodynamics of ferroelectricity.....	19
4.1.	Polarization dynamics.....	19
4.1.1.	Streamline approach.....	19
4.1.2.	Bernoulli principle.....	20
4.1.3.	Euler equation.....	21
4.2.	Polarization topological states.....	22
4.2.1.	Hopfions and vortices.....	22
4.2.2.	Handedness and helicity.....	24
4.2.3.	Polarization field in nanoparticles.....	25
4.3.	Topology of polarization streamlines.....	26
4.3.1.	Fibration. Homotopy group.....	26
4.3.2.	Linking and entanglement of streamlines.....	27
4.3.3.	Foliation and Arnold theorem.....	28
4.3.4.	Polarization singularities.....	31
5.	Extensions of topological hydrodynamics in ferroelectrics.....	32
5.1.	Perturbative approach.....	32
5.2.	Ergodicity, anisotropy, and the KAM theorem.....	33
5.3.	Electric charges in ferroelectrics.....	34
5.3.1.	Residual bound charges.....	34
5.3.2.	Intrinsic free charges.....	34
5.3.3.	Localized remanent charges.....	35
5.3.4.	Screening electrodes.....	36
5.4.	About terminology.....	37
6.	Quantification of topological states.....	37
6.1.	Numerical indicators.....	37
6.2.	Topological charges.....	38
6.3.	Application of quantification parameters.....	39
7.	From theory and simulations to experiment.....	39
7.1.	Topology of nanostructured ferroelectrics.....	39
7.2.	Nanoparticles and nanodots.....	40
7.2.1.	Simply connected nanostructures.....	40
7.2.2.	Nanoparticles.....	40
7.2.3.	Nanodots.....	42
7.3.	Nanorods and nanowires.....	42
7.4.	Heterostructures.....	44
7.4.1.	From domains to vortex matter.....	44
7.4.2.	Topological manifolds of heterostructures.....	45
7.4.3.	Vortex arrays.....	45
7.4.4.	Skyrmion bubbles.....	45
7.4.5.	Meron bubbles.....	46
7.4.6.	Labyrinths.....	46
7.5.	Bulk.....	47
8.	Conclusion.....	48
	CRediT authorship contribution statement.....	50
	Declaration of competing interest.....	50
	Acknowledgments.....	50
	Appendix A. Supplementary data.....	50
	References.....	50

1. Introduction

The 21st century inaugurated a revolution in physics launching an entirely new comprehension of matter built on topology. This development introduced and brought in the concepts of topological states, topological phase transitions, and resulted in groundbreaking discoveries of topological materials [1–3]. In a contrast to traditional approach to the description of matter that has been focusing on local interactions, the understanding of the nature of topological matter is governed by the global nonlocal fields which implies that the properties of the topological matter are shaped not only by the internal structure but also by the material's overall geometry.

Ferroelectrics, a class of materials possessing by spontaneous electric polarization, have been studied for over a century. They revealed a remarkable ability to switch polarization under an application of the external electric field. These materials have been demonstrated to be of fundamental importance for a wide range of applications, extending from capacitors to memory devices, thanks to their ability to store and control electric charge. Ferroelectrics exhibit domain structures, regions where polarization is uniformly aligned and can be reoriented by external fields. This property makes ferroelectrics a critical material for devices that base their performance on switching electrical states. Remarkably, unlike conventional dielectrics, the ferroelectrics keep their polarization even in the absence of an external field, a feature that makes them invaluable for technologies built on non-volatile memory.

The new era of ferroelectricity [4] was opened by the discovery of a rich variety of topological states in nanostructured ferroelectric materials. It was recognized that the topological nature of these ferroelectric formations arises from the nonlocal behavior of polarization fields, which makes ferroelectrics a fertile ground for the emergence of novel topological effects. In these materials, long-range electrostatic forces dominate, and the complex interplay of bound charges, stemming from polarization inhomogeneities, can destabilize long-range order. This instability leads to the formation of intricate and diverse topological states. A good example of these phenomena can be seen in ferroelectric films, where the bound charges accumulate at the sample surface where polarization lines abruptly terminate. The depolarization field associated with them creates periodic domain textures, reminiscent of the patterns first described by Landau and Kittel [5] in magnetic materials and observed further as intricate stripe domains, labyrinths, and domain bubbles [6,7].

The discovered topological states in ferroelectric heterostructures, thin films and superlattices, encompass stable domain walls [8–12], vortices [13], cylindrical and bubble domains [14], and skyrmions and skyrmion bubbles [15–20], as well as basal formations like Hopfions [21], target skyrmions [22], merons [23–25], bimerons [22], electons [26], and labyrinthine structures [22,27]. A wealth of exciting topological states was also discovered in other basic ferroelectric nanostructures [15,28], in particular, in nanoparticles [21,29–32], nanodots [16,33–36], and nanorods [37–41]. These findings have significantly expanded the landscape of ferroelectricity, demonstrating the diversity and complexity of topological phenomena in nanoscale ferroelectric materials.

There have been excellent reviews that have provided comprehensive pictures of both the experimental and theoretical progress in the field of ferroelectrics [4,42–51]. These works have systematized the current knowledge by applying basic topological principles, often adapted from magnetic systems. These reviews have made significant contributions to the general understanding of topology in ferroelectrics, yet there remains a strong need for a targeted and in-depth description of the topological phenomena that are specific to ferroelectric systems. This includes addressing the unique electrostatic characteristics of ferroelectrics and using the advanced theoretical approaches, which our Review will provide.

The primary objective of our Review is to utilize the fundamental concepts of topology specific to ferroelectrics that remain underexplored. We build upon and further develop a generic topological foundation of ferroelectricity, rooted in its electrostatic essence. Leveraging the topological identity between the hydrodynamics of incompressible fluids and the laws of electrostatics, we apply the fundamental mechanisms of topological hydrodynamics to constructing and reviewing a coherent theoretical framework for ferroelectrics. This allows us to present a comprehensive classification of polarization structures in ferroelectrics, demonstrating that their rich diversity can be fully understood through fundamental topological formations, including vortices and Hopfions.

By extending concepts like topological helicity, fibration, foliation, ergodicity, and entanglement which are widely applied in differential topology, high-energy physics and magneto-hydrodynamics, but were rarely explored in condensed matter physics, our Review offers a systematic analysis of topological textures in ferroelectrics. We not only synthesize existing knowledge but also highlight emerging experimental systems and potential applications in nanostructured ferroelectrics, such as nanoparticles, nanorods, and composite materials. This comprehensive perspective on the role of topology in ferroelectrics introduces innovative approaches for interpreting, manipulating, and applying topological structures, which are indispensable for advancing theoretical understanding and practical developments in this promising field.

The Review is organized as follows.

In Section 2 we present a comprehensive overview of the topological principles commonly employed in condensed matter physics and discuss how these concepts are adapted to ferroelectricity. We examine the key topological categories, including manifolds and vector fields, and their singularities. Additionally, we explore the homotopy group approach for classifying topological states, using magnetic systems as an example, and explain to what extent this method can be applied to polarization fields in ferroelectrics.

In Section 3 the key principles of ferroelectricity are reviewed, starting with the Ginzburg–Landau–Devonshire theory which is the principal analytical tool for exploring the topology in ferroelectrics. This Section covers the role of

depolarization effects in destabilizing uniform states and in how topological structures like domains form to reduce the depolarization energy. A comparison between ferroelectricity and magnetism highlights the unique topological challenges in each system.

Section 4 is central for reviewing the topological foundations of ferroelectricity. The core concept of the topological approach to polarization dynamics in nanostructured ferroelectrics involves minimizing large depolarization contributions, which critically influence the stability of polarization structures. A key element of this approach, which is similar to the approach to the topology of incompressible fluids, is the treatment of ferroelectric polarization as an analogue to the streamlines of ideal fluid flow where polarization fields are viewed as continuous, non-terminating fluxes. Building on the theoretical framework of topological hydrodynamics introduced by Vladimir Arnold [52] and applying it to exemplary ferroelectric nanostructures, the divergenceless nature of polarization fields gives rise to key topological characteristics, such as handedness, helicity, vibration foliations, and entanglement. These features are fundamental for understanding the complex polarization formations in nanostructured ferroelectrics, which are crucial in determining their physical properties.

In Section 5 we further expand the formalism of topological hydrodynamics to explain how the topology of ferroelectric systems evolves under specific perturbations, including anisotropic effects, elastic energy, and electrostatic interaction with external charges and electrodes. These perturbations drive the system away from the ideal state described by topological hydrodynamics. The chapter explores Kolmogorov–Arnold–Moser (KAM) theorem asserting that topological states of divergence-free vector fields remain structurally intact and topologically stable as long as perturbative forces remain moderate. This theorem serves as a foundation for analyzing how polarization textures in ferroelectrics persist or reconfigure under varying degrees of external influence.

Section 6 presents methods for quantifying topological states in confined ferroelectrics, particularly within nanostructured systems. It introduces key numerical parameters, such as swirling, chirality, and topological charges, which are used to characterize complex polarization phenomena. These quantification tools are crucial for analyzing and understanding the intricate topological states at the nanoscale. Furthermore, they are essential for applying the topological approach to ferroelectrics in practical applications, enabling precise control over polarization configurations in advanced ferroelectric devices.

Section 7 explores the manifestation of topological states in specific ferroelectric nanostructures, illustrating key concepts of the topological approach to ferroelectrics. We review how the shape and geometries of confined systems like nanoparticles, nanorods, thin films, heterostructures, and bulk materials influence the formation of topological states in these systems. Special emphasis is given to the added complexity in multi-connected topologies, which makes a significant impact on polarization behavior and stability. This section, like the entire Review, does not aim to provide a comprehensive account of the rapidly advancing achievements in experimental and modeling research on the specific properties of nanostructured ferroelectrics. A detailed and up-to-date review of the field can be found in the extensive works cited at the beginning of the Introduction. Our objective here is to highlight key and reliable findings from both experimental and theoretical research, using them to illustrate the core principles of the topological description presented in our Review.

In conclusion, Section 8 summarizes the key findings of the Review and discusses potential applications of the topological framework in emergent technologies, particularly in nanotechnology and advanced materials science.

Building on the available experimental and theoretical studies, and to present a comprehensive 3D panorama of the emerging states, we complement the existing data by integrating them with phase-field simulations of ferroelectric systems, specifically conducted for this Review. Details of these simulations are provided in the Supplemental Material.

2. Principles of topology

2.1. Topological states and spaces

2.1.1. Topological concepts

Topological concepts have been developed to describe and classify the complex structures found in various condensed matter systems. Historically, the first states treated in terms of topology were structural defects, namely, dislocations in solids [53] and disclinations and vortices in liquid crystals [54,55] and in multicomponent superfluid ^3He [56]. In general, topological states appear in systems possessing a symmetrical order, which is usually described by the physical quantity called the order parameter. The order parameter can be either a real or complex number, a vector, or a tensor of an arbitrary rank. A remarkable illustration of the application of topological concepts and ideas in condensed matter physics for the description of spacial structures is presented by exemplary works [57,58] which straightforwardly explore rigorous topological concepts developed in classical topological textbook [59].

Considerations of topological states are based on the comparison of fundamental spaces, commonly referred to as manifolds. Fig. 1 illustrates typical manifolds, their interrelations, and the topological properties of the vector fields that arise on them. In the following sections, we examine in detail the characteristics and structure of these manifolds, as well as the properties of the vector fields defined on these manifolds.

The first fundamental space that we consider is the order parameter space D , a manifold that parametrizes various states of a multi-component order parameter based on specific criteria relevant to the problem. Typically, D forms a subset

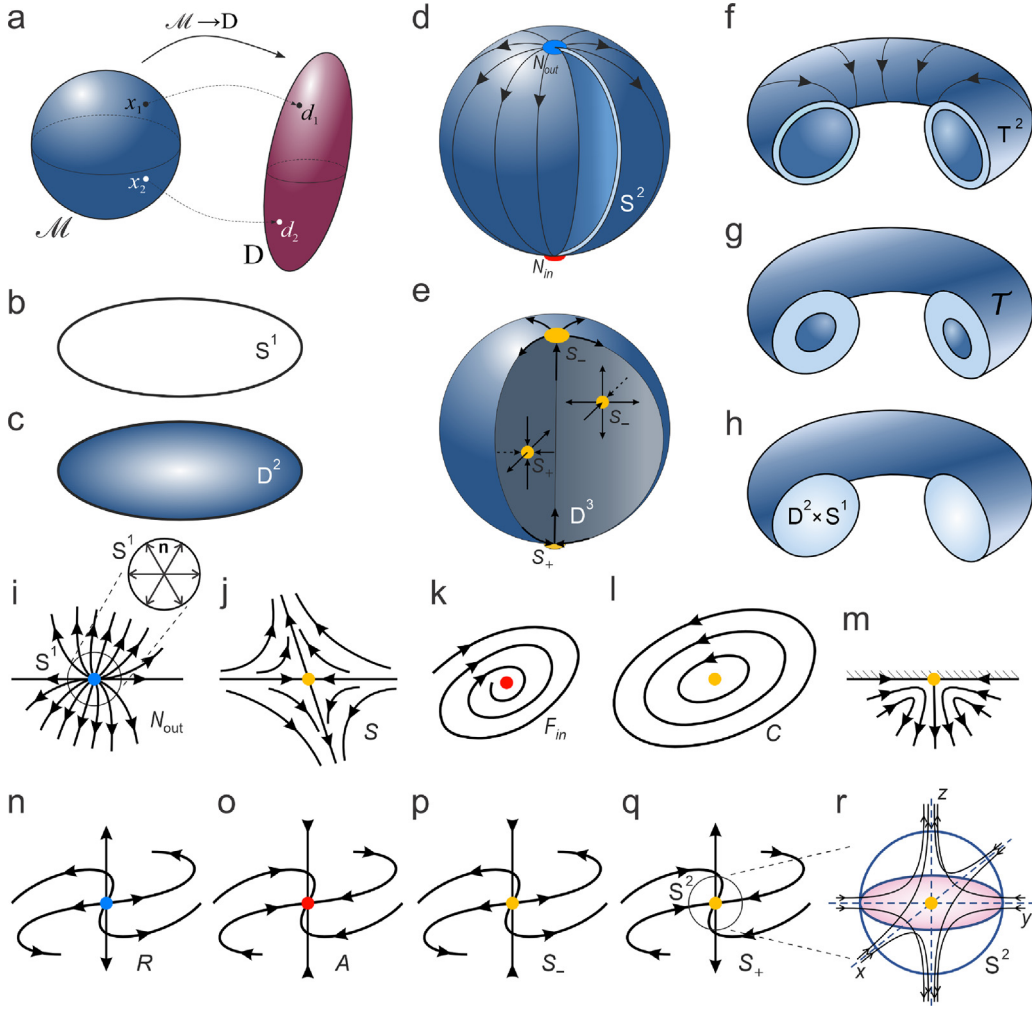


Fig. 1. Topological manifolds and vector field singularities. (a) Homotopy group mapping between the coordinate space and order parameter space, illustrating topological classifications. (b) 1D circle S^1 , a closed manifold with no boundary. (c) 2D disk D^2 , a manifold with a circular boundary, S^1 . (d) 2D sphere S^2 , a closed manifold with no boundary, commonly used to represent the surface of a 3D simply connected object. (e) 3D ball D^3 , a manifold with a spherical boundary S^2 , representing confined simply connected topological structures, such as those in ferroelectric nanoparticles. (f) 2D torus T^2 , a closed manifold without boundaries. (g) 3D toroidal shell \mathcal{T} , a manifold with two boundaries (inner and outer tori), used to model films with periodic topological textures. (h) 3D solid torus $D^2 \times S^1$, a manifold with a toroidal boundary T^2 , representing systems like nanorods with periodic topological textures. (i) 2D unstable node N_{out} , a singular point where the vector field diverges outward the point. The upper sketch demonstrates the topological characterization of this singularity through the winding of the surrounding vector field. (j) 2D saddle point S , a point where the vector field both converges and diverges. (k) 2D focus F_{in} , a point where the vector field spirals inward. (l) 2D center C , a vector field configuration where vectors circulate around a central singular point, forming a vortex. (m) A singularity at the surface where the vector field terminates, influencing both surface and bulk field configurations. (n) 3D repelling point R , a singularity where the vector field diverges outward from a central point. (o) 3D attracting point A , a singularity where the vector field converges inward toward a central point. (p) 3D saddle point type S_- , a singularity where the field converges along one direction and diverges along two others. (q) 3D saddle point type S_+ , a singularity where the field converges along two directions and diverges along one. (r) The topological characterization of singular point S_+ . Singular points with converging and diverging vector fields are shown in red and blue, respectively. Divergence-free singular points are shown in yellow.

of a larger manifold, encompassing all possible states of the order parameter, with its dimensionality reduced to capture only the relevant physical or symmetry-related states. In many cases, D represents the space of order parameter states that share the same or nearly identical energy, such as in ferromagnetic or liquid crystal systems, where the states of similar energy form continuous families due to rotational or gauge symmetries.

The next space is the coordinate manifold \mathcal{M} , a subspace of the system space \mathbb{R}^n , in which the order parameter is defined. Here, $n = 1, 2, 3$ represents the dimensionality of the space of the system, which could correspond to a three-dimensional (3D) space of a bulk crystal or confined particle, a two-dimensional (2D) space of a thin film, or a one-dimensional (1D) space of a wire. Within the manifold \mathcal{M} , the order parameter is non-uniformly distributed, taking specific values which correspond to a point on the order parameter space D .

The classification of topological textures involves mapping the coordinate space \mathcal{M} onto the order parameter space D , $\mathcal{M} \rightarrow D$, as sketched in Fig. 1(a). The homotopy group approach is used to classify these mappings by considering how the coordinate space \mathcal{M} can wrap around D and by identifying distinct topological configurations that cannot be continuously transformed into one another. For instance, in magnetic systems with vortices or skyrmions, where the order parameter is represented by a unit vector, the homotopy group assigns an integer expressing a topological charge or a set of such integers to describe how many times the coordinate space wraps around the order parameter space. We introduce these systems as exemplary applications of the homotopy group approach in Section 2.3. The topological treatment of ferroelectric systems requires an even more advanced method, which explores the order parameter space for divergenceless fields. This approach, utilizing elements of topological hydrodynamics, will be presented in Section 4 and will be used throughout the most of our Review.

2.1.2. Topological manifolds

The properties of topological manifolds are crucial for understanding the complex interplay between their inherent structure and the resulting properties of the condensed matter systems, particularly the properties of the polarization field confined in ferroelectric nanostructures. In this Review, we consider several typical manifolds representing order parameter spaces, specifically circles S^1 , disks D^2 , and spheres S^2 , as illustrated in panels (b), (c), and (d) of Fig. 1, respectively.

We also explore the coordinate manifolds, hosting topological states, balls D^3 , panel (e), tori T^2 , panel (f), toroidal shells \mathcal{T} , panel (g), solid tori $D^2 \times S^1$, panel (h), 3D tori T^3 , and 3D sphere S^3 . The last two manifolds are not shown in Fig. 1. The 3D torus, T^3 , is the cube with opposite faces joined in pairs, while the 3D sphere, S^3 , is the ball D^3 in which all points of its boundary, 2D sphere, are glued together. As further discussed in Section 7, the coordinate manifolds D^3 , $D^2 \times S^1$, \mathcal{T} , and T^3 are appropriate coordinate manifolds for describing ferroelectric nanoparticles, nanorods, films, and superlattices, respectively.

It is important to note that certain nanostructures, which differ geometrically from those shown in Fig. 1, belong to the same topological classes. This similarity arises because, using continuous deformations, these nanostructures can be transformed into one another without compromising their integrity. For example, cylindrical and cubic nanoparticles, as well as those of irregular shapes, are topologically equivalent to the three-dimensional ball D^3 . Here, we outline the key topological characteristics of these manifolds, that are also summarized in Table 1.

Dimensionality of a manifold refers to the number of independent parameters needed to describe a point within the manifold, indicating whether the manifold is one-dimensional, 1D, (lines), two-dimensional, 2D, (surfaces), or three-dimensional, 3D, (volumes).

Boundaries of a manifold are features of those topological manifolds that have borders. The boundaries are themselves manifolds having the dimensionality which is by 1 (one) lower than the dimensionality of the manifold they bind. The boundaries play crucial roles in defining the properties of the manifold, particularly in materials where boundary effects are significant. The boundary of a manifold \mathcal{M} is denoted by the symbol $\partial\mathcal{M}$. For example, the boundary of a 2D disk is a 1D circle, $S^1 = \partial D^2$, and the boundary of a 3D ball is the 2D sphere, $S^2 = \partial D^3$. The 3D solid torus has a 2D toroidal boundary, $T^2 = \partial(D^2 \times S^1)$, while the 3D toroidal shell \mathcal{T} has two boundaries, an internal and an external ones, both of which are 2D tori T^2 . Notably, the 1D circle, S^1 , 2D and 3D spheres, S^2 and S^3 , and 2D and 3D tori, T^2 and T^3 , have no boundaries. Such manifolds are referred to as *closed manifolds*. The absence of the boundary is denoted as $\partial\mathcal{M} = \emptyset$.

An essential property of the manifolds describing nanoparticles is that they are *bounded manifolds*, meaning they are confined within a finite region of space. Ferroelectric nanorods, films, and superlattices are examples of *unbounded manifolds*, as they extend infinitely in at least one direction. Nevertheless, as we demonstrate in Sections 7.3 and 7.4, when the polarization distribution is periodic, their behavior can be effectively mapped onto bounded manifolds.

Connectivity of a manifold describes and refers to how points within the manifold are connected. A simply connected manifold is the one where any closed loop can be contracted to a single point, indicating no “holes” or “handles”. For example, a two-dimensional sphere, S^2 , is simply connected. A multiply connected manifold, like a torus T^2 , has independent paths or loops that cannot be contracted to a single point without leaving the manifold. The torus is multiply connected because it has a handle, creating independent loops that cannot be reduced to a point, reflecting its topological complexity.

The *Euler characteristic*, χ_E , of a manifold is an important topological invariant intrinsically linked to its connectivity. It describes the structure of the manifold, providing a numerical representation of the manifold's topological complexity, capturing information about the number of holes, handles, and disconnections. It remains unchanged under deformations of the manifold that do not involve tearing or cutting. The Euler characteristic of a sufficiently smooth manifold is a topological invariant that is calculated using triangulation, which is the process of dividing the manifold into simple elements, such as triangles in the two-dimensional case or tetrahedra in the three-dimensional case. For a smooth two-dimensional manifold, the Euler characteristic is calculated using the formula $\chi_E = V - E + F$, where V is the number of vertices in the triangulation, E is the number of edges, and F is the number of triangles (faces) in the triangulation. For instance, for a sphere triangulated into 4 triangles (like a tetrahedron), we have $V = 4$, $E = 6$, and $F = 4$. Substituting into the formula gives $\chi_E = 4 - 6 + 4 = 2$. For a 3D manifold, χ_E is calculated using volumetric triangulation. The formula is $\chi_E = V - E + F - C$, where V is the number of vertices, E is the number of edges, F is the number of triangular faces, and C is the number of tetrahedral cells.

Table 1

Topological characteristics of typical manifolds \mathcal{M} , their mathematical expressions, dimensionality, \dim , their boundary, $\partial\mathcal{M}$ (where the symbol \emptyset denotes closed manifolds with no boundary), genus, g , and ferroelectric nanostructures, described by these manifolds.

\mathcal{M}	\dim	$\partial\mathcal{M}$	g	χ_E	Nanostructure
Circle S^1	1	\emptyset		0	
Disk D^2	2	S^1	0	1	
Sphere S^2	2	\emptyset	0	2	
Torus $T^2 = S^1 \times S^1$	2	\emptyset	1	0	
Ball D^3	3	S^2		1	Nanoparticle
Solid torus $D^2 \times S^1$	3	T^2		0	Nanorod
Toroidal shell \mathcal{T}	3	$2 \times T^2$		0	Film
3D Torus $T^3 = S^1 \times S^1 \times S^1$	3	\emptyset		0	Superlattice
3D Sphere S^3	3	\emptyset		0	

The genus of a 2D surface, in particular of the boundary of a 3D manifold, is a topological property that represents the number of handles or holes in a manifold. For example, a sphere has a genus $g = 0$, meaning it has no handles or holes, while a torus has a genus $g = 1$, indicating it has one handle. The genus is mathematically related to the Euler characteristic χ_E of the surface by the formula $\chi_E = 2 - 2g - b$, where b is the number of boundary components in the case of the surface with boundaries. In this Review, we consider only *oriented surfaces* in which a consistent direction or normal vector can be smoothly defined across the entire surface, assigning an “inside” and “outside” directions everywhere.

2.1.3. Vector fields on topological manifolds

Vector order parameters, such as polarization \mathbf{P} in ferroelectric materials, and magnetization \mathbf{M} in magnetic materials, are essential for describing phase transitions in these systems. They determine the level of order, symmetry breaking, and the nature of the phase transition. The introduction of vector order parameters also enables the study of topological phenomena, such as domain walls, vortices, skyrmions, and Hopfions, particularly in nanostructured materials. In this and the following sections, we discuss the general structure of the vector fields, \mathbf{V} , focusing on how they are described and decomposed into fundamental components while considering the specific topology of the coordinate manifolds on which the vector fields are defined, how the singularities and topological states arise in these fields, and how the local, differential, characteristics of the fields are related to the global, topological, characteristics of the fields and coordinate manifolds.

Two key differential operations are used to characterize the local inhomogeneities of vector fields: *divergence* and *curl* (or rotor) of the field. The divergence of a vector field, denoted as $\nabla \cdot \mathbf{V}$ or $\text{div}\mathbf{V}$, is a scalar quantity that measures the amount of the flux of the field that spreads out from a point or converges toward a point. A positive divergence indicates a source, from which the vector field is spreading out, while a negative divergence indicates a sink, where the field converges. In fluid dynamics, as well as in ferroelectric and magnetic systems, this operation is crucial for understanding the behavior of vector fields in relation to sources and sinks within the system. In nematic liquid crystals [54], characterized by the unit director field \mathbf{n} , representing the orientation of rod-like molecules, the term $\text{div}\mathbf{n}$ corresponds to splay deformation. This deformation occurs when the molecules experience a divergence in their alignment, causing the angle between adjacent directors to change and the molecules to spread apart from one another.

The curl (or rotor) of a vector field, denoted as $\nabla \times \mathbf{V}$, $\text{curl}\mathbf{V}$, (or $\text{rot}\mathbf{V}$), is a vector quantity that measures the rotation or circulation of the field around a point. It helps to determine whether, and to what extent, the field exhibits local twisting. In fluid dynamics, ferroelectric, and magnetic systems, the curl plays a crucial role in describing vortex-like structures. In nematic liquid crystals, the curl helps distinguish between two fundamental swirling distortions of the rod-like molecules: twist distortion, where the molecules rotate around an axis perpendicular to their alignment direction, and bend distortion, where the vector field characterizing the molecular orientation curves, causing adjacent molecules to bend toward or away from each other. These distortions are characterized by the terms $\mathbf{n} \cdot [\nabla \times \mathbf{n}]$ for twist and $\mathbf{n} \times [\nabla \times \mathbf{n}]$ for bend, respectively.

Curl-free and divergence-free vector fields play a fundamental role in various areas of physics. Curl-free fields, \mathbf{V}_d , characterized by relation $\nabla \times \mathbf{V}_d = 0$, can typically be expressed in terms of a scalar potential φ , such that $\mathbf{V}_d = -\nabla\varphi$. A classic example of a curl-free field is the electrostatic field, which is irrotational because it can be described as the gradient of an electric potential. The absence of vorticity in curl-free fields is crucial for describing potential flows in fluid dynamics, where the fluid moves smoothly without forming vortices. Divergence-free fields, \mathbf{V}_v , defined by the condition $\nabla \cdot \mathbf{V}_v = 0$, are essential in systems governed by conservation laws, such as the conservation of mass or charge. These fields are often represented as the curl of a vector potential \mathbf{A} , such that $\mathbf{V}_v = \nabla \times \mathbf{A}$. A well-known example of a divergence-free field is the solenoidal magnetic field, where the absence of magnetic monopoles ensures that magnetic field lines form closed loops. Similarly, the condition of incompressibility in fluid dynamics leads to a divergence-free velocity field, which ensures that the mass of the fluid is conserved as it flows, reflecting the fundamental principle of mass conservation. As outlined in this Review, the divergence-free component of the polarization vector \mathbf{P} is crucial for understanding the topological states in nanostructured ferroelectrics.

A powerful and widely used method for analyzing vector fields is the Helmholtz decomposition [60]. The Helmholtz theorem states that any sufficiently smooth vector field can be decomposed into the sum of a curl-free component and a divergence-free component, represented as the gradient of a scalar potential and the curl of a vector potential, respectively:

$$\mathbf{V} = \mathbf{V}_d + \mathbf{V}_v = -\nabla\varphi + \nabla \times \mathbf{A}. \quad (1)$$

This decomposition is highly useful in physics, particularly in areas such as fluid dynamics and electromagnetism, as it allows the separation of vector fields into components with distinct physical properties. The curl-free part corresponds to sources and sinks, while the divergence-free part corresponds to rotational behavior, distinguishing the vortex matter. This decomposition enables a clear understanding and modeling of complex systems described by the vector fields. The Helmholtz decomposition of the polarization field $\mathbf{P}(\mathbf{r})$ is of great importance in ferroelectrics, as the divergent part of the polarization field corresponds to the formation of so-called dipole bound charges, which are energetically unfavorable. That is why, as will be discussed further in Section 3.2, the divergent part of $\mathbf{P}(\mathbf{r})$ tends to decrease. The decomposition (1) allows for the separation of the energetically unfavorable (small) divergent component from the divergence-free curled component, enabling an analysis of the underlying physical processes governing the polarization behavior in ferroelectric materials.

It is important to note that the standard formulation of the Helmholtz theorem typically applies to vector fields that either decay rapidly in space or are confined within simply connected manifolds. When dealing with more complex topologies, such as multiply connected manifolds, the Helmholtz decomposition is generalized into the broader *Helmholtz–Hodge decomposition* [61]. In this extension, an additional component, the *harmonic field* \mathbf{V}_h , is introduced alongside the basic divergence-free field \mathbf{V}_d with non-zero curl and the curl-free field \mathbf{V}_v with non-zero divergence. The harmonic field, which is simultaneously curl-free and divergence-free, satisfies the conditions $\nabla \cdot \mathbf{V}_h = 0$ and $\nabla \times \mathbf{V}_h = 0$. The structure of \mathbf{V}_h strongly depends on the connectivity of the manifold, and its behavior reflects the topological characteristics of the space. As an example, in Section 7.3 we will demonstrate the emergence of the harmonic field in ferroelectric nanorods, which are described by a doubly connected manifold of a solid torus $D^2 \times S^1$. This field circulates around the torus and is both curl-free and divergence-free.

Inhomogeneities in the vector field can give rise to specific points where the field's amplitude drops to zero. These points, known as singularities, are crucial elements that shape the global structure of the field. In the following Section, we classify these singularities and explore their connection to the overall topology of the field. Hereafter we move on to the topological properties of specific vector fields constrained by particular physical conditions. In Section 2.3, we illustrate the application of the topological homotopy group approach to the description of vector fields with fixed amplitude. This approach, widely used in solid-state physics, is commonly applied to vector fields in magnetic materials and nematic liquid crystals, where the order parameter is a unit vector. Although it can to some extent be applied to ferroelectrics to describe the qualitative behavior of the polarization vector, it does not fully account for the additional, already mentioned, topological constraint – the vanishing of the divergence component of the polarization vector field in these materials. The topological description of divergence-free vector fields goes beyond the usual theories of homotopy groups and requires more advanced methods. These methods have been developed in topological hydrodynamics, which deals with divergence-free fluid flows [52]. We will rely on this approach throughout the Review when exploring the topology of polarization fields in ferroelectrics.

2.2. Singularities of the vector field

2.2.1. Singular points

Singular points are the points where the vector field is either undefined or its value is zero. Singular points serve as markers of the vector field, through which the structure of the entire field in the manifold can be understood. Studying these points in mathematics is essential for the classification of fields and qualitative analysis of solutions of differential equations [59,62]. The approach based on the analysis of singularities is widely applied in traditional physics disciplines such as fluid dynamics, electromagnetism, and plasma physics [52,63].

In hydrodynamics, singular points correspond to locations of vortices or stagnation points. In electrodynamics, these points indicate charge-induced sources or sinks of an electric field. They correspond to the null saddle points in magnetic fields, crucial in plasma physics and magnetohydrodynamics, particularly in the design and operation of tokamak devices for fusion research, where they impact plasma confinement and stability. Singularities in the magnetic field distribution, referred to as Bloch points, have been actively studied in magnetism [64–70]. As magnetic nanotechnology advances toward more intricate three-dimensional structures, the importance of these 3D magnetization configurations – particularly in cylindrical magnetic nanowires, nanoparticles, and thick asymmetric circular dots – is anticipated to grow significantly over time [71–76]. Notably, the dynamics of singular points have been shown to play a crucial role in switching phenomena and the motion of domain walls in magnetism [77]. Although singular Bloch-like points have been predicted in ferroelectric systems [78–82], observing them in practice remains challenging due to their extremely small sizes. Here, we outline the fundamental topological properties of singular points in arbitrary vector fields and detail their application to the polarization field in ferroelectrics later in the Review.

Table 2
Properties of the 2D vector field singular points.

Singularity	Eigenvalues $\lambda_{1,2}$ ^a	Ind ₂	Description
$N_{in}(N_{out})$, Stable (unstable) node	$\lambda_{1,2}$ are both negative (positive) real numbers.	+1	The vector field converges into (diverges out from) the point.
S, Saddle point	$\lambda_{1,2}$ are both real numbers with opposite signs	−1	The vector field has both attraction and repulsion directions.
$F_{in}(F_{out})$, Stable (unstable) focus	$\lambda_{1,2}$ are complex conjugated numbers with negative (positive) real parts	+1	The vector field spirals inward (outward) towards the point.
C, Center	$\lambda_{1,2}$ are both imaginary numbers	+1	The vector field rotates around the point, forming the vortex

^a Either both eigenvalues are real or complex conjugates; $\lambda_1\lambda_2 \neq 0$.

Talking about the entire set of singular points in a vector field, it is important to distinguish non-degenerate singularities, which serve as the fundamental building blocks of singularities. Mathematically, any complex singularity can be decomposed into these non-degenerate singular points, as they provide the local structure around which more intricate singular behaviors can be understood. Below we will assume the singular points to be non-degenerate. Then, importantly, they are stable under small variations of the field, serving as key elements in topology that significantly impact the overall field structure. It should also be noted that linear singularities, such as singular lines in the cores of vortex formations can exist in vector fields. However, these linear singularities are topologically unstable, meaning they can be transformed into a set of isolated singular points through small variation of the field. What can stabilize them are specific symmetry requirements of the system or other physical constraints. In Section 4.3.4, we will examine the formation of linear vortex-like singularities in ferroelectrics, governed by specific energetic constraints.

2.2.2. Classification of singular points

In differential topology, the properties of a non-degenerate singular point in a vector field V_i are characterized by the non-degenerate Jacobi matrix of the spatial derivatives of V_i at that point, $J_{ij} = \partial_j V_i$ [59]. The eigenvalues λ_i of the Jacobi matrix characterize the local behavior of the field near this point. The index of the point is determined by the sign of the determinant:

$$\text{Ind}_k = \text{sgn det } \|\partial_i V_j\| = \text{sgn} \prod_i \lambda_i, \quad (2)$$

where the subscript k represents the dimensionality of the space.

When analyzing polarization fields, we are interested in their behavior both on the surface and within the volume of manifolds of nanostructures. Consequently, we need to classify possible types of singularities in 2D and in 3D coordinate spaces.

In the 2D case, we focus on the relevant to ferroelectrics configuration, in which the polarization is tangential to the nanostructure's surface, see Section 3.2. This reduces the classification to the singular points of a 2D vector field, located within 2D coordinate plane. The possible 2D singular points, along with their eigenvalues, indices, and properties, are listed in Table 2. The configurations of the vector field near typical points – unstable node (N_{out}), saddle point (S), stable focus (F_{in}), and center (C) – are illustrated in panels (i) through (l) of Fig. 1, respectively.

Singularities on the surface exhibit a dual nature, as depicted in panels (d) and (e) of Fig. 1, where we use the singular points at the poles of the ball's surface as an example. On one hand, they can be characterized as singular points of a 2D surface field, as discussed earlier. On the other hand, as shown in Fig. 1(m), they influence the 3D field structure beneath the surface and can be classified as 3D objects. Historically, David Mermin referred to such surface singularities, in reference to surface topological defects in superfluid ^3He , as boojums [83], a term borrowed from Lewis Carroll's poem “The Hunting of the Snark”. This terminology has also been used to describe surface defects in nematic liquid crystals [84], but is rarely employed in the context of magnetism or ferroelectrics. The topological interplay between surface and bulk singularities is discussed further in Section 2.2.4.

Similarly to the 2D case, the classification of 3D singular points is based on analyzing the eigenvalues of the Jacobian matrix, now consisting of three nonzero values: λ_1 , λ_2 , and λ_3 . The typical singular points – repelling point R, attracting point, A, and saddle points, S_- and S_+ – are summarized in Table 3 and illustrated in panels (n)–(q) of Fig. 1, respectively.

To conclude here, by referencing the given in Tables 2 and 3 eigenvalues, indices, and descriptive behaviors of the polarization fields near the singular points, it is possible to predict the behavior of polarization vectors around these points. As we explain in the next Section, this understanding, when aligned with knowledge of the topological structure of the coordinate manifold, is crucial for decoding complex field behaviors into more comprehensible patterns, thereby facilitating a deeper insight into the overall polarization dynamics within the nanostructure.

Table 3
Properties of the 3D vector field singular points.

Singularity	Eigenvalues $\lambda_{1,2,3}$ ^a	Ind ₃	Description
R, Repelling point	Re $\lambda_{1,2} \geq 0$, $\lambda_3 > 0$ is real number	+1	The vector field diverges from the point. In the specific case when $\lambda_{1,2}$ are both imaginary numbers, the vector field diverges along the direction defined by λ_3 and forms the 2D center (vortex) within the plane, defined by $\lambda_{1,2}$.
A, Attracting point	Re $\lambda_{1,2} \leq 0$, $\lambda_3 < 0$ is real number	−1	The vector field converges into the point. In the specific case when $\lambda_{1,2}$ are both imaginary numbers, the vector field converges along the direction defined by λ_3 and forms the 2D center (vortex) within the plane, defined by $\lambda_{1,2}$.
S ₊ , Saddle point	Re $\lambda_{1,2} < 0$, $\lambda_3 > 0$ is real number	+1	The vector field diverges from a point along the axis defined by λ_3 , while simultaneously converges to this point across a perpendicular plane defined by $\lambda_{1,2}$ exhibiting either a 2D stable node N_{in} or a stable focus F_{in} within this plane.
S _− , Saddle point	Re $\lambda_{1,2} > 0$, $\lambda_3 < 0$ is real number	−1	The vector field converges towards a point along the axis defined by λ_3 , while simultaneously diverges from this point across a perpendicular plane defined by $\lambda_{1,2}$, exhibiting either a 2D unstable node N_{out} or a unstable focus F_{out} within this plane.

^a Either all three eigenvalues are real, or one of them is real and other two are complex conjugates; $\lambda_1\lambda_2\lambda_3 \neq 0$.

2.2.3. Topology of singular points

We provide further details concerning the topological stability of singular points, showing that the field singularity, characterized by the point's index, remains unchanged under small field variations. Specifically, using the outlined in Section 2.1.1 homotopy group approach, we show that the indices of singular points can be determined through the global field behavior in their vicinity. We consider 2D and 3D cases separately.

The topological characterization of a singular point in the 2D vector field \mathbf{V} on a 2D coordinate manifold is illustrated in Fig. 1(i), with the singular unstable node N_{out} as an example. We encircle the point N_{out} with a closed contour l and traverse it, making a full turn in the coordinate space of the 2D manifold. During this loop, the unit vector of the normalized field, $\mathbf{n} = \mathbf{V}/V$, also completes a full rotation. Topologically, this procedure is described by f_1 mapping $S^1 \xrightarrow{f_1} S^1$ of the coordinate space S^1 of the closed contour l onto the circle manifold S^1 , representing the space of the tips of the normalized vector \mathbf{n} . The degree of the mapping is determined by the number of full rotations of the vector \mathbf{n} around the contour l , and is given by

$$\deg f_1 = \frac{1}{2\pi} \oint_l \mathbf{z} \cdot [\mathbf{n} \times \partial_l \mathbf{n}] = \frac{1}{2\pi} \oint_l \frac{\partial \varphi}{\partial l} dl. \quad (3)$$

Here, the integration is done over the contour l , encircling the singular point, dl is the element of the length of this contour, φ is the azimuthal angle of \mathbf{n} , and \mathbf{z} is the unit vector perpendicular to the 2D plane of the system. Importantly, $\deg f_1$ is an integer that remains constant under small variations of the contour l or minor deformations of the vector field \mathbf{V} . This invariance guarantees the stability of the singular point, a property known as topological protection.

The topological characterization of singular points in 3D case is similar. We exemplify it for the saddle point of type S₊, as shown in panels (q) and (r) in Fig. 1. Let S^2 be a closed sphere centered at S_2 that is pierced by the vector field \mathbf{V} . Consider now the map of S^2 onto the space of the tips of the normalized vector $\mathbf{n} = \mathbf{V}/V$ which is now a 2D sphere S^2 . In this f_2 mapping, $S^2 \xrightarrow{f_2} S^2$, each point of S^2 has an image on S^2 representing the direction of \mathbf{n} at the selected point. The

mapping f_2 is characterized by the degree of the mapping calculated as

$$\deg f_2 = \frac{1}{8\pi} \int_{S^2} \mathbf{F} \, d\mathbf{s}, \quad (4)$$

where $d\mathbf{s}$ is the vector element of the integration surface and \mathbf{F} represents the divergence-free vector field given by

$$F_i = \epsilon_{ijk} \mathbf{n} \cdot \left[\frac{\partial \mathbf{n}}{\partial x_j} \times \frac{\partial \mathbf{n}}{\partial x_k} \right], \quad \text{div } \mathbf{F} = 0. \quad (5)$$

This field is commonly known as the topological Sine–Gordon current in field theory [85] and as the gyrovector density in magnetic literature [86–89]. Here and subsequently, the repeated indices $i, j, \dots = 1, 2, 3$ (or x, y, z) imply summation over these indices and ϵ_{ijk} is the antisymmetric Levi-Civita symbol.

The value of $\deg f_2$ for any type of singularity is an integer number, corresponding to the signed number of times the image of coordinate manifold sphere S^2 is wrapped around the vector space sphere S^2 . Hence it is the topological characteristic of the singular point that does not depend on the choice of the wrapping surface. The important result of differential topology, established by Poincaré in 1885 [90] and quantified by Hopf in 1931 [91] using relations (3) and (4) is that the topological charges of singular points, represented by their mapping degrees, are equal to the indices of their singularities (2); specifically, $\deg f_\nu = \text{Ind}_{\nu+1}$ with $\nu = 1, 2$. This fundamental result not only reveals the deep connection between the topological properties of singular points and the differential characteristics of the surrounding vector field but also enables the global topological exploring of the vector field over the entire coordinate manifold, which will be considered in the next Section.

2.2.4. Poincaré–Hopf theorem

The Poincaré–Hopf theorem is a fundamental theorem in differential topology that connects the intrinsic topology of a manifold to the properties of vector fields defined on it. Specifically, it provides a profound relationship between the number and nature of the singularities of a vector field and the manifold’s topology. This foundational theorem is typically formulated for *closed manifolds* – i.e., manifolds without boundary, see Section 2.1.2. It asserts that for a smooth closed manifold \mathcal{M} of dimension ν and a smooth vector field \mathbf{V} on \mathcal{M} , with a finite number of isolated singular points $\mathbb{V}_i \in \mathcal{M}$, the sum of the indices of these singular points is equal to the Euler characteristic of the manifold,

$$\sum_i \text{Ind}_\nu(\mathbb{V}_i) = \chi_E(\mathcal{M}). \quad (6)$$

The closeness of the manifold is a necessary condition, limiting the theorem’s direct application to singularities inside the bounded volume. However, the theorem remains valuable for the surfaces enveloping these structures, serving as a useful tool for characterizing 2D surface singularities through microscopy techniques such as PFM, AFM, and SEM.

As an example, we apply the Poincaré–Hopf theorem to the sphere S^2 , which bounds the ball D^3 with $S^2 = \partial D^3$, as illustrated in Fig. 1(d,e). As we already mentioned, we restrict ourselves to the case, relevant to ferroelectrics, when the vector field \mathbf{V} is tangential to the boundary $\partial \mathcal{M}$. According to Table 1, the sphere has an Euler characteristic of $\chi_E(S^2) = 2$. From the Poincaré–Hopf theorem, it follows that any vector field tangential to the surface of the sphere must exhibit singularities whose total index sums to 2. For instance, in the meridian vector field distribution shown in Fig. 1(d), two singular points emerge: a stable node at the south pole N_{in} , and an unstable node at the north pole N_{out} , both with an index of $+1$, see Table 2. Together, their indices sum to $+2$, which matches the Euler characteristic of S^2 . This example demonstrates the well-known *Hairy Ball Theorem*, which asserts that no non-vanishing continuous tangential vector field can exist on a sphere. In other words, it is impossible to ‘comb’ a hairy ball without creating cowlicks, representing the singular points in the vector field.

As another example, we consider a 2D torus T^2 , Fig. 1(f), which has a zero Euler characteristic, $\chi_E(T^2) = 0$, see Table 1. This implies that the total sum of the vector field indices must also be zero, allowing for the construction of a smooth, continuous vector field on the torus with no singularities – meaning it is possible to “comb” the vector field on a torus without creating any discontinuities. An exemplary vector field, circulating smoothly around the toroidal surface without singular points, is shown in Fig. 1(f). Alternatively, it is possible to create a vector field on the torus that includes several singular points with a total zero index. For instance, one could have a stable focus, F_{in} with index $+1$ and a saddle point S with index -1 , see Table 2, maintaining the required balance. The possibility of the absence of singularities in the vector field on the surface of a torus plays a crucial role in understanding the overall structure of the polarization field in confined ferroelectrics, as described by Arnold theorem, which we will discuss in Section 4.3.3.

To explore singularities in the whole 3D structures with boundary, an extension of the Poincaré–Hopf theorem to the manifold \mathcal{M} with boundary $\partial \mathcal{M}$ is required, which accounts for both volume singular points, \mathbb{V}_i , and surface singular points, \mathbb{V}_{sj} , simultaneously. For this purpose, we introduce a duplicate manifold \mathcal{M}' , aligned with \mathcal{M} along their common boundary $\partial \mathcal{M} = \partial \mathcal{M}'$. This creates a unified, boundary-free closed manifold $\mathcal{M}_U = \mathcal{M} \cup \mathcal{M}'$. To endow the whole manifold with a vector field structure we extend the vector field \mathbf{V} symmetrically to a field \mathbf{V}' in \mathcal{M}' . Then the singular points $\mathbb{V}_i \in \mathcal{M}$ will double onto $\mathbb{V}'_i \in \mathcal{M}'$, while singular points \mathbb{V}_{sj} on the boundary will become defined in whole neighborhoods in \mathcal{M}_U , not in half-neighborhoods as before in \mathcal{M} . Note that the field $\mathbf{V}_U = \mathbf{V} + \mathbf{V}'$ is continuous within \mathcal{M}_U , but it may not be smooth across the boundary $\partial \mathcal{M}$. However, assuming a natural non-degeneracy, it can be smoothed, as outlined in [92].

Since the manifold \mathcal{M}_U , containing the singular points \mathbb{V}_i , \mathbb{V}'_i , and \mathbb{V}_{si} , is now closed, the Poincaré–Hopf theorem can be applied. Given that $\text{Ind}_3(\mathbb{V}_i) = \text{Ind}_3(\mathbb{V}'_i)$, we extend the Poincaré–Hopf theorem as follows:

$$2 \sum_i \text{Ind}_3(\mathbb{V}_i) + \sum_j \text{Ind}_3(\mathbb{V}_{sj}) = \chi_E(\mathcal{M}_U). \quad (7)$$

$$\chi_E(\mathcal{M}_U) = 2\chi_E(\mathcal{M}) - \chi_E(\partial\mathcal{M}).$$

This relation links the indices of internal singular points and surface singular points at the boundary of the manifold to the Euler characteristic of the unified manifold. The value of the Euler characteristic is derived using the inclusion–exclusion principle [93]: $\chi_E(\mathcal{M} \cup \mathcal{M}') = \chi_E(\mathcal{M}) + \chi_E(\mathcal{M}') - \chi_E(\mathcal{M} \cap \mathcal{M}')$, with $\chi_E(\mathcal{M}) = \chi_E(\mathcal{M}')$, and $\mathcal{M} \cap \mathcal{M}' = \partial\mathcal{M}$.

We now apply the steps described above to a simply connected particle, which is topologically equivalent to a 3-dimensional ball, D^3 , with its boundary $\partial D^3 = S^2$. By doubling the D^3 manifold, we obtain a 3D sphere, S^3 , which is a closed manifold with no boundary. The Euler characteristic of this manifold is $\chi_E(S^3) = 2\chi_E(D^3) - \chi_E(S^2) = 2 \cdot 1 - 2 = 0$, as shown in Table 1. Consequently, the sum of the 3D indices of all singular points, both on the surface, counted with coefficient 1 according to the formula (7), and within the bulk, with coefficient 2, must be zero. As discussed earlier, the surface of a ball contains singular points with a total 2D index of 2, ensuring the presence of surface singularities. However, this constraint provides no further insight into the nature or behavior of singularities beneath the surface unless the 3D indices of surface singularities, \mathbb{V}_{si} , are known. These 3D indices are not directly related to their 2D counterparts and depend on how the vector field emerging from the interior of \mathcal{M} terminates at these points. Consider, for instance, the previously discussed meridian vector field distribution at the surface of the ball, with two singular points, N_{in} , and N_{out} located at the south and north poles of the spherical surface respectively, see Fig. 1(d). Suppose that the internal vector field \mathbf{V} enters at the north pole into N_{out} , and exits at the south pole from N_{in} , as shown in Fig. 1(e). In the unified manifold \mathcal{M}_U , the singular point N_{out} corresponds to a saddle 3D singularity S_- at the north pole with an index of -1 , while N_{in} corresponds to a saddle 3D singularity S_+ at the south pole with an index of $+1$, see Table 3 and Fig. 1(p,q). The calculation shows that, according to the relation (7), the sum of the 3D indices of singular points inside the ball must also equal zero. Thus, the ball may either not contain any internal singular points at all, or their indices must compensate for each other. For example, this could be a pair of saddle points like S_- and S_+ , located in the bulk of the ball, with indices $\text{Ind}_3(S_-) = -1$ and $\text{Ind}_3(S_+) = +1$, as shown in Fig. 1(e). Another interesting example occurs in confined 2D circular geometry when boundary center-type half-vortex singularities annihilate with the bulk center-type vortex singularity, as considered in magnetic systems in [94].

The application of the Poincaré–Hopf theorem to ferroelectrics presents distinct restrictive characteristics. First, as it will be discussed in Section 3.2, the polarization vector field, $\mathbf{P}(\mathbf{r})$, in ferroelectrics tends to be divergence-free. This introduces additional constraints on the admissible configurations of singular points, which will be explored in detail in Section 4.2.1. Notably, divergence-free saddle-type singular points are stable, whereas repelling and attracting singular points, which generate dipolar bound charges, are energetically unfavorable, unless localized compensating charges – induced by imperfections – are introduced. This aspect is addressed in Section 5.3.1. Another key constraint in confined ferroelectrics is the tangential orientation of the polarization vector field at the surface. However, external charges and electrodes can lead to situations where in certain regions $\mathbf{P}(\mathbf{r})$ deviates from this assumed tangential orientation, adopting either an outward or inward direction. The Poincaré–Hopf theorem permits further generalization in such cases, as discussed in [95,96]. A similar situation involving a general orientation of the field at the surface was examined in [84] for droplets of nematic liquid crystals, where a formalism based on relative homotopy groups [97,98] was applied. Furthermore, the specific symmetry conditions may constrain multiple typical singular points, as described in Section 2.2.2, to coalesce into composite degenerate singular points. Such situation for manifolds with boundaries was explored in [99].

2.3. Unit vector fields

2.3.1. Order parameter space

Here, we consider a specific class of vector fields where the vector magnitude is fixed at one. Such descriptions are common in magnetic systems, where the magnitude of the order parameter is constrained by quantization, carrying magnetic spin, and in liquid crystals, where the fixed length of the director is provided by the size of the molecules. In ferroelectrics, the constant polarization assumption is less justified, although it remains useful and widely employed, for qualitative description of topological states. We discuss another topological constraint in ferroelectrics, based on the almost divergence-free nature of polarization fields in Section 4.

Fig. 2 presents examples of applying topological considerations to systems with unit vector order parameters. We refer here to magnetic systems [100], which have traditionally been used as a reference for the topological description of ferroelectrics [49]. Magnetic ordering is usually characterized by the unit length magnetization vector $\mathbf{m}(\mathbf{r})$, $|\mathbf{m}(\mathbf{r})| = 1$, that can assume an arbitrary spacial direction in case of weakly anisotropic magnetism. Accordingly, the end of the vector \mathbf{m} sweeps the unit sphere surface, S^2 , that constitutes the order parameter space D . Two other configurations for the order parameter space are possible in the case of strong uniaxial anisotropy. In the case where vector \mathbf{m} is oriented perpendicularly to the anisotropy axis (i.e., lies in an easy-plane, transversal to the anisotropy direction), the

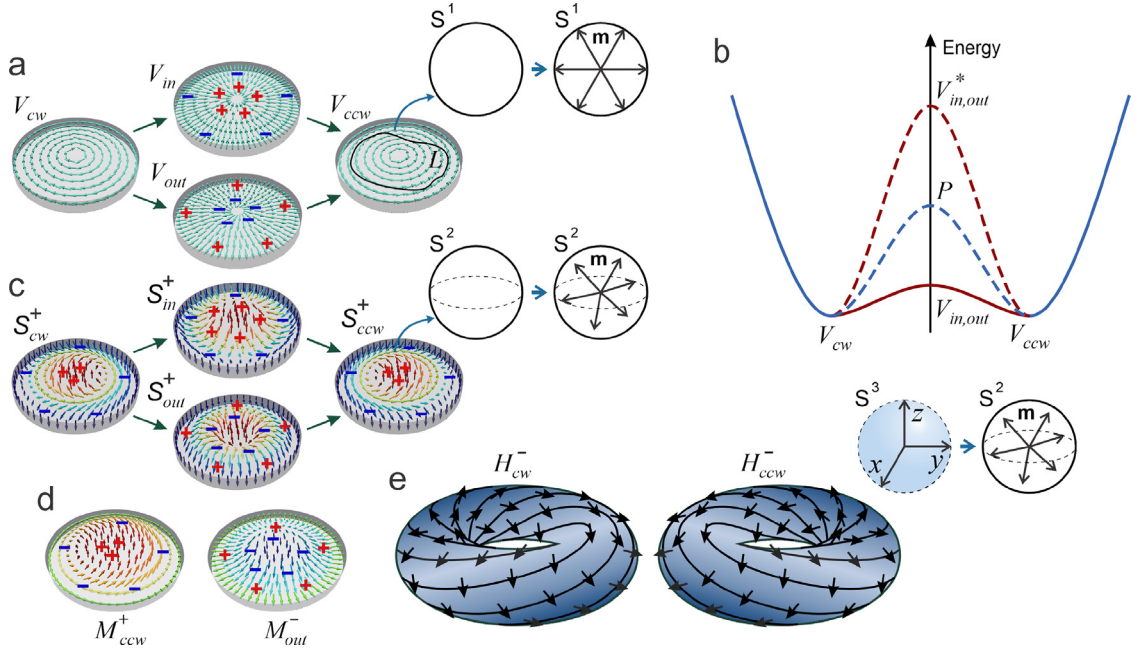


Fig. 2. Unit vector field topological states and homotopy groups. (a) Different types of vortices with the clockwise, V_{cw} , counterclockwise, V_{ccw} , incoming, V_{in} , and outgoing, V_{out} , distribution of vector order parameter, belonging in the same topological class of vortex states, emerging in 2D films with vector \mathbf{m} lying in the film plane. The arrows demonstrate the pathway of continuous transition from V_{cw} to V_{ccw} through the intermediate states V_{in} or V_{out} by the continuous rotation of unit vectors \mathbf{m} . Plus and minus symbols stand for bound electric charges that would have emerged had we considered ferroelectric order parameter. The scheme in the upper-right corner demonstrates the action of the homotopy group. The unit circle of the coordinate space, S^1 , which is equivalent to the closed contour L embracing the vortex center, maps onto the order parameter space S^1 of the unit vector \mathbf{m} , lying in the film plane due to the easy-plane anisotropy. (b) The energy profile, explaining that the switching from the V_{cw} to the V_{ccw} vortex occurs more advantageously when staying in the same topological class of vortices and realizes through the intermediate vortex configurations V_{in} or V_{out} (solid red energy line), rather than by passing through the high-symmetry paramagnetic state, P , in case of magnetism (dashed blue energy line). At the same time, in the ferroelectric system, switching through the paraelectric state is more advantageous than switching by passing across the charged vortex states V_{in}^* or V_{out}^* because of the huge electrostatic energy barrier formed by emerging bound charges (dashed red energy line). (c) Different types of skyrmions, either of Bloch type – with the clockwise, S_{cw}^+ , and counterclockwise, S_{ccw}^+ , swirling – or of Néel type, with incoming, S_{in}^+ , and outgoing, S_{out}^+ , distribution of the vector order parameter, belonging in the same topological class of skyrmion states, emerging in 2D isotropic films. The arrows demonstrate the pathway of the continuous transition from S_{cw}^+ to S_{ccw}^+ through the intermediate states S_{in}^+ or S_{out}^+ by the continuous rotation of the unit vectors \mathbf{m} . Plus and minus symbols stand for bound electric charges that would have emerged had we considered ferroelectrics instead of magnets. The scheme in the upper-right corner demonstrates the action of the homotopy group. The unit sphere of the coordinate space, S^2 , equivalent to the whole space of the film with a fixed direction of the vector field at infinity, maps onto the order parameter space S^2 of the unit vector \mathbf{m} , taking an arbitrary direction. (d) Exemplary illustration of the Bloch meron M_{ccw}^+ , and Néel meron M_{out}^- . (e) The topological Hopfions H_{cw}^- and H_{ccw}^- , emerging in the isotropic bulk systems with vector order parameter. They are described by the $S^3 \rightarrow S^2$ homotopy group, as shown in the scheme in the upper-right corner. Each point in the order parameter space S^2 presenting a particular direction of \mathbf{m} , has a preimage in the form of the whole line in the real space with an equivalent direction of \mathbf{m} at infinity. These lines are wound in the system of concentric tori.

order parameter space is reduced to the circle of the unit radius, S^1 . Otherwise, when the anisotropy orients \mathbf{m} in the easy-axis direction, parallel to the anisotropy axis, the order parameter space, denoted as \mathbb{Z}_2 , is reduced to the two points, corresponding to the “up” and “down” directions of \mathbf{m} .

To employ the coordinate space of the system, \mathcal{M} , we note that conventionally bulk samples are characterized by the 3D Euclidean space, \mathbb{R}^3 , whereas thin films and nanowires are described in terms of the 2D and 1D Euclidean spaces \mathbb{R}^2 and \mathbb{R}^1 , respectively. However, in many cases, one assumes that topological excitations are localized within a certain region of space and that the behavior of the order parameter at infinity is uniform. Within the topological approach, such a condition is naturally accounted for by an assumption that the infinite points of the corresponding \mathbb{R}^n space are adjusted together, forming the n -dimensional sphere S^n . Then, depending on the considered problem, the coordinate space \mathcal{M} either coincides with \mathbb{R}^n or with S^n spaces of the whole system or forms their subspace.

2.3.2. Vortices

Let us consider, as an example, the formation of vortices [7] in a 2D space of a thin film, \mathbb{R}^2 , in the case where the vector \mathbf{m} is restricted to the film plane by the easy-plane anisotropy. The corresponding order parameter space is $D = S^1$. Fig. 2(a) shows several types of vortices. Together with vortices V_{cw} with the clockwise (CW) vector order parameter winding around the vortex center and vortices V_{ccw} with the counterclockwise (CCW) vector order parameter winding

around the vortex center, the star-like vortex states V_{in} with the incoming into the vortex center vector field, and V_{out} with the outcoming from the vortex center vector field, also belong in the same class of vortex topological states.

To demonstrate that, we employ the homotopy group topological approach. We encircle the core of the vortex by the closed contour $L \subset \mathbb{R}^2$ (exemplified in Fig. 2(a) for the vortex V_{ccw}). Next, we travel around the selected loop performing an operation that is topologically equivalent to a complete turn along the unit circle which we consider as a coordinate space $\mathcal{M} = S^1$, shown in the upper-right corner of Fig. 2(a). We observe that the order parameter, \mathbf{m} , also performs one complete turn in the order parameter space $D = S^1$, shown as the second circle in the upper-right corner of Fig. 2(a). Therefore, one assigns the winding number $N_1 = 1$ to the vortex V_{ccw} . In general, the winding number N_1 is determined by the Poincaré–Hopf degree of the mapping $S^1 \xrightarrow{f_1} S^1$ as $N_1 = \deg f_1$, using Eq. (3) with $\mathbf{m} = \mathbf{n}$.

This winding number expressing the topological charge of the vortex remains the same for any of the vortices presented in Fig. 2(a) and for any bending of the contour L , encompassing the vortex core. Such a procedure allows assigning these vortices to the topological class with $N_1 = 1$. One can also imagine other stable topological states defined by the mapping $S^1 \xrightarrow{f_1} S^1$ as $N_1 = \deg f_1$. Those are, for instance, a double-winding vortex with $N_1 = 2$, for which the order parameter performs two complete turns in the order parameter space S^1 , anti-vortex with $N_1 = -1$ for which the turning occurs in the opposite direction, or simply almost-uniform state for which $N_1 = 0$.

Importantly, the transformation between the different states of the same topological class can occur via the continuous deformation of the vector field, conserving the winding number N_1 . For instance, the transformation from V_{cw} to V_{ccw} can be realized through the continuous in-plane rotations of the order parameter vectors by passing through the intermediate states V_{in} or V_{out} , see Fig. 2(a). In energy terms, this implies that the transformation between the different states of the same topology class does not require large energy costs, as illustrated in Fig. 2(b). Thus, the transformation from V_{cw} to V_{ccw} may occur going over a small energy barrier stemming from the difference between the gradient energy of the states V_{cw} , V_{ccw} and V_{in} , V_{out} (the red solid line) rather than over the barrier (shown by the blue dashed line) arising due to the formation of a high-symmetry para-phase, P . This ensures the topologically protected stability of the vortex state with $N_1 = 1$ since its transformation to the states belonging to another class demands large energy. For example, transformation into the uniform state with $N_1 = 0$ would require vortex destruction via the partial or complete melting of a vortex state into para-state spending the energy necessary to overcome a huge barrier corresponding to condensation energy of the ordered state.

2.3.3. Skyrmions

Taking another example, skyrmions [101–108], we consider topological states in thin films, now the case of vanishingly small anisotropy, where the order parameter space is a 2D sphere, S^2 . As a coordinate space, we select the entire film with the adjusted together infinity points, hence $\mathcal{M} = S^2$, assuming that the vector field of the order parameter is uniform at infinity and has, for instance, the down-directed orientation. The corresponding mapping $S^2 \rightarrow S^2$, classifying the topological states, skyrmions, indicates how many times, N_2 , a 2D sphere of the order parameter space is wrapped around a 2D sphere presenting the coordinate space. The topological charge of a skyrmion, referred to as the Pontryagin index in magnetic and ferroelectric literature [49,100], represents the Poincaré–Hopf degree of the mapping $S^2 \xrightarrow{f_2} S^2$. It is calculated using Eq. (4) as $N_2 = \deg f_2$, with $\mathbf{m} = \mathbf{n}$.

For the topological state carrying the topological charge $N_2 = 1$, the orientation of the unit vector \mathbf{m} assumes – one time each – all possible directions when passing the entire plane of the film, providing the one-quanta skyrmion texture. Typical representatives of the $N_2 = 1$ skyrmions, like Bloch skyrmions with screwed order parameter, S_{cw}^+ and S_{ccw}^+ (cw and ccw denote the clockwise and counterclockwise swirling of the texture, and the sign, “+” or “–” shows the polarity of the core), and Néel skyrmions, S_{in}^+ and S_{out}^+ , having the fountain-like overturning order parameter with the in- and out-of-the-center directed vector field flux, respectively, are shown in Fig. 2(c). Note that the in-plane winding of skyrmions is uniquely defined by their swirling and polarity. Similar to vortices, the skyrmions belonging to the same topological class can transform one into another via the continuous deformation of the order parameter requiring low gradient energy costs. In particular, for the skyrmions with $N_2 = 1$, the pathway of the continuous switching between Bloch skyrmions of different winding occurs through the intermediate Néel skyrmions S_{in}^\pm and S_{out}^\pm . The skyrmion states with given N_2 are topologically protected because they are separated by essential energy barriers (of the order of the ordered state condensation energy) from the states with other topological charges, particularly from the uniform state with $N_2 = 0$.

2.3.4. Merons

The merons represent another topological state dwelling in 2D systems and having a structure analogous to that of skyrmions [107,109–113]. Similarly, they can be of the Bloch type, M_{cw}^\pm and M_{ccw}^\pm , possessing clockwise or counterclockwise swirling, or of the Néel type, M_{in}^\pm and M_{out}^\pm . Fig. 2(d) shows the typical representatives, merons M_{cw}^+ and M_{out}^- . The distinction from skyrmions is that the order parameter vector field in skyrmions at infinity is supposed to be either up or down-directed with respect to the film, whereas in merons it remains confined within the plane of the film. Accordingly, the topological structure of merons presents a “partial-skyrmion”, specifically “half-skyrmion” structure. It means that meron’s vector field texture results from the cutting of the inner region of the skyrmion in which the vector sweeps only the upper half of the S^2 sphere in the order parameter space. At its periphery, the vector order parameter lies in the film plane and makes a full 360° turn when going around the meron center. Therefore, merons can also be globally viewed as vortices in which the order parameter vector escapes from the film plane at the core, avoiding hence the singularity.

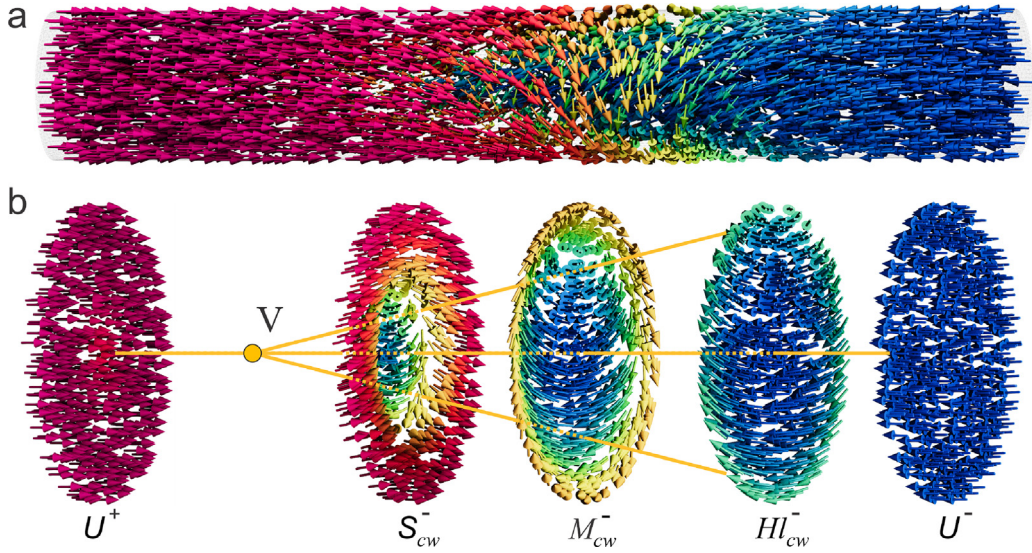


Fig. 3. Polarity switching via continuous transformation of topological states in a vortex tube along the nanorod (a). (b) A skyrmion S_{cw}^- nucleates from the uniformly polarized state U^+ , forming a singular point V . The system transitions through a meron M_{cw}^- and a helical state Hl_{cw}^- , ultimately reaching the oppositely polarized uniform state U^- .

2.3.5. Vector field tubes

The topological states of the unit vector field, as described thus far, were confined to a 2D coordinate manifold, specifically within a disk or an infinite plane. These textures can also extend into the third dimension, propagating through the thickness of the host material. Structures of this type, hosted skyrmion strings were discovered in magnetic materials [67,114–118]. Notably, this extension of 2D topological states into 3D alters their homotopy group classification, and these states may lose their topological protection. For instance, a singular vortex in 3D geometry can be continuously transformed into a nonsingular field configuration [57,98]. Non-topological factors, such as uniaxial anisotropy resulting from the easy-plane crystal anisotropy, specific boundary conditions, or external fields inducing anisotropy in the system, can still stabilize these vortex-like structures. The vector field tubes reviewed in this article typically manifest along the axes of nanorods and nanowires, or as cylindrical stripe domains within heterostructures. These configurations are discussed in detail in Sections 7.3 and 7.4, respectively.

The topological states, such as vortices, skyrmions, and merons form structural units propagating along the tube, as shown in Fig. 3(a). Notably, the specific topological state within the tube is predominantly stabilized by energetic factors, although these states are topologically transformable into one another. Fig. 3(b) illustrates various topological states that continuously emerge within an exemplary vortex tube hosted by nanorod. We analyze the evolution of these states along the nanorod, progressing from left to right. Initially, the skyrmion states, denoted as S_{cw}^- , nucleate in the center of the uniform state U^+ , emerging from the singular point V , see Section 2.2. In the center of the skyrmion, the direction of the vector field is opposite to that in the surrounding uniform state. As the skyrmion expands further off-center, it twists the vector field at the nanorod surface, leading to the formation of a meron configuration, M_{cw}^- . Subsequently, the surface fields reverse direction, transitioning the system into the uniform state U^- , which is opposite to the initial state U^+ . This transition occurs through an intermediate helical state, Hl_{cw}^- .

2.3.6. Real space Hopfions

Finally, we discuss topological states, Hopfions, that can emerge in the 3D space of the bulk of an isotropic or weakly anisotropic material with unit vector order parameter, specifically in magnetic systems [107,119–129]. The exemplary textures of H_{cw}^- and H_{ccw}^- Hopfions are shown in Fig. 2(e). They are classified via the mapping of the real-space manifold of the entire material volume S^3 (we assume the fixed direction of \mathbf{m} at the infinity) on the order parameter space of the unit vector \mathbf{m} , S^2 . The mathematical study of the topological classes corresponding to the mapping $S^3 \rightarrow S^2$, first undertaken in 1931 by Heinz Hopf [91], again gives the classification according to the topological charges. The realization of topological states in the considered case is described in terms of the tracelines of vector \mathbf{m} which are traces of vector \mathbf{m} having the same direction. Each point in the order parameter space S^2 , presenting a particular direction of \mathbf{m} , has a preimage in the form of the whole traceline in the real space S^3 . The tracelines densely fill the coordinate space and constitute the so-called Hopf fibrations or simply Hopfions. The integer topological charge of Hopfions is given by the relation [130,131]

$$N_3 = -\frac{1}{(8\pi)^2} \int_{S^3} \mathbf{F} \cdot \mathbf{A} dV, \quad (8)$$

where the vector field \mathbf{F} is defined by Eq. (5) with $\mathbf{m} = \mathbf{n}$, and \mathbf{A} is the vector potential of \mathbf{F} , $\mathbf{F} = \nabla \times \mathbf{A}$. The integration in Eq. (8) is carried out over the whole volume of the system.

In summary, the considered in this Section mappings of the unit vector field are formally described by homotopy groups of n -dimensional spheres with $n = 1, 2, 3$, $S^1 \rightarrow S^1$, $S^2 \rightarrow S^2$, and $S^3 \rightarrow S^2$, also denoted as $\pi_1(S^1)$, $\pi_2(S^2)$, and $\pi_3(S^2)$. These groups are all isomorphic to the group \mathbb{Z} of integers under addition; the integers correspond to the topological charges N_1 , N_2 and N_3 of the described topological states [59]. Other types of sphere mapping in 1D, 2D, and 3D spaces in the case of the vector order parameter give the trivial homotopy groups, isomorphic to zero. Therefore, the considered representative cases cover the most typical topological states of the vector field with fixed vector magnitude.

3. Ferroelectrics. Essential concepts

3.1. Ginzburg–Landau–Devonshire approach

In ferroelectrics, the polarization order parameter is the polarization vector $\mathbf{P} = (P_1, P_2, P_3)$, describing how charges within the material are displaced relative to their equilibrium positions and align in a specific direction. The polarization vector \mathbf{P} represents the electric dipole moment per unit volume. Formally, it can be expressed as: $\mathbf{P} = V^{-1} \sum \mathbf{p}_i$, where \mathbf{p}_i is the dipole moment of an individual ionic charge, and V is the volume over which the dipoles are considered. The direction of the vector shows where the dipoles are pointing, and the magnitude indicates the degree of dipole alignment. In the paraelectric high-temperature phase, the order parameter is zero which reflects the absence of electric ordering. In the ferroelectric phase, which emerges spontaneously below the critical temperature T_c , the order parameter $\mathbf{P} \neq 0$ indicates the onset of spontaneous dipole alignment.

Importantly, even though dipoles are discrete, polarization can be regarded as a continuous vector field. When we describe polarization in this way, we imply averaging over small volumes of material [132,133]. While larger than individual atoms or molecules, these volumes are still on the scale of several nanometers. This size corresponds to the coherence length of the ferroelectric material, ξ_0 , which is the distance over which dipoles within the material remain interconnected and their orientations are correlated. At this length scale, microscopic fluctuations are averaged out, and the material can be described in terms of macroscopic vector fields. In ferroelectrics well below T_c , the coherence length $\xi_0 \simeq 1\text{--}2$ nm and increases when approaching T_c . It approximately corresponds to the half-width of the domain wall between oppositely oriented polarization domains.

The Ginzburg–Landau–Devonshire (GLD) theory of phase transitions is the core approach in ferroelectrics, based on minimizing the GLD energy in terms of the polarization order parameter \mathbf{P} [132–134],

$$\mathcal{F}_f = \mathcal{F}_p + \mathcal{F}_{grad} = \int (F_p + F_{grad}) dV. \quad (9)$$

This energy includes the energy density of the uniform ferroelectric state, F_p , and the gradient energy F_{grad} ,

$$F_p = a_i(T)P_i^2 + a_{ij}P_i^2P_j^2 + a_{ijk}P_i^2P_j^2P_k^2, \quad F_{grad} = \frac{1}{2}G_{ijkl}(\partial_i P_j)(\partial_k P_l). \quad (10)$$

The uniform energy, F_p , is typically expanded up to the 4th or 6th order in \mathbf{P} , where one or several second-order coefficients $a_i(T)$ become negative below T_c , providing the instability of the system towards the transition to the ferroelectric state. This state is stabilized by the fourth- and sixth-order coefficients a_{ij} and a_{ijk} . The gradient energy, F_{grad} , accounts for the energy cost of spatial variations of polarization, related, in particular, to domain formation. This contribution is expanded to the second order in polarization gradients.

An important aspect that governs the behavior of ferroelectrics is the coupling of the polarization with physical fields, electric field \mathbf{E} and elastic field presented by the Cauchy stress tensor, σ_{ij} . These couplings, described by the terms

$$\mathcal{F}_{PE} = \int F_{PE} dV, \quad F_{PE} = -P_i E_i, \quad (11)$$

$$\mathcal{F}_{P\sigma} = \int F_{P\sigma} dV, \quad F_{P\sigma} = -Q_{ijkl}P_i P_j \sigma_{kl}, \quad (12)$$

where Q_{ijkl} are electrostrictive constants, should be added to the ferroelectric contribution (9) to minimize the energy $\mathcal{F}_f + \mathcal{F}_{PE} + \mathcal{F}_{P\sigma}$ and describe the polarization state.

The variational minimization of the system's energy is performed under the additional constraints of the mechanical and electrostatic constitutive equations. The mechanical stability condition, which equilibrates the elastic forces and the forces produced by stress-polarization coupling (12), is an elasticity equation,

$$\partial_i (\sigma_{ij} + q_{ijmn} P_m P_n) = 0, \quad (13)$$

where $q_{ijmn} = C_{ijkl} Q_{klmn}$ is the product of the elastic stiffness tensor, C_{ijkl} , and electrostrictive constant tensor, Q_{klmn} . We do not consider the flexoelectric contribution [135,136] to the elastic energy density, given by $F_{flexo} = f_{ijkl}^{(\sigma)} P_i \partial_j \sigma_{kl}$, where $f_{ijkl}^{(\sigma)}$ is the flexoelectric tensor defined in terms of stress variables. The topological consequences of this higher-order stress effect can be analyzed later as a perturbation to the main energy functional, as described in Section 5.1.

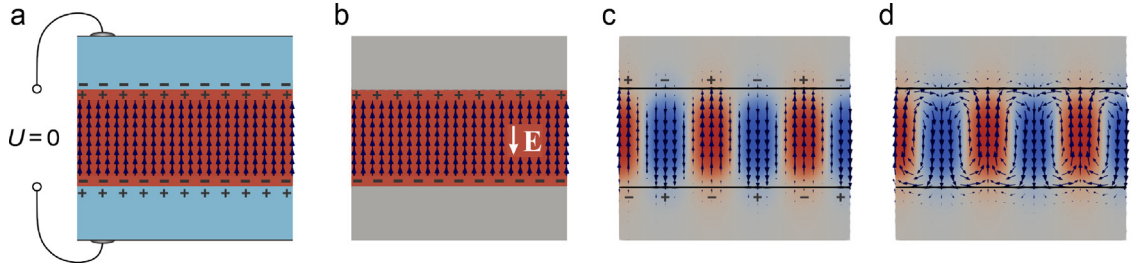


Fig. 4. Screening of bound charges in a ferroelectric slab. (a) The bound charges are screened by electrodes. (b) In the absence of the electrodes the strong depolarization charges emerge at the slab surface. They create the depolarization field \mathbf{E} , which destroys the ferroelectric state. (c) Splitting the sample into alternatively directed soft polarization domains reduces the depolarization energy. The depolarization field, produced by the alternative bound charges, is localized near the sample surface. (d) Further screening of the depolarization field is ensured by the transverse polarization component, which provides the soft polarization domains with a vortex structure. A minor part of the polarization flux emerges from the ferroelectric and is confined near the surface.

The electrostatic Maxwell equations,

$$\text{div}(\varepsilon_0 \varepsilon_b \mathbf{E}) = \rho_b + \rho_q + \rho_e, \quad \nabla \times \mathbf{E} = 0, \quad (14)$$

where $\varepsilon_0 = 8.85 \times 10^{-12} \text{ CV}^{-1}\text{m}^{-1}$ is the vacuum permittivity and ε_b is the background dielectric constant of the non-polar ions [137]. This equation relates the electric field, \mathbf{E} , to the bound charge density produced by the non-uniform distribution of polarization dipoles, $\rho_b = -\text{div} \mathbf{P}$, localized charges, ρ_q , and free conductive charges, ρ_e . It is convenient to express the electric field via the electrostatic potential, $\mathbf{E} = -\nabla \varphi$, and present the electrostatic equations (14) in the form of a screened Poisson equation,

$$\varepsilon_0(\varepsilon_b \nabla^2 \varphi - \delta^{-2} \varphi) = \partial_i P_i - \rho_b, \quad (15)$$

where we represent the screening effect of free charges in a linearized Debye–Huckel–Thomas–Fermi form, $\rho_e = -\varepsilon_0 \delta^{-2} \varphi$, with δ being the screening length. Note that the particular symmetrical structure of the tensors coefficients a_i , a_{ij} , a_{ijk} , G_{ijkl} , Q_{ijkl} , and C_{ijkl} depend on the symmetry of materials, while their specific values can be found in standard textbooks, see, e.g. [134].

3.2. Electrostatics of ferroelectrics

A key aspect in forming non-uniform topological states in ferroelectrics is the counterbalance between the system's tendency to form a coherent ferroelectric state and the depolarization electrostatic forces destabilizing this state. To put this competition on a quantitative basis, we compare two contributions to the energy of the ferroelectric state, the ferroelectric contribution and the depolarization contributions. The first, the favorable ferroelectric energy, F_p , represents the energy gain of the ferroelectric state relative to the paraelectric state. This is the energy of the ferroelectric sample in which the depolarization field is screened by external short circuited electrodes with potential $U = 0$, see Fig. 4(a). The uniform energy of the ferroelectric state, F_p , calculated per unit volume, is given by Eq. (10). It is estimated as the value opposite to the work done by an external electric field, produced by the electrode voltage U , and applied against the polarization to restore the paraelectric state: $F_p \approx -\int_{P=P_0}^{P=0} P(E) dE \approx -(T_c/\varepsilon_0 C) P_0^2$. Here, $P(E) = P_0 - \varepsilon_0 \chi E$ is the constitutive relation for a ferroelectric (with \mathbf{E} opposite to \mathbf{P}), P_0 is the spontaneous polarization in the ferroelectric state, and $\chi = C/(T_c - T)$ is the Curie–Weiss susceptibility of the uniform ferroelectric with Curie constant C [133]. Well below the critical temperature T_c , $\chi \approx C/2T_c$.

The second, depolarization energy contribution, F_{dep} , represents the energy that destabilizes the ferroelectric state due to the emergence of the depolarization field E_{dep} , which appears in a ferroelectric with a free surface, Fig. 4(b). The termination of polarization at the surface of the sample results in the emergence of the surface bound charge $\sigma_0 = P_0$ which, in turn, produces the depolarization electric field, oriented oppositely to polarization, $E_{dep} = -\sigma_0/\varepsilon_0 \varepsilon_b = -P_0/\varepsilon_0 \varepsilon_b$. The associated with E_{dep} depolarization energy,

$$\mathcal{F}_{dep} = \int F_{dep} dV, \quad F_{dep} = \frac{1}{2} \varepsilon_0 \varepsilon_b E_{dep}^2 = \frac{P_0^2}{2\varepsilon_0 \varepsilon_b}, \quad (16)$$

is positive. Here, ε_b represents the background dielectric constant associated with the non-polar ions, typically located at the A-site of the perovskite lattice in pseudo-cubic oxide ferroelectrics. This constant accounts for the non-polar ions' contribution to the overall polarizability of the system. Its value should be on the order of the permittivity of the non-polar oxide perovskite and usually is considered to be around $\varepsilon_b \simeq 10$ [137].

The depolarization energy density, F_{dep} , is by the factor $\kappa = 2C/\varepsilon_b T_c$ larger than the absolute value of F_f . In the most functional oxide ferroelectrics that are displacive ferroelectrics, this factor is especially large [133], for example, $\kappa \simeq 10^2$ for PbTiO_3 , and 0.5×10^2 for BaTiO_3 [138]. It is the substantial predominance of the positive depolarization energy over

the negative GLD energy that significantly destabilizes the uniform ferroelectric state and finally results in the strongly non-uniform state, in which the emerging bound charges and produced by them depolarization fields are reduced due to the non-uniform polarization field configuration.

The best known example of the formation of the non-uniform state reducing the depolarization energy is the emergence of the alternatively polarized Landau–Kittel domains in ferroelectric slabs [5,8,139]. Dividing the system into domains results in the formation of stripe-like surface depolarization charges with alternating signs. Consequently, the depolarization field is confined to the near-surface layer, significantly reducing the associated depolarization energy. It was shown [9,140] that in thin ferroelectric films, the electrostatic energy of the Landau–Kittel domains is minimized even more, if the surface bound charges draw back into the domain volume at points of domain termination. This results in the gradual profile of the spontaneous out-of-plane polarization inside domains from almost zero at points of domain termination to almost equilibrium value P_0 in the bulk of the domain, see Fig. 4(c). Such polarization profile is referred to as “soft polarization domains” [140,141], to highlight its distinction from the Landau–Kittel domains with flat magnetization profile in ferromagnets. This distribution is complemented by the field-induced in-plane polarization component near the film surface, resulting in the overall polarization texture, looking like the periodic structure of alternatively rotating vortices, shown in Fig. 4(d) [142].

Though stemming from the same electrostatic principles, the emergence of more intricate topological states necessitates an advanced mathematical treatment. The hydrodynamic topological approach developed in this Review offers a natural framework for considering topological states in ferroelectrics, fundamentally rooted in their electrostatic origin.

3.3. Ferroelectricity versus magnetism

Since ferroelectrics appeared as an electrical duality to ferromagnets, the topological description of their properties was constructed as a direct extension of the described above methods of the real-space homotopy groups for vector fields [49]. There are, however, essential differences between magnetic and electric interactions that require constructive modifications of the traditional real-space vector field topological approach, appropriate for magnetic system. Note, first, that the absolute value of the polarization vector \mathbf{P} , which is the order parameter in ferroelectrics, is not entirely fixed. Also, the considerable anisotropy effects lift the degeneracy of the system with respect to rotation of \mathbf{P} . This implies that the standard definition of the order parameter space S^n as a space with $|\mathbf{P}(\mathbf{r})| = \text{const}$ or, equivalently, as a space of the unit vector $\mathbf{p} = \mathbf{P}/|\mathbf{P}|$ is not a fully appropriate tool for the description of the topological formations in ferroelectrics.

The use of the 1D and 2D coordinate spaces, \mathbb{R}^1 and \mathbb{R}^2 , is not completely applicable for the description of such ferroelectric low-dimensional structures as nanowires and films. This is because in ferroelectrics, the coherence length ξ_0 , defining the crossover from the low-D to 3D geometry of the system, is of the order of several nanometers. This is extremely small compared to coherence lengths of about tens of nanometers in magnetic systems. Consequently, the ferroelectric nanostructures should be considered as 3D particles, cylinders, and plates, described by the corresponding 3D manifolds \mathcal{M} confined by boundaries $\partial\mathcal{M}$, rather than low-D objects, unless their confinement scales are indeed as small as atoms. Moreover, this confinement results in depolarization effects that play a primary role in the formation of topological states in ferroelectrics.

The most significant distinction influencing the formation of topological states in ferroelectrics versus magnetic materials lies in the difference in magnitudes of the respective depolarization and demagnetization forces. As noted in the previous Section, the strength of the depolarization effect in ferroelectrics is characterized by a large factor, $\kappa = 2C/\varepsilon_b T_c \simeq 10^2$. In contrast, the analogous parameter in magnetic materials, derived from Curie susceptibility well below the transition temperature, is estimated as $\chi \simeq n\mu_0\mu_B^2/3k_B T_c$ [143], yielding values of only 10^{-4} to 10^{-5} . Here, μ_B represents the Bohr magneton, k_B is the Boltzmann constant, $n \simeq 27 \text{ m}^{-3}$ is the concentration of magnetic ions, $T_c \simeq 100\text{--}1000 \text{ K}$ is the Curie temperature, and μ_0 is the vacuum permeability. This indicates that demagnetization forces provide only a minor correction to the energy of the magnetic state. The disparity of over six orders of magnitude leads to fundamentally different physics governing the topological states in magnetic and ferroelectric materials.

The huge depolarization contribution breaks, for instance, down the topological real-space classification of the states in ferroelectrics widely used for magnetic systems. Consider, for illustration, vortex topological states in thin films shown in Fig. 2(a). While two of them, V_{cw} and V_{ccw} , carry the divergence-free polarization fields, which are not affected by the depolarization energies, two other, V_{in} and V_{out} , do produce bound charges, depicted by plus and minus symbols in Fig. 2(a). The emergence of bound charges costs enormous depolarization energy, pushing the star-like vortices out of the topological degeneracy class to which belong the CW- and CCW-rotating vortices. Accordingly, switching vortex state from V_{cc} to V_{ccw} via the continuous rotation of the polarization vector, hence by passing through the intermediate charged vortices V_{in}^* and V_{out}^* , shown in Fig. 2(b) by the dashed red line, is much less energetically favorable than the same switching but occurring via destroying the ferroelectric order parameter and passing through the paraelectric phase, P , having a much weaker energy barrier shown by the dashed blue line in Fig. 2(b).

The more diverse situation arises when considering the skyrmion topological states. Similar to the star-like vortices, huge bound charges associated with the emergence of V_{in} and V_{out} , emerge in the Néel-type skyrmions, S_{in} and S_{out} , because of the arising divergence of the polarization vector field. Furthermore, the Bloch-type skyrmions, S_{cw}^\pm and S_{ccw}^\pm , also produce bound charges at the central and periphery regions of skyrmion where polarization hits the surface of the film, see Fig. 2(c). This feature discriminates Bloch and Néel skyrmions on the basis of their formation energy costs

unless some special conditions for the charge screening significantly reduce the depolarization effects. Note that skyrmion formation in magnetic systems is usually driven by the local asymmetric Dzyaloshinskii–Moriya interaction (DMI). In ferroelectrics, this type of interaction commonly does not exist, and the formation of the topological structures is governed by the electrostatic confinement phenomena. Let us also note that in magnetism, the magnetostatic interaction can either enhance or compete with the DMI [144–151]. However, it does not play as decisive a role as in ferroelectrics because it is significantly weaker.

Another essential difference between ferroelectricity and magnetism lies in the symmetric properties of their vector order parameters. Polarization in ferroelectrics, arising from ionic displacement, is a polar vector that changes direction under mirror reflection. In contrast, magnetization in magnetic materials, originating from spin degrees of freedom, is an axial vector that retains its direction under mirror reflection. This fundamental distinction significantly influences the symmetry and response of these materials to external fields. For example, in magnetic materials, a Néel-type skyrmion changes its direction under mirror reflections, making it a chiral object. In contrast, a Néel-type ferroelectric skyrmion is invariant under mirror transformations. At the same time, Bloch-type skyrmions, both in magnetism and in ferroelectricity, change their orientations under mirror reflections, hence are chiral.

4. Topological hydrodynamics of ferroelectricity

4.1. Polarization dynamics

4.1.1. Streamline approach

We develop a consistent topological approach to ferroelectrics accounting for the necessity of eliminating the huge depolarization contribution, which fundamentally determines the topological properties of ferroelectrics. As we have pointed out above, the depolarization field is produced by the bound charges $\rho = -\text{div } \mathbf{P}$, hence the stable state of the polarization distribution in ferroelectrics tends to be divergence-free. The central point of the topological approach in ferroelectrics is the consideration of polarization fields satisfying the condition $\text{div } \mathbf{P} = 0$. This condition is essentially different from the constraint of the invariance of the order parameter amplitude, $|\mathbf{P}(\mathbf{r})| = \text{const}$, used in the real-space vector field approach, which does not account for the depolarization energy.

As a consequence of the requirement $\text{div } \mathbf{P} = 0$, the polarization field strives to be tangential to the surface of the sample to avoid the formation of the surface depolarization charges. This discloses the fundamental importance of the boundary confining the ferroelectric within the finite volume for the topological theory of ferroelectrics. Taking the coordinate space \mathcal{M} of the ferroelectric system as a 3D manifold with boundary $\partial\mathcal{M}$, we face by far more complex problem than that in magnetic systems, where the usually considered coordinate spaces are without boundary, i.e., are either infinite \mathbb{R}^n or closed S^n .

We establish here a description based on the streamlines of the polarization distribution in ferroelectric topological states. The streamline approach originates from hydrodynamics where streamlines are useful to represent the velocity field $\mathbf{v}(\mathbf{r})$ of ideal fluids [152]. The most important property for our purposes is that, in the case of incompressible fluids characterized by the condition $\text{div } \mathbf{v} = 0$, the streamlines are typically endless. Each line is either closed or continuously fills some volume, or goes to infinity in unbounded systems. It could also approach saddle singular points or other invariants sets and make arbitrary links, see [153–155].

The streamline of a vector field $\mathbf{V} = (V_x, V_y, V_z)$, starting from a point $\mathbf{r}_0 = (x_0, y_0, z_0)$, is defined parametrically via $\mathbf{r} = \mathbf{r}(\mathbf{r}_0, t)$ as the solution of the equation

$$\frac{dx}{V_x} = \frac{dy}{V_y} = \frac{dz}{V_z} = dt, \quad (17)$$

where t is the parametrization variable that traces out the path of the streamline from its initial point \mathbf{r}_0 .

In the case of a stationary steady flow of an ideal fluid, the streamlines present the trajectories of the moving particles of the fluid. In this case, the vector \mathbf{V} represents the velocity vector \mathbf{v} , and the parameter t is the time of motion of the particle along the line. In ferroelectrics, the vector \mathbf{V} represents the polarization vector \mathbf{P} . However, in this case, there is no actual particle movement. Instead, the parameter t serves as an auxiliary variable, acting as a coordinate along the polarization streamline. Importantly, the family of appropriately parametrized streamlines $\mathbf{r}(\mathbf{r}_i, t)$ of the polarization field $\mathbf{P}(\mathbf{r})$, where index i enumerates the starting points, fully determines the field $\mathbf{P}(\mathbf{r})$. The field vector corresponding to the point $\mathbf{r}_1 = \mathbf{r}(\mathbf{r}_0, t_1)$ of the line $\mathbf{r}(\mathbf{r}_0, t)$ (and tangential to this line) is determined as $\mathbf{P}(\mathbf{r}_1) = (d\mathbf{r}(\mathbf{r}_0, t)/dt)_{t=t_1}$.

The consideration of divergence-free polarization fields in confined ferroelectrics in terms of the topology of their streamlines is advantageous as compared to the vectors-based technique since it explicitly ensures the divergence-free character of the polarization field via the requirements that the streamlines are typically continuous, nonterminating, and localized within a confined volume. This correspondence between polarization fluxes in ferroelectrics and fluid flows allows for the topological description of polarization states using a generalized hydrodynamic approach. This approach studies the dynamics of streamlines and vortex lines by interpreting, as V. Arnold has established [52,156], the dynamic equations as geodesic flows of right-invariant energy metrics on infinite-dimensional objects, specifically groups of volume-preserving diffeomorphisms.

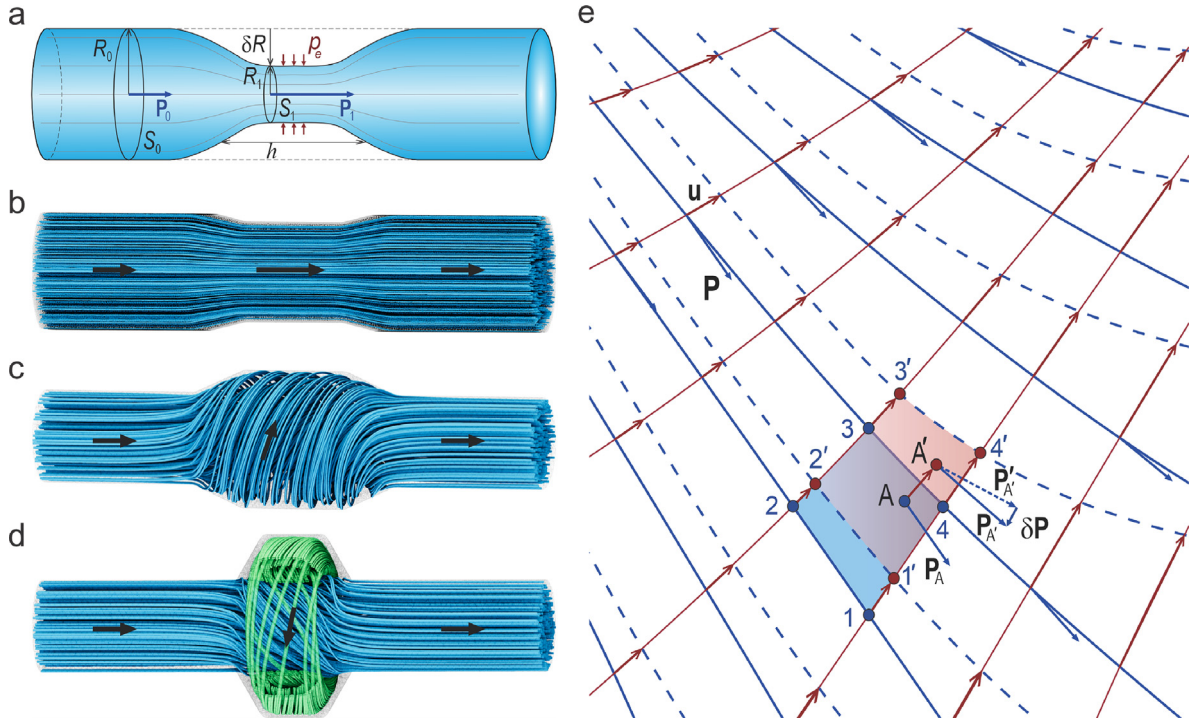


Fig. 5. Topological hydrodynamic approach; panels (b)–(d) show numerical simulations of streamlines. (a) Concept of Bernoulli principle. (b) Densification of polarization streamlines in a tube with local narrowing. The black arrow shows the magnitude and direction of polarization. (c) Helical swirling of polarization streamlines in a tube with local broadening. (d) Formation of the doughnut-like stream with a compensating counter-directed helical flux at the periphery of the broad part of the tube. (e) Deformation of streamlines of the polarization $\mathbf{P}(\mathbf{r})$ under the action of a volume-preserving diffeomorphism $\delta \mathbf{u}(\mathbf{r})$.

It is important to note that the representation of the polarization distribution in the form of streamlines is continuous, although it is constructed by interpolating discrete polarization dipoles located at the lattice nodes. As mentioned in Section 3.1, see also [132,133], the transition from a discrete to a continuous representation of the dipolar system is valid when the system size and the characteristic size of inhomogeneities exceed the coherence length, typically on the order of several nanometers. For graphical purposes, we apply smooth interpolation of the polarization lines at smaller scales, which enhances the visualization of the polarization field.

As a further generalization, the application of the method of streamlines for ferroelectrics would be interesting to consider the situation beyond the steady flow approximation and to incorporate the dynamics with the real-time parameter t into the formalism. The possibility of describing the motion of domain walls in ferroelectrics using hydrodynamic methods was proposed in [157,158].

4.1.2. Bernoulli principle

The Bernoulli principle is a foundational principle of hydrodynamics that provides the understanding of fluid flow behavior and connects fluid mechanics to other areas of physics, making it an essential starting point for grasping basic and complex fluid dynamics. The Bernoulli principle states that in a steady, incompressible flow of an ideal fluid through a straight tube with a variable cross-section, an increase in the fluid velocity results in a decrease in its pressure, and vice versa [152]. To analyze this correspondence, let us consider a uniform ferroelectric polarization flux along an infinite cylindrical tube of radius R_0 . This tube contains a narrowed segment, which has a reduced radius R_1 , with $R_1 < R_0$, see Fig. 5(a). Due to the polarization field's divergence-free nature, the polarization flux's value is conserved along the cylinder. This conservation establishes the relationship between the polarization P_0 in the infinite part of the cylinder, and the polarization P_1 in its narrowed segment, such that $\pi R_0^2 P_0 = \pi R_1^2 P_1$. Notably, the value of the polarization P_0 in the infinite part of a cylinder is equal to its equilibrium value, provided by the solution of the uniform GLD equation, $\partial F_P / \partial P = 0$, and corresponding GLD energy density is equal to its equilibrium value $F_0 = F_P(P_0)$, where $F_P(P)$ corresponds to the uniform part of GLD functional (9). At the same time, $P_1 = (R_0/R_1)^2 P_0$ is larger than P_0 , which results in the increase in the GLD energy density of the ferroelectric in the considered short segment, $F_1 = F_P(P_1)$, above F_0 . Importantly, this out-of-equilibrium state, P_1 , is not a solution of the GLD equation $\partial F_P / \partial P = 0$ which shows that the constraint $\text{div } \mathbf{P} = 0$ takes us beyond the class of the equilibrium solutions of this equation.

We now calculate the system's reaction to the increase in energy density from F_0 to F_1 in the segment. To that end, we consider the work necessary to narrow this segment from radius R_0 to R_1 , $\delta\mathcal{W} = -p_e 2\pi R h \delta R$, where p_e is the external pressure of the compressive force applied to the surface of the segment, see Fig. 5(a). This work is done to change the internal GLD energy of the segment,

$$\delta\mathcal{F}_P = \delta(VF_P) = F_P \delta V + V \delta F_P = \left[F_P + \frac{1}{2} R \frac{\partial F_P}{\partial P} \frac{\partial P}{\partial R} \right] 2\pi R h \delta R = \left[F_P - \frac{\partial F_P}{\partial P} P \right] 2\pi R h \delta R. \quad (18)$$

In the last term, the condition $\partial P / \partial R = -2P / R$, which follows from flux conservation, was applied. By equating $\delta\mathcal{W} = \delta\mathcal{F}_P$, we obtain $p_e = (\partial F_P / \partial P) P - F_P$. Taking into account that, according to the mechanical stability condition, the total pressure, p_{tot} – which is the sum of the internal elastic pressure, p , and the applied external pressure, p_e – should remain constant along the entire tube, we derive the generalized Bernoulli law,

$$p_{tot} = p + \frac{\partial F_P}{\partial P} P - F_P = \text{const}. \quad (19)$$

The relation (19) generalizes the classical Bernoulli equation for inviscid incompressible fluids, $p + \frac{1}{2} \rho \mathbf{v}^2 = \text{const}$, where the energy is given by $F = \frac{1}{2} \rho \mathbf{v}^2$ and ρ is the fluid density, to ferroelectrics with a more complex form of the energy density, $F_P(P)$. We conclude that variations in the polarization field lead to variations in the internal stress of the medium, which is of a ponderomotive nature, similar to the ponderomotive stress exerted by internal electric or magnetic fields [132].

Fig. 5(b) shows the simulation of the ferroelectric flux in a long cylindrical ferroelectric with a local narrowing in the middle, based on the numerical solution of the Ginzburg–Landau equations described in Section 3.1. The polarization streamlines become denser in the narrow region of the tube, indicating a polarization amplitude increase, which is consistent with the flux conservation law. However, in the case of a local thickening of the tube, demonstrated in Fig. 5(c), the polarization streamlines exhibit an unusual behavior. Instead of uniform sparsifying of the lines with decreasing polarization amplitude, as observed in fluids, they swirl into a helical structure, rotating around the tube axis. Such a configuration is indeed energetically more favorable than the laminar one. In the helical rotating texture, the polarization vector acquires transversal components enabling it to maintain an amplitude close to the equilibrium value while conserving the constancy of the flux.

An interesting situation arises with the further local broadening of the tube above a certain critical radius. Then a new type of a doughnut-like formation of closed streamlines appears upon approaching the boundary of the thickened segment, as shown in Fig. 5(d). In the inner part of the doughnut, the polarization lines wind around the doughnut, matching the helically-screwed lines of the original flow that comes from the regular, non-widened tube part and pierces the doughnut. In the outer part of the doughnut, they form a compensating counter-directed helical stream, thus, the contribution of the streamline doughnut to the total flux of the polarization along the tube vanishes. This assists in the invariance of the flux of the central flow with no substantial perturbation in the wider part of the tube.

Bernoulli equation (19) is valid for a uniform potential flow with no vorticity. The helical screwing and the doughnut-like wrapping of the polarization flux, presented in Fig. 5(c,d) takes us out of the class of the flows, described by (19). Describing streams with vorticity in an inviscid incompressible fluid requires the more general stationary Euler equations, obtained by variation of full non-uniform GLD functional \mathcal{F}_f (9). In the next Section, we derive the corresponding equation for the polarization streamlines, which is a core equation of topological hydrodynamics in ferroelectrics.

4.1.3. Euler equation

The derivation of the Euler equation for ferroelectrics is based on the consideration of the mechanical stability of a non-uniformly distributed polarization field $\mathbf{P}(\mathbf{r})$ with $\text{div} \mathbf{P} = 0$, shown in Fig. 5(e) by blue streamlines. Our analysis is based on the variational approach [52], utilizing the virtual infinitesimal deformation of the ferroelectric material under the action of a volume-preserving diffeomorphism $\mathbf{r} \rightarrow \mathbf{r} + \delta \mathbf{u}(\mathbf{r})$. The small displacement field $\delta \mathbf{u}(\mathbf{r})$, with $\text{div}(\delta \mathbf{u}) = 0$, is shown in Fig. 5(e) by red streamlines.

Let us consider the elementary volume 1234 that is transformed to 1'2'3'4' under the perturbation of $\delta \mathbf{u}(\mathbf{r})$. The variation of the GLD ferroelectric energy \mathcal{F}_f (9), $\delta\mathcal{F}_f = \int (\delta F_f / \delta \mathbf{P}) \delta \mathbf{P} dV$ (where the integration is done over the volume 1'2'3'4'), is provided by the variation of the polarization texture, $\delta \mathbf{P}$, under the diffeomorphism $\delta \mathbf{u}(\mathbf{r})$. Specifically, for point A' , displaced from point A , $\delta \mathbf{P} = \mathbf{P}'_{A'} - \mathbf{P}_{A'}$, where $\mathbf{P}'_{A'}$ is the original (before diffeomorphism) polarization vector starting from A' , and $\mathbf{P}_{A'}$ is the polarization vector displaced from A under the action of the diffeomorphism. According to the formalism of differential geometry [52], the variation of the polarization field, $\delta \mathbf{P}(\mathbf{r})$, is defined by the Lie bracket $\{\cdot, \cdot\}$ of the fields $\mathbf{P}(\mathbf{r})$ and $\delta \mathbf{u}(\mathbf{r})$, $\delta \mathbf{P} = \{\mathbf{P}, \delta \mathbf{u}\} \equiv \nabla \times [\mathbf{P} \times \delta \mathbf{u}]$, and, hence, the energy variation is given by

$$\delta\mathcal{F}_f = \int \frac{\delta F_f}{\delta \mathbf{P}} \delta \mathbf{P} dV = \int \frac{\delta F_f}{\delta \mathbf{P}} \{\mathbf{P}, \delta \mathbf{u}\} dV = - \int \left(\mathbf{P} \times \left[\nabla \times \frac{\delta F_f}{\delta \mathbf{P}} \right] \right) \delta \mathbf{u} dV. \quad (20)$$

In the last step, the integration by parts was used.

The virtual energy variation $\delta\mathcal{F}_f$ is to be compared to the virtual work $\delta\mathcal{W} = - \int \nabla p_{tot} \cdot \delta \mathbf{u} dV$, performed during the displacement of the volume 1234, where the pressure p_{tot} is the total Bernoulli pressure given by Eq. (19), which we

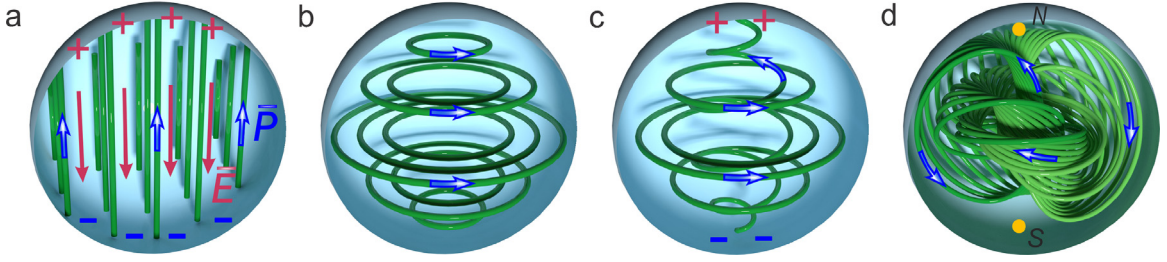


Fig. 6. Formation of the Hopfion. (a) A uniform distribution of the polarization, \mathbf{P} (green lines), in a spherical nanoparticle, blue arrows show the polarization direction. Positive and negative depolarization charges on the surface induce depolarization electric field, \mathbf{E} (red lines). (b) Polarization vortex. (c) Escape of the polarization vortex into the third dimension. (d) Polarization Hopfion. The yellow points show the singularities of the polarization field emerging at the North, N, and South, S, poles of the nanoparticle.

refer to as the Bernoulli function $\Psi_B(\mathbf{r})$. By equating $\delta\mathcal{F}_f$ and $\delta\mathcal{W}$, we obtain the mechanical stability condition for the polarization distribution:

$$\mathbf{P} \times \left(\nabla \times \frac{\delta F_f}{\delta \mathbf{P}} \right) = \nabla \Psi_B, \quad \Psi_B = p + \mathbf{P} \frac{\delta F_f}{\delta \mathbf{P}} - F_f. \quad (21)$$

This equation is a generalization of the stationary Euler–Lamb equation for fluids [152], which, with the energy density $F = \frac{1}{2} \rho \mathbf{v}^2$, is written as $\mathbf{v} \times (\nabla \times \rho \mathbf{v}) = \nabla (p + \frac{1}{2} \rho \mathbf{v}^2)$. It is also worth noting that Bernoulli equation (19) is a special case of (21) for a potential polarization distribution, where $\nabla \times (\delta F_f / \delta \mathbf{P}) = 0$.

Using the standard relations of vector calculus, and taking into account that $\text{div} \mathbf{P} = 0$, the Eq. (21) can be reduced to the form

$$(\mathbf{P} \nabla) \frac{\delta F_f}{\delta \mathbf{P}} = -\nabla p, \quad (22)$$

which is a generalization of the stationary Euler equation for fluids [52,152], $(\mathbf{v} \nabla) \rho \mathbf{v} = -\nabla p$.

The ponderomotive forces, resulting in the Euler equations, are naturally integrated into the mechanical condition of stability of the polarization field in ferroelectrics, expressed by the elasticity Eq. (13). Introducing the stress tensor of the polarization field,

$$T_{ij}(\mathbf{P}) = P_i \frac{\delta F_f}{\delta P_j} - \delta_{ij} F_f, \quad (23)$$

which is the generalization of the Maxwell stress tensor for electromagnetic fields [132] for the nonlinear polarization dynamics in ferroelectrics, we extend Eq. (13) as

$$\partial_i (\sigma_{ij} + T_{ij} + q_{ijmn} P_m P_n) = 0. \quad (24)$$

Then, the generalized Euler–Lamb (21) and Euler Eqs. (22) are recovered in the isotropic case where tensor q_{ijmn} has the symmetric form, $q_{ijmn} = q_1 \delta_{ij} \delta_{mn} + q_2 (\delta_{im} \delta_{jn} + \delta_{in} \delta_{jm})$, where q_1, q_2 are the material constants, and the shear stress is small. Interestingly, the structure of the equations remains unchanged under local rotations of the polarization vector field, $\hat{R}_{ij} P_j$. However, in general anisotropic case, the equation of mechanical stability loses its integrability, and the system becomes rather complex. Yet, Euler’s approach can be applied within certain limits due to the system’s stability, governed by the Kolmogorov–Arnold–Moser (KAM) theorem, specifically for divergence-free fields [52,159–161]. The KAM theorem outlines the conditions under which the topological structure of divergence-free fields persists despite perturbations, providing a measure of stability to the dynamic system. Section 5.2 explores this in detail, with specific application to ferroelectric systems. Additionally, it is worth noting that by considering only quadratic terms in polarization for $T_{ij}(\mathbf{P})$ the ponderomotive and electrostrictive effects can be unified.

4.2. Polarization topological states

4.2.1. Hopfions and vortices

Now we discuss the fundamental topological states of polarization, emerging in a confined nanostructured ferroelectric, specifically in a spherical nanoparticle [21]. As we mentioned in Section 3.2, a uniform polarization state is not energetically favorable because of the formation of surface-bound charges located at the termination points of polarization lines, see Fig. 6(a). Therefore, we consider the divergence-free polarization fields with the polarization vector tangential to the surface. The analogy with the hydrodynamics of an ideal fluid, in which the streamlines of the divergence-free velocity field the $\mathbf{v}(\mathbf{r})$ correspond to the streamlines of the divergence-free polarization field $\mathbf{P}(\mathbf{r})$, proves to be very useful in this context. To this end, we consider an incompressible, inviscid fluid in motion within a spherical volume. The fluid remains

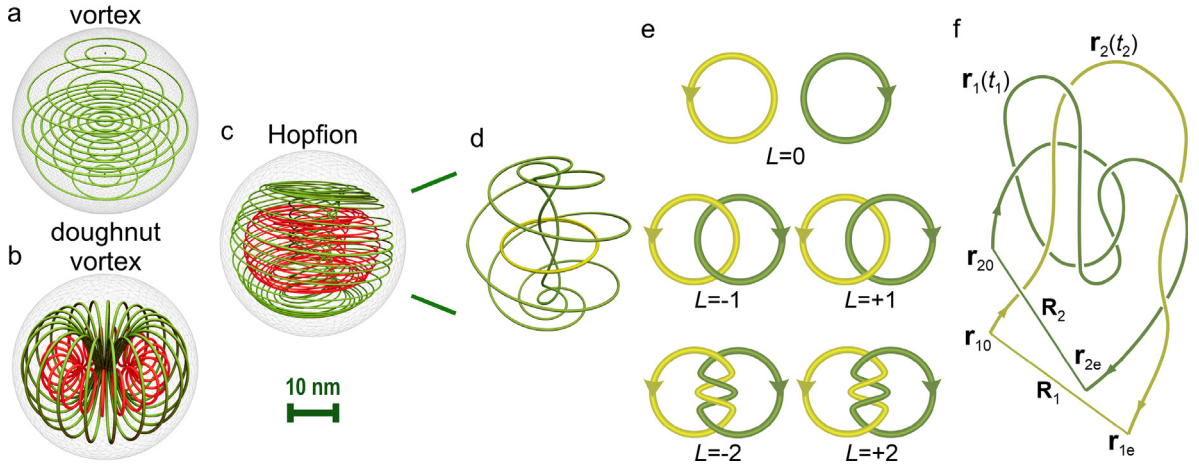


Fig. 7. Hopfion properties. (a) A straight vortex, the toroidal component of a Hopfion. (b) A doughnut vortex, the poloidal component of a Hopfion. (c) A Hopfion, the combination of the toroidal and poloidal components. (d) Exemplary polarization streamlines belonging in the tori shown in c that illustrate linking of streamline loops in the Hopfion. (e) Illustration of the topological linking numbers for closed lines, quantifying how many times the two lines wind around each other. (f) Illustration of the linking of two entangled streamlines.

in motion as long as its energy is not dissipated. Under these conditions, vortex flow is the most intuitively evident type of motion. Similarly, a ferroelectric vortex with the polarization vector tangential to the surface is a possible configuration that maintains the divergence-free character of the polarization field, as illustrated in Fig. 6(b). However, the formation of a vortex requires additional energy due to the existence of the vortex core, where ferroelectricity is suppressed.

A singularity at the vortex core can be eliminated by allowing the vector field to escape into the third dimension along the vortex axis, similar to how a fluid might form a helical flow to avoid a singularity. This forms a helical structure of the vector field, as illustrated in Fig. 6(c). However, this flux encounters the volume boundary, creating bound charges and an energetically unfavorable depolarization field. Analogous to a fluid spreading out to avoid pressure buildup, directing the flux into a back-flow over the sphere's surface keeps the vector field tangential to the surface, thereby eliminating the undesirable depolarization charges. This described structure, shown in Fig. 6(d), in which only two singular points on the vector field remain at the poles, is a fundamental topological state that we refer to as hydrodynamic Hopfion.

The concept of Hopfions, or more exactly Hopf fibrations, was first introduced by Heinz Hopf in the field of topology in 1931 [91] using concepts of the nontrivial homotopy group $S^3 \rightarrow S^2$. Its application Hopfions in hydrodynamics in terms of streamlines was later developed in the works of Moffatt and Arnold [52,162,163]. The implementation the mapping $S^3 \rightarrow S^2$ in the case of the ferroelectric nanoparticle will be discussed in Section 4.3.1. Note that despite the seeming similarity between the real-space magnetic Hopfions, Fig. 2(e), and hydrodynamic Hopfions, Fig. 6(d), – both of them realize the same nontrivial homotopy group $S^3 \rightarrow S^2$, studied by Hopf – there is an important difference in their construction. In the former case of magnetic Hopfion, the winding lines are the traces of the unit vector $|\mathbf{m}| = 1$ with the given direction, whereas in the latter case, these lines are the streamlines tangential to the field vectors.

Fig. 7 displays more details on the properties of Hopfions. As shown in panels (a)–(c), a Hopfion in an axially symmetric nanoparticle can be presented as a combination of two basic topological states: a vortex state, with a straight axis, coinciding with the vertical nanoparticle axis, see Fig. 7(a), and a doughnut vortex state, with the circular vortex axis entwining the nanoparticle axis, see Fig. 7(b). In ferroelectric literature, the doughnut vortices are also quoted as electrical skyrmion bubbles, skyrmion bubbles, polar bubble skyrmions, polar skyrmion bubbles, and torons [164,165]. We prefer to keep the term doughnut vortex, to avoid confusion with general terminology in which skyrmion is a purely 2D object whereas a bubble means any type of cylindrical domain or any other topological state formation of cylindrical shape. Notably, such a configuration was first introduced in the physics of elementary particles by Ia. B. Zel'dovich [166], where it was termed an anapole following a suggestion by B. L. Ioffe and A. S. Kompaneets.

In spherical coordinates (r, θ, φ) the toroidal-poloidal decomposition of the divergence-free vector field of the Hopfion is [162,167]

$$\mathbf{P} = \mathbf{P}_{\text{tor}} + \mathbf{P}_{\text{pol}} = \alpha_t \eta \mathbf{e}_\varphi + \alpha_p \nabla \times (\zeta \mathbf{e}_\varphi), \quad (25)$$

where $\eta = \eta(r, \theta)$ and $\zeta = \zeta(r, \theta)$ are scalar potentials, and α_t and α_p are the corresponding weights of the toroidal and poloidal components. For illustrative purposes, we select a simple form of the η - and ζ -potentials, reproducing qualitatively the topology of the toroidal and poloidal components of streamlines, maintaining the polarization tangential to the nanoparticle surface, and enabling analytical calculations as

$$\eta = \sin\left(\frac{\pi r}{2R}\right) \sin \theta, \quad \zeta = R \frac{\sin(\pi r/R)}{r/R} \sin \theta. \quad (26)$$

In a Hopfion, polarization lines form the upcoming flux in the central region and the compensating down-coming flux at the periphery, making the total flux equal to zero. Herewith the polarization lines turn out to be wound on a system of tori concentrically nested around the central ring encircling the vertical nanoparticle axis. The important property of the polarization vector field of Hopfions is the entanglement of the streamlines. As illustrated in Fig. 7(d), any two streamlines, winding either around the same torus or around the different tori, are knotted with each other. The situation is different for the straight and doughnut vortices in which the streamlines form the rings that are not linked. The exemplary types of knots, having different linking numbers L , quantifying how many times the two lines wind around each other, are illustrated in Fig. 7(e). The more complex pattern of streamlines' entanglement is shown in Fig. 7(f). In Section 4.3.2, we will discuss in detail how the linking of streamlines relates to the topological properties of the polarization field in the nanoparticle.

4.2.2. Handedness and helicity

An important property of Hopfions is their chirality, or handedness, a concept introduced by Lord Kelvin in 1894, which is defined as a fundamental asymmetry property describing systems, distinguishable from their mirror images. The concept of chirality provides a remarkable addition to the foundational pillars of our world that applies to a wide multiplicity of sciences ranging from particle physics and life science to the structure of the universe [168–171]. The chirality of materials has become a key focus in modern materials science, particularly regarding materials that exhibit exceptional optical, plasmonic, biochemical, and pharmaceutical properties.

The handedness of Hopfions has a topological origin, stemming from the helical structure of the winding lines that form them. The Hopfions, H_{cw}^- and H_{ccw}^- , shown in Fig. 2(e), are related to each other via the mirror image symmetry operation. They give the example of the right-hand and left-hand chiral formations. The concept of topological chirality in Hopfions brings in far-reaching generalizations to other fields, in particular the description of chiral topological linking of the streamlines of electromagnetic field in plasma magneto-hydrodynamics and astrophysics [162], and of the fluxes in streaming fluids [52].

To reiterate, the emergence of topological chirality in ferroelectrics is not related to the underlying crystallographic group of the material. Instead, it arises from the long-range electrostatic forces within the confined volume of the nanomaterial. Structurally, handedness is created by the interplay between the central helix-like flux and the opposite peripheral helix-like flux. Typically, the central part of the Hopfion dominates, determining the overall handedness of the nanoparticle [21]. We show in Section 4.3.2 on more general basis that the chirality is remarkably realized in nanostructured ferroelectrics in the form of the linked streamlines.

The topological quantity that characterizes chirality of hydrodynamic Hopfions is helicity [52,162,163],

$$\mathcal{H} = -\frac{1}{(8\pi)^2} \int_{\mathcal{H}} \mathbf{P} \cdot \mathbf{A} dV = -\frac{1}{(8\pi)^2} \int_{\mathcal{H}} \epsilon_{ijk} A_i \partial_j A_k, \quad (27)$$

where the integration is carried out over the Hopfion cell \mathcal{H} , and \mathbf{A} is the vector potential of the divergence-free field \mathbf{P} , $\mathbf{P} = \nabla \times \mathbf{A}$. This expression does not depend on the specific choice of the vector potential \mathbf{A} , which is defined up to the addition of the gradient of a harmonic function ∇f in a simply connected manifold [52]. The second integral in (27) has a universal metric-independent Chern–Simons form widely used in the field theory [172]. In particular, since \mathbf{P} is frozen into deformations of the metric coordinate space, the helicity is a preserved quantity under the action of a volume-preserving diffeomorphism of \mathcal{H} , see Section 4.1.3 [52]. Note that we apply the hydrodynamic terminology for helicity \mathcal{H} [52], whereas in magnetism, helicity serves as the quantitative parameter that differentiates between Bloch and Néel skyrmions [102], see Section 2.3.3.

The helicity defined by expression (27) coincides with the topological charge of magnetic Hopfions (8) (with $\mathbf{P} = \mathbf{F}$), but it does not necessarily assume only integer values and can be a continuous variable. Its specific value depends on the degree of the reversal of the polarization vector with respect to the Hopfion axis, which changes when we move from the core region of the Hopfion to its periphery. It is equal to one (or to minus one) for a complete Hopfion with 180° polarization turn, and is zero when the Hopfion degenerates into a vortex state with the polarization vector lying in the equatorial plane. In other cases, it usually takes the intermediate values, being positive for right-hand Hopfions and negative for left-hand Hopfions.

The helicity of any divergence-free vector field on a three-dimensional simply connected manifold can be considered as a natural extension of the integral definition of the Hopf invariant. The topological nature of helicity follows from its conservation under any volume-preserving diffeomorphism of the system, including volume-preserving deformations.

Remarkably, the structural handedness of the polarization field in ferroelectrics can be altered by appropriately varying the electric fields or circular-polarized light [51,82,173–181]. This unique characteristic sets ferroelectric chiral systems apart from materials where chirality is a fixed, inherent property established during synthesis and unchangeable thereafter. The ability to switch handedness in ferroelectric materials provides unprecedented flexibility and control, enabling the development of advanced applications in areas such as tunable photonics, adaptive materials, and responsive biomedical devices. This tunable chirality opens new avenues for research and technology, offering capabilities that usual chiral materials cannot match.

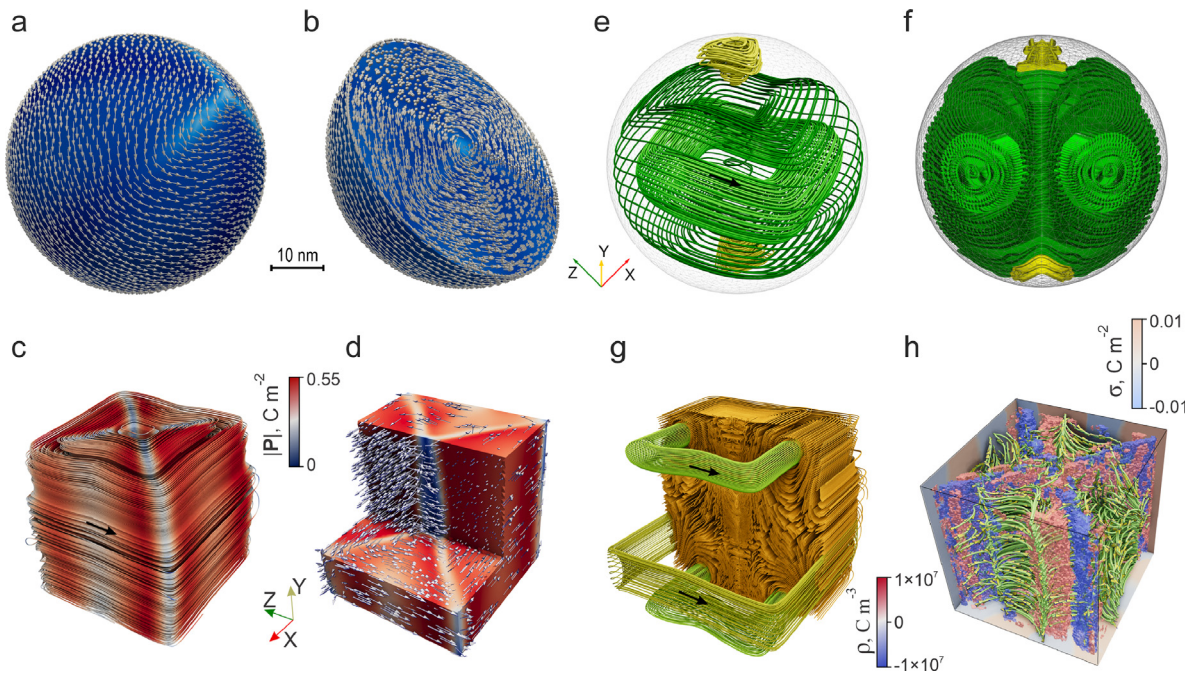


Fig. 8. Topological polarization states in PZT nanoparticles. Numerical simulations. (a) Distribution of the polarization vector field at the surface of a spherical nanoparticle. (b) Polarization vector field at the equatorial cross-cut of the spherical nanoparticle. (c) Polarization streamlines emerging at the surface of a cubic nanoparticle. (d) Polarization vector field at the corner cut of the cubic nanoparticle. (e) Distribution of the polarization streamlines in the spherical nanoparticle revealing the topological states, Hopfion (at the center) and vortices (at the poles). (f) Vertical cross-cut of the spherical nanoparticle, demonstrating the Poincaré map of polarization streamlines. (g) Cross-sectional Poincaré map of the cubic nanoparticle and several sets of streamlines emerging in volume and revealing their tori winding structure. (h) Distribution of the electric field in the cubic nanoparticle is shown by green streamlines. The volume bound charges, ρ , and the surface bound charges, σ , charges are shown by a red–blue maps.

4.2.3. Polarization field in nanoparticles

Free-standing ferroelectric nanoparticles appear as a basic setup providing a material ground for the study of the topology of polarization streamlines in confined systems. Fig. 8 shows the polarization distribution in a spherical ferroelectric nanoparticle with a radius of $R = 25$ nm and a cubic nanoparticle with dimensions $60 \times 60 \times 60$ nm, as obtained from phase-field simulations. The $\text{PbZr}_{0.6}\text{Ti}_{0.4}\text{O}_3$ (PZT) compound is chosen as the nanoparticle material because, at this Ti concentration, the compound is near the morphotropic phase boundary, where the polarization vector is only slightly pinned by crystal anisotropy. When passing through this point, the polarization vector rotates from the [001] crystallographic orientation, corresponding to the tetragonal phase stable at higher Ti concentration, to the [111] crystallographic orientation, corresponding to the rhombohedral phase stable at lower Ti concentration.

The initial view of the polarization vector distribution, $\mathbf{P}(\mathbf{r})$, across the nanoparticle's surface, as shown in Fig. 8(a), reveals a configuration that closely resembles a vortex with three-fold symmetry, oriented along the [111] crystallographic direction. To avoid energetically unfavorable depolarization charges, the polarization vector remains tangential to the surface, resulting in two singularities at the poles. According to the Poincaré (Hairy Ball) theorem, see Section 2.2.4, these singularities are unavoidable, as it is impossible to have a continuous tangential vector field located on a closed simply connected surface without having some singular points. Upon examining an equatorial cut of the nanoparticle, the polarization vector distribution suggests the presence of six flux-closure domains, forming the vortex, see Fig. 8(b). A similar situation occurs in the cubic nanoparticle, where a vortex with a four-fold symmetry axis is observed through the streamlines emerging at the nanoparticle's surface, see Fig. 8(c). The corner cross-cut suggests the presence of four flux-closure domains, forming the vortex, see Fig. 8(d).

However, the more detailed study of the polarization vector field in the spherical nanoparticle in terms of streamlines demonstrates that in fact, the volume of the nanoparticle splits into three topological states, as shown in Fig. 8(e). The major part of the volume then is occupied by a Hopfion, shown in green, whose structure is similar to that of the model case discussed in Section 4.2.1, but deformed due to the residual crystal anisotropy. Two small cells in the vicinity of the poles are hosting the tiny vortices shown in yellow. Fig. 8(f) shows the vertical cut of the spherical nanoparticle, providing a clear identification of the internal streamline structure. The 2D plane of the cut section, known in mathematics as a Poincaré section or Poincaré map [182], is transversal to the system's flow. It shows the streamlines that intersect this section and tracks the points where these streamlines start and return to the section. The system of nested tori, around

which the streamlines wind, appears at this intersection as two sets of concentric cross-sectional ellipses. The similar cut of the cubic particle is shown in Fig. 8(g). The structure of the Poincaré map is now by far more complex. Yet by allowing part of the streamlines to go outside the intersection while keeping their 3D character, it is immediately evident that the streamlines preserve their tori-winding configuration.

The polarization configurations, presented above, were calculated for ferroelectric nanoparticles in a vacuum where the polarization is zero. In this case, the polarization vector field remains tangential to the surface, while any normal-to-the-surface component of the field would imply a nonzero divergence at the surfaces, which would cost depolarization energy. However, in the case where the ferroelectric is embedded into the polarizable dielectric medium, the polarization flux can overflow from the nanoparticle to the space outside, making the nanoparticle surface semi-transparent. We foresee the possible escape of the polarization lines from the Hopfion-like textures in ferroelectric nanoparticles in the case where one puts them into high- ϵ dielectric media. This flux emergence would help to avoid the pole singularities of the polarization field. However, this effect is expected to be small. The effects of the polarization field emerging beyond the ferroelectric nanospecies can also be included into the general topological consideration of Arnold hydrodynamics. In fact, the outcoming polarization streamlines are continuous at the dielectric–ferroelectric interfaces and localized within the narrow layer close to them. The polarization vanishes as we are moving away from the interface; otherwise, polarizing the external media would cost substantial energy. Placing the bounding surface slightly outside of the ferroelectric, where the induced polarization is already zero, we satisfy the condition of the zero tangential polarization.

Notably, the expulsion of bound charges from the system is not perfect, and the system's polarization field can maintain a slight divergence to accommodate the deformed toroidal-winding streamline configuration to the nanoparticle's geometry. As shown in Fig. 8(h), the residual volume and surface bound charges, as well as the induced electric depolarization fields, remain relatively small, as we will discuss in Section 5.3.1. Remarkably, the well-structured patterns of streamlines observed in ferroelectrics have a profound topological origin, grounded in the core principles of topological hydrodynamics. These aspects, which are central to understanding the topology of ferroelectrics, are further discussed in Section 4.3.3.

4.3. Topology of polarization streamlines

4.3.1. Fibration. Homotopy group

In the hydrodynamic topology approach, streamlines are the principal constructive elements that describe the structure of the divergence-free polarization field. Streamlines indicate the direction of polarization at every point in space and typically never intersect each other or break off within the ferroelectric volume. They densely fill the space, realizing the topological concept of space fibration, in which each streamline represents a fiber. By representing the polarization field as a bundle of fibers, one can apply topological methods to study its properties. Accordingly, different polarization states are specifically classified by application of the general homotopy group approach, see Section 2.1.1. In this approach, when applied to streamline fibration, each streamline from the 3D nanoparticle manifold \mathcal{M} is mapped onto a point in the 2D degenerate space manifold D , parametrizing these streamlines, as illustrated in Fig. 9(a). This classification remains unchanged under small continuous streamline deformation. We consider the application of the homotopy group approach for the description of the Hopfion state, confined by the simply connected cell within a nanoparticle, which is the coordinate manifold \mathcal{M} , see Fig. 9(b).

The parametrization of the tori-winding streamlines confined into the cell \mathcal{M} can be executed using the flat deck D' located inside \mathcal{M} in between the central loop C'_1 , around which all the tori are nested, and the contour C'_2 embracing the core of the Hopfion. This deck allows to fully parameterize all the fibers inside \mathcal{M} since all the tori-winding streamlines cross D' . Here, each outcoming line is considered a new one, which terminates when it meets again the deck D' after one complete turn around torus. Then we make one-to-one mapping of D' onto a region D of a unit sphere S^2 , see Fig. 9(c). Under the mapping $D' \rightarrow D$, the external edge C'_1 of D transforms into an internal single point S in D because it corresponds to a single streamline in D' . At the same time, the inner contour C'_2 in D' transforms into an external contour C_2 in D . As a result, the degenerate space D is a simply connected surface, containing the image of C'_1 as an internal point S and bounded by the contour C_2 corresponding to the internal contour C'_2 of the deck D' . The surface D forms a part of the sphere S^2 , where the point S is selected as the south pole and the contour C_2 encompasses the sphere above S . The region D , which, due to the one-to-one $D' \rightarrow D$ correspondence, unambiguously parametrizes the Hopfion streamlines, is useful as the degenerate space in the homotopy group approach. Then, the mapping $\mathcal{M} \rightarrow D$ defines the homotopy group describing Hopf fibration in the nanoparticle. Establishing the homotopy group $\mathcal{M} \rightarrow D$ allows us to consider two specific limiting cases. Note that the surface D is continuously deformable. This corresponds to the continuous deformations of the vector field conserving the principal constraint $\text{div } \mathbf{P} = 0$.

When the surface D shrinks to a single point, in particular to point S , all the preimages of the coordinate space \mathcal{M} map to the same structural unit, a horizontal closed loop corresponding to the vortex structure of the vector field with zero helicity.

When the surface D expands, extending over the whole sphere S^2 , and the edges of the contour C_2 shrink and map to the north-pole point N , the order parameter space becomes S^2 . In the real coordinate space, \mathcal{M} , this corresponds to the situation where all the streamlines at the nanoparticle's surface have a meridional direction and can be topologically identified with each other. We refer to such configuration as to a complete Hopfion. The streamlines of the complete

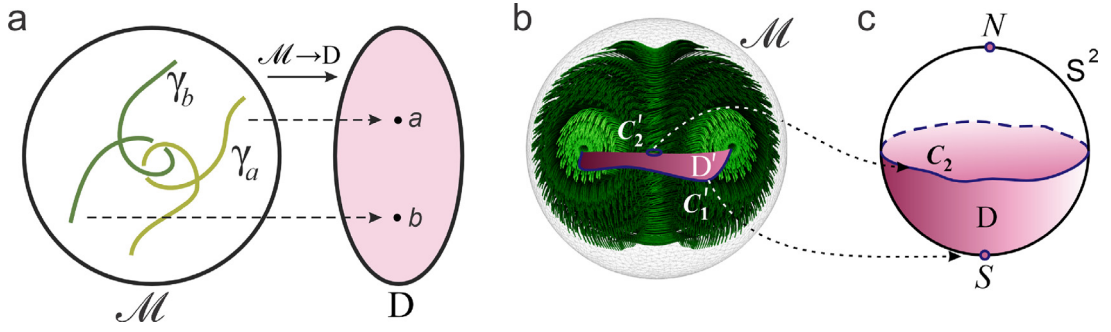


Fig. 9. Streamline homotopy in ferroelectric nanoparticles. (a) Concept of the homotopy group approach. The polarization field streamlines γ_a and γ_b from the 3D nanoparticle manifold \mathcal{M} map onto points a and b of the 2D degenerate space manifold D . (b) Cross-section of the nanoparticle manifold \mathcal{M} displaying the polarization vector field streamlines forming the Hopfion (taken from Fig. 8(f)). The rose-pink deck-area D' is used to parameterize the streamlines in the cell \mathcal{M} . It is embedded in between the central loop C'_1 , around which all the Hopfion tori are nested, and the contour C'_2 , embracing the core of the Hopfion. (c) The order parameter space D of the polarization Hopfion streamlines is shown in rose-pink. It is constructed by mapping the parametrization of the deck area D' (panel a) onto the part of the unit sphere S^2 . The external contour C'_1 of D' is mapped onto the single point, the south pole S of S^2 . The internal contour C'_2 is mapped onto the closed contour C_2 stretching over S^2 above S . The point N is the north pole of S^2 .

Hopfions can be expanded to the infinite space, S^3 , becoming uniformly directed streamlines at infinity. The resulting homotopy group in this case becomes $S^3 \rightarrow S^2$ and is characterized by the integer helicity (27).

Notably, the polarization distribution in the complete hydrodynamic Hopfion in S^3 is related to the real-space Hopfion of unit-vector $|\mathbf{n}| = 1$, described in Section 2.3.6 via transformation (5) with $\mathbf{P} = \mathbf{F}$. This relation shows that the order parameter space of the divergence-free field \mathbf{P} in a hydrodynamic Hopfion is topologically equivalent to the order parameter space S^2 of the unit vector \mathbf{n} in a real-space Hopfion [183]. Therefore, both types of topological states implement the same homotopy group $S^3 \rightarrow S^2$; that is why the Hopf fibration terminology is equally relevant for both of them. Furthermore, in the hydrodynamic case, the concept of the Hopf fibration is naturally generalized to the confined coordinate manifolds, generating, in particular, the considered here $\mathcal{M} \rightarrow D$ homotopy group. We point out here that the introduced unit gauge vector \mathbf{n} is not directly related to the unit vector of the normalized polarization field vector $\mathbf{p} = \mathbf{P}/|\mathbf{P}|$, and, therefore, using the latter to determine the Hopf index $N_3(8)$ of the polarization field \mathbf{P} is not entirely justified. Furthermore, the transformation (5), well defined for the systems in infinite coordinate spaces, faces the problem in the case of a confined coordinate space \mathcal{M} , where the condition of tangentiality of the polarization field to the manifold boundary has to be taken into account.

4.3.2. Linking and entanglement of streamlines

The intricate behavior of streamlines in ferroelectrics, shown in Fig. 8, reveals profound topological properties essential for understanding their dynamics. Even a single Hopfion topological state reveals the entanglement and linking between streamlines, see Fig. 7(d). In this Section we show that the complexity and linking of the streamlines are not merely geometric issues; they rather represent fundamental topological characteristics that connect deeply with other properties like helicity, energy conservation, and field stability.

Historically, the idea of the intertwined field lines has fascinated scientists since Lord Kelvin's 19th-century hypothesis that atoms might be vortex knots in the ether. While this specific notion has been set aside, the exploration of the knot-like structures in fields has persisted, with the topology becoming a central framework in modern physics systems, including classical and quantum fluids and superconductors [154,184–191], magnetic and optical fields [192–198], field theories [120,199,200], in liquid crystals, soft and biological matter [201–206]. These concepts provide powerful tools for understanding the complex behavior of physical fields. For example, in plasma physics, entangled magnetic field lines influence phenomena like solar flares. The study of knots in DNA and polymers, which affects genetic processes and cellular functionality, also parallels the entangled streamlines in ferroelectrics. Optical vortices in optics, which manipulate particles and enhance communication systems, showcase the application of knot theory in technology. This suggests a shared topological nature across different physical domains. As we already discussed, in ferroelectrics, the polarization field's streamlines, governed by the condition $\text{div } \mathbf{P} = 0$, form continuous paths that may wind around one another in complex ways, analogous to the behavior of streamlines in fluids or magnetic field lines in plasma.

The fundamental topological characteristic of streamline entanglement is the linking number, a key invariant that quantifies how these lines are interlinked in 3D space. To define the linking number, we first consider two closed curves, $\mathbf{r}_1(t_1)$ and $\mathbf{r}_2(t_2)$, with initial points $\mathbf{r}_{10} = \mathbf{r}_1(0)$ and $\mathbf{r}_{20} = \mathbf{r}_2(0)$, and the same terminal points $\mathbf{r}_{1e} = \mathbf{r}_1(T_1) = \mathbf{r}_{10}$ and $\mathbf{r}_{2e} = \mathbf{r}_2(T_2) = \mathbf{r}_{20}$. The parameters t_1 and t_2 trace out the paths of the curves, as described in Section 4.1.1. They run from 0 to T_1 for $\mathbf{r}_1(t_1)$ and from 0 to T_2 for $\mathbf{r}_2(t_2)$, respectively. The linking number for these curves is an integer that represents the number of times one curve winds around the other, with the sign indicating the direction of this winding,

see Fig. 7(e). It is calculated using Gauss' formula which provides a way to capture the entanglement between two closed curves,

$$L = \frac{1}{4\pi} \oint_{t_1} \oint_{t_2} \frac{\mathbf{r}_1 - \mathbf{r}_2}{|\mathbf{r}_1 - \mathbf{r}_2|^3} \cdot [d\mathbf{r}_1 \times d\mathbf{r}_2]. \quad (28)$$

In the topological hydrodynamics, streamlines are not always closed loops; they may instead densely fill a bounded space, or go to infinity, forming complex infinite trajectories. Extending the idea of linking to cases where the field lines are not closed, Arnold introduced the concept of the asymptotic linking. To illustrate this concept of asymptotic linking, let us consider the initial points \mathbf{r}_{10} and \mathbf{r}_{20} of the trajectories $\mathbf{r}_1(t_1)$ and $\mathbf{r}_2(t_2)$. By connecting these initial points to their respective terminal points \mathbf{r}_{1e} and \mathbf{r}_{2e} – reached at $t_1 = T_1$ and $t_2 = T_2$ (which are not necessarily the same as the initial points) – by the segments \mathbf{R}_1 and \mathbf{R}_2 , we create two closed loops, see Fig. 7(e). These loops may link with each other, and the corresponding linking number, which is the function of T_1 and T_2 , $L = L(T_1, T_2)$, provides a measure of the degree of the entanglement of these trajectories when they get extended through the space. By allowing the terminal parameters T_1 and T_2 to approach infinity, we obtain the asymptotic linking number which Arnold defined as:

$$L_a = \lim_{T_1, T_2 \rightarrow \infty} \frac{L(T_1, T_2)}{T_1 T_2}. \quad (29)$$

This quantity captures the long-term behavior of the entanglement between two trajectories as they evolve in length. The average linking number for a vector field $\mathbf{P}(\mathbf{r})$, which represents the number of times that each line, on average, winds around another, is obtained by averaging the asymptotic linking number over all pairs of streamlines, $(\mathbf{r}_{0i}, \mathbf{r}_{0j})$, parametrized by their starting points. This average quantity, written as

$$\bar{L}_{\mathbf{P}} = \langle L^a \rangle_{(\mathbf{r}_{0i}, \mathbf{r}_{0j})} = \mathcal{H}, \quad (30)$$

provides a global measure of the complexity and entanglement of the streamline configuration within the field, offering insights into the topological self-linking nature of the field itself. The second equality represents a crucial result in topological hydrodynamics, establishing the equivalence between the average linking number of streamlines and the helicity (27) of a topological state. According to Arnold helicity theorem, *for a divergence-free vector field on a simply connected manifold, the average self-linking of the field is equivalent to the helicity of the field.*

This theorem underscores the deep connection between the local entanglement of streamlines and the global topological invariant of helicity [52,163,207]. The equivalence between these two concepts is based on a fundamental principle called Poincaré duality, which connects physical objects of different dimensions in a space, revealing their topological interdependence. For instance, in electromagnetism, Gauss and Stokes theorems establish how lower-dimensional entities such as charges and currents are related to higher-dimensional quantities like electromagnetic fields and fluxes through surfaces or loops. In topological hydrodynamics, applying the principle of Poincaré duality allows for the calculation of essential global properties, such as field helicity, by analyzing the wrapping and twisting of the field's streamlines.

As an example of the application of Arnold helicity theorem, in Hopfions that possess distinct helicity, the field lines are entangled and exhibit non-zero average linking numbers, as illustrated in Fig. 7(d). In contrast, for vortices with no handedness, the linking numbers are zero, and all the vortex field lines are not linked. The sign of L is different for the left- and right-handed modifications of the knots of the winding streamlines, as illustrated in Fig. 7(e). This explains – from another perspective – why helicity is related to handedness.

The conception of entanglement of the streamlines in ferroelectrics is very important from a practical viewpoint. As we discuss in more detail in Section 6, it allows for the practical finding of the topology of nanostructured ferroelectrics in a straightforward and constructive experimental way, even in cases where the topological states are imperfect or affected by various external perturbations. Furthermore, the phenomena of entanglement and linking between streamlines in ferroelectric materials showcase complex interactions that resonate with fundamental physics principles seen across various scales. This is akin to quantum entanglement, where the state of one particle is inherently connected to another regardless of distance, highlighting a universal principle spanning quantum and classical fields.

The topological knotting and entanglement of streamlines in ferroelectric nanostructures resemble the dynamic topologies observed in the cited above physical systems, where field lines are intertwined and knotted. Exploring these linkages deepens our understanding of phenomena like energy conservation and field stability in ferroelectrics while enriching theoretical knowledge and inspiring practical innovations in materials engineering. As the research in this area progresses, new insights into the topological properties of materials and fields are likely to emerge, offering exciting possibilities for both theoretical exploration and practical applications.

4.3.3. Foliation and Arnold theorem

A remarkable aspect of the topological arrangement of streamlines in ferroelectrics, discussed in Section 4.2.3, is their tendency to lie entirely on closed surfaces, densely covering these surfaces; a phenomenon referred to as foliation in topology. For example, in the case of a Hopfion hosted by a spherical nanoparticle, the streamlines wind around a family of nested toroidal surfaces, as shown in Fig. 8(e,f). Another instance is a cubic nanoparticle, where the streamline surface sheets are observed in the vertical cut depicted in Fig. 8(g). Many of these sheets again exhibit a toroidal-winding or

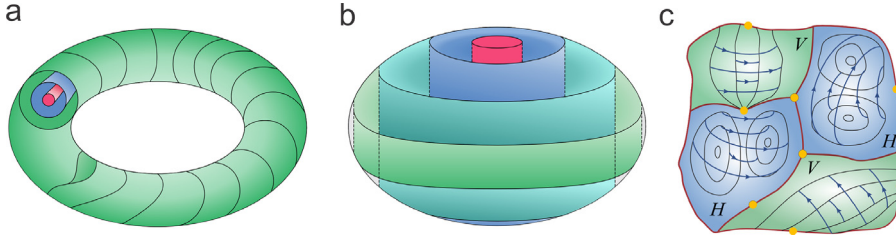


Fig. 10. Illustration of Arnold theorem. (a) Foliation of a topological cell into a set of nested tori around which the polarization streamlines wind. (b) Foliation of a topological cell into a set of concentric cylinders around which the polarization streamlines wind. (c) Cross-section of a nanoparticle, schematically illustrating the volume partition into cells hosting Hopfions, H , and vortices, V . The cell walls are shown in dark red. The black lines show the sections of the surface levels of the Bernoulli function, $\Psi_B(\mathbf{r})$. The streamlines of polarization winding around the surface levels of $\Psi_B(\mathbf{r})$ are shown in blue. The singular points of the polarization field are shown in yellow.

vortex-winding origin of the streamlines, although they are more intricate as compared to a single Hopfion in a spherical nanoparticle.

The propensity of streamlines to conform to 2D surfaces, such as nested tori or cylindrical vortex-winding surfaces, arises from the principles of topological hydrodynamics that define the configuration of polarization fields in these systems. We delve into the underlying topological principles governing these structures, established by Arnold [52].

First, we explain why the polarization streamlines are confined within 2D surfaces. These surface sheets densely fill the 3D manifold of a nanoparticle. To this end, we refer to the generalized Euler–Lamb equation (21), which presents a mechanical stability constraint for the divergence of the polarization field. We present this equation in the form

$$\mathbf{P} \times \mathbf{G} = \nabla \Psi_B, \quad \mathbf{G} = \nabla \times (\delta F_f / \delta \mathbf{P}), \quad (31)$$

where $\Psi_B(\mathbf{r})$ is the scalar Bernoulli function, defined by Eq. (21), and the introduced vector \mathbf{G} is divergence-free. It follows from Eq. (31) that the polarization vector field, $\mathbf{P}(\mathbf{r})$, as well as the vector field $\mathbf{G}(\mathbf{r})$, are orthogonal to the gradient field $\nabla \Psi_B(\mathbf{r})$, which, in turn, is orthogonal to the level surfaces of the Bernoulli function $\Psi_B(\mathbf{r})$. Therefore, both vector fields $\mathbf{P}(\mathbf{r})$ and $\mathbf{G}(\mathbf{r})$ are tangential to the level surfaces of the Bernoulli function $\Psi_B(\mathbf{r})$, and their streamlines are confined by these surfaces, *quod erat demonstrandum*. In other words, the Bernoulli function $\Psi_B(\mathbf{r})$ is the first integral of the polarization flow defined by the field $\mathbf{P}(\mathbf{r})$ in the space of a nanoparticle.

Notably, the foliation of the polarization field in ferroelectrics is a particular case of the Frobenius theorem, which is foundational in differential topology [208]. For smooth vector fields $\mathbf{P}(\mathbf{r})$ and $\mathbf{G}(\mathbf{r})$ defined on a smooth 3D manifold \mathcal{M} , this theorem is formulated as follows. Consider the vector field $\mathbf{V}(\mathbf{r})$ defined as the Lie commutator of the fields \mathbf{P} and \mathbf{G} , $\mathbf{V} = \{\mathbf{P}, \mathbf{G}\}$. Here, $\{\mathbf{P}, \mathbf{G}\} = \nabla \times [\mathbf{P} \times \mathbf{G}]$ represents the Lie bracket as defined in Section 4.1.3. If the field \mathbf{V} belongs to the subspace spanned by the fields \mathbf{P} and \mathbf{G} , that is, if at each point in \mathcal{M} it can be expressed as a linear combination of these fields, $\mathbf{V} = \alpha \mathbf{P} + \beta \mathbf{G}$, then there exists a smooth foliation of \mathcal{M} , with vector fields \mathbf{P} , \mathbf{G} , and \mathbf{V} tangential to the sheets of this foliation. In our case, as follows from Eq. (31), $\nabla \times [\mathbf{P} \times \mathbf{G}] = 0$, and the fields $\mathbf{P}(\mathbf{r})$ and $\mathbf{G}(\mathbf{r})$ commute, giving $\mathbf{V}(\mathbf{r}) = 0$, which constitutes the specific condition for the applicability of the Frobenius theorem.

In the next stage, we investigate the topological properties of the foliated surfaces around which the streamlines wrap. The fundamental theorem, established by Vladimir Arnold in the context of topological hydrodynamics for stationary fluid flows [52], limits the classes of such surfaces to nested tori and concentric cylinders. Arnold theorem, central to topological hydrodynamics, states: *Assume that the region $\mathcal{M} \subset \mathbb{R}^3$ is bounded by a compact analytic surface and that the field of velocities is analytic and is not collinear with its curl everywhere. Then the flow region for a stationary field can be partitioned by an analytic submanifold into a finite number of cells, in each of which the flow is constructed in a standard way. Namely, the cells are of two types: those fibered into tori invariant under the flow, see Fig. 10(a), and those fibered into the surfaces invariant under the flow, diffeomorphic to the annulus $\mathbb{R}^1 \times S^1$, see Fig. 10(b). On each of these tori, the flow lines are either periodic or quasi-periodic, and on annuli all flow lines are periodic.* The topological states composed of fibers entwined around the annuli are vortices, and the states composed of fibers entwined around the tori are Hopfions.

Arnold's proof of his theorem is concise and intuitively clear. It is based on the observation that any divergence-free stationary flow is a critical point of the energy among diffeomorphic or isovorticed fields. This implies Eq. (31), which means that the polarization field $\mathbf{P}(\mathbf{r})$, which is constrained by a similar variational principle, and the corresponding field $\mathbf{G}(\mathbf{r})$, are always tangential to the level sets of the Bernoulli function, $\Psi_B(\mathbf{r})$. To uniquely determine $\Psi_B(\mathbf{r})$, these nonsingular surface layers must either be closed and bounded or unbounded, intersecting the manifold boundary. According to the Poincaré–Hopf theorem, see Section 2.2.4, the only nonsingular closed-oriented surfaces that admit a non-vanishing tangential vector field are tori. Another possibility is that the winding surfaces are unbounded. In this case, they intersect the boundary of the manifold, forming annuli, as illustrated in Fig. 10(b).

The winding of the streamlines of two commuting vector fields $\mathbf{P}(\mathbf{r})$ and $\mathbf{G}(\mathbf{r})$ onto surface layers, defined by $\Psi_B(\mathbf{r}) = \text{const} = \varrho$, – where ϱ is the tori parametrization value – may be described in the local coordinates of tori,

$$\mathbf{P} = P_1(\varrho) \mathbf{e}_\vartheta + P_2(\varrho) \mathbf{e}_\varphi,$$

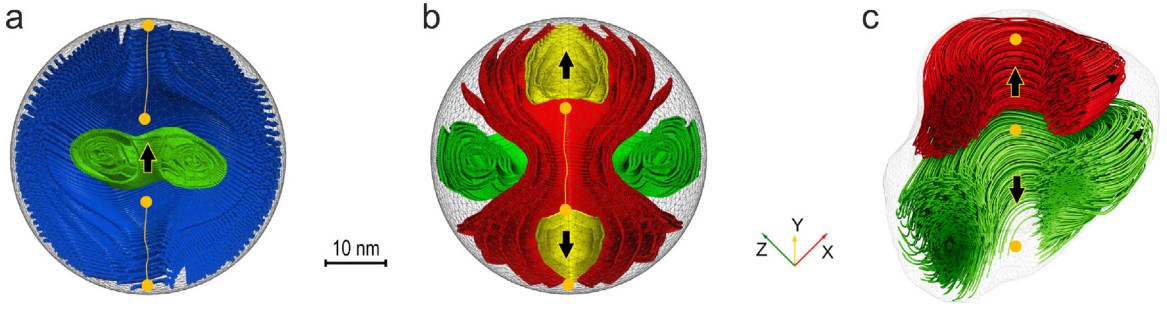


Fig. 11. Coexistence of different topological states in a ferroelectric PZT nanoparticle. Numerical simulations. (a) A vortex (in blue) envelops a Hopfion (in green). The yellow points indicate the singularities in the polarization field. The yellow lines indicate the linear vortex singularities. The thick black arrow indicates the direction of the average polarization flux at the center of Hopfion. (b) A vortex (in red) pierces a Hopfion (in green). Two additional local Hopfions (in yellow) emerge at the poles, each enveloped by a vortex. (c) Two Hopfions with the same polarization winding around the axis but opposite fluxes at the central part. The flux in the red Hopfion is upward, while in the green Hopfion it is downward. The thin black arrows indicate the polarization direction at the periphery of Hopfions.

$$\mathbf{G} = G_1(\varrho)\mathbf{e}_\theta + G_2(\varrho)\mathbf{e}_\varphi; \quad (32)$$

here \mathbf{e}_θ and \mathbf{e}_φ are the unit coordinate vector fields, tangential to the toroidal surface. The vector \mathbf{e}_φ encircles the tube of the torus, while the vector \mathbf{e}_θ loops around the torus central hole. The coefficients P_1 , P_2 , G_1 , and G_2 remain constant on the surfaces of the tori. Presentation (32) demonstrates that polarization flux $\mathbf{P}(\mathbf{r})$ forms a completely integrable Hamiltonian system with two degrees of freedom.

The implications of Arnold theorem for ferroelectrics are already seen in our model simulations of polarization states in a PZT spherical nanoparticle, shown in Fig. 8(e,f). The internal space of the nanoparticle is split into three cells. The biggest central cell hosts a Hopfion, shown in green, whereas the other two small cells at the nanoparticle poles, shown in yellow, contain the vortices. Importantly, the Arnold cells, partitioning nanoparticles can be multi-connected spaces. Fig. 11 offers further examples of Arnold partition of the PZT nanoparticle. These states, prepared under the application of an electric field, are metastable relative to the central Hopfion state depicted in Fig. 8(e,f). Fig. 11(a) shows the vortex which wraps around the nested cylindrical surface, depicted in blue. The green color represents the localized toroidal polarization lines of Hopfion, located inside a cavity at the center of the vortex. In Fig. 11(b) the vortex polarization lines, shown in red, rupture the central Hopfion part, shown in green, pushing it toward the equator. The secondary Hopfion states, shown by the yellow lines, are formed close to the poles. Two Hopfions with the same winding direction of rotation but with up- and downcoming fluxes at the central part, coexisting inside the nanoparticle of the irregular shape, are shown in Fig. 11(c) in red and green respectively.

Note that under certain conditions, the gradient of the Bernoulli function, Ψ_B , may become zero, leading to the condition $\mathbf{P} \times \mathbf{G} = 0$ in Eq. (31). In this case, referred in topological hydrodynamics as to a force-free condition, the previously discussed arguments regarding streamlines winding along the surface layers of $\Psi_B(\mathbf{r})$ do not apply any longer. However, the polarization streamlines may still conserve the toroidal or cylindrical winding. Indeed, in such a situation, the vector field \mathbf{G} becomes collinear with \mathbf{P} and can be expressed as $\mathbf{G} = \kappa\mathbf{P}$, where $\kappa = \kappa(\mathbf{r})$ is a smooth scalar function of the coordinates. Given the divergence-free nature of both fields \mathbf{P} and \mathbf{G} , we then have $\text{div } \mathbf{G} = \mathbf{P} \cdot \nabla \kappa = 0$, which indicates that \mathbf{P} is orthogonal to the vector field $\nabla \kappa$, and is, therefore, foliated by the level surfaces of the function $\kappa(\mathbf{r})$, which is now is the first integral of the polarization flow [52]. Its nonsingular surfaces must again be either a set of nested tori or cylinders, according to the Poincaré–Hopf theorem as discussed above.

When considering free forces, however, one special case should be distinguished, namely the situation where $\kappa(\mathbf{r}) = \text{const}$. Then, $\nabla \times \mathbf{G} = \kappa\mathbf{P}$. In the hydrodynamics of fluids, where $\mathbf{P} = \mathbf{v}$ and $\mathbf{G} = \rho\mathbf{v}$, this relation implies that \mathbf{P} is an eigenfield of the curl operator. However, when there is a nonlinear relationship between \mathbf{G} and \mathbf{P} , this interpretation no longer holds. Nevertheless, similarly to fluid hydrodynamics, we can conclude that in the case of free forces with $\kappa(\mathbf{r}) = \text{const}$, the vector fields exhibit flows without the formation of invariant surfaces, suggesting a more complex topology of the field. Such fields are called Beltrami fields [153–155]. An interesting example of these fields in fluids is given by the so-called ABC flow on a 3D torus, expressed as $v_x = A \sin z + C \cos y$, $v_y = B \sin x + A \cos z$, $v_z = C \sin y + B \cos x$, where A , B , and C are the parametrization constants. The streamlines of these fields exhibit chaotic behavior and draw special attention in topological hydrodynamics. Identifying the situations where a force-free condition is realized in ferroelectrics can offer intriguing possibilities for the emergence of novel topological properties.

Our further consideration of the topological states will be fully based on the results of Arnold theorem and its generalization. It is important that for our approach, neither the constraint of constancy of the polarization amplitude nor the isotropy of the polarization rotation energy, which have been the shortcomings of the real-space considerations, are essential. These effects are considered at the further stage and shown to be perturbations that do not change the topological classification of the topological states. In other words, we follow the general topological approach by determining, first, a topological class, the divergence-free polarization fields, and then selecting from those the fields

that minimize the relevant system energies: Ginzburg–Landau free energy (including anisotropic terms), gradient-related polarization energy, and elastic energy.

4.3.4. Polarization singularities

As discussed in Section 2.2, the distribution of the vector field within a confined space can give rise to singular points, either on the surface or within the volume of this space. These singularities are intrinsically connected to the topology of the manifold describing the space occupied by the system. A key constraint imposed by the divergence-free nature of the vector field is that the field fluxes entering and exiting at singular points must compensate each other. Since the polarization field vanishes at a singular point, it can be linearized in its vicinity as $P_i = J_{ij}r_j$, where J_{ij} is the Jacobi 3×3 matrix, and r_j is the local coordinates, see Section 2.2.2. The condition $\text{div } \mathbf{P} = 0$ acquires then the form $\partial_i P_i = J_{ii} = \sum_i \lambda_i = 0$, where λ_i are the eigenvalues of J_{ij} . The sum of the eigenvalues of a nondegenerate 3D matrix can only be zero if the sign of the real part of at least one eigenvalue differs from the signs of the real parts of the other eigenvalues. This occurs when the singular points are of saddle type, S_- or S_+ , but not repelling, R , or attracting, A , points. Furthermore, the Hopf–Poincaré relation (6) for closed manifolds, and the corresponding relation (7) for manifolds with boundaries, remain valid, provided that only saddle 3D points are considered.

For further specification, we consider a polarization field in a simply connected space of a nanoparticle, which is topologically equivalent to a ball D^3 . As we indicated in Section 3.2, this field should be tangential to the spherical boundary of the ball, $S^2 = \partial D^3$. According to the Hairy Ball Theorem, see Section 2.2.4, at least two singular non-degenerate points with the total 2D Hopf–Poincaré surface index equal to 2, which is the Euler characteristics of the sphere, $\chi_E = 2$, should exist at the surface of the nanoparticle. At the same time, the extension of these points into the nanoparticle volume beneath the surface S^2 provides them with the structure of the 3D singularities, which are of saddle type when occurring in ferroelectric materials. According to the generalized Hopf–Poincaré theorem (7), the arrangement of these singular saddle points at the surface predetermines the interior singularities within the particle, which should be also of the typical saddle type.

As an example, we consider a Hopfion embedded into a spherical nanoparticle D^3 , confined by the spherical boundary $S^2 = \partial D^3$, as shown in Fig. 6(d). The polarization streamlines, which wind around a series of nested tori to form the Hopfion, contain no singularities on these tori. Polarization zeros can occur only at the singular points of the Bernoulli function, located at the North (N) and South (S) poles of the sphere, marked by the yellow points in Fig. 6(d). If viewed from the surface, these singular points correspond to the stable and unstable foci, F_{out} and F_{in} , of the surface vector field, see Fig. 1(k). Both have a two-dimensional index equal to one, see Table 2; their sum corresponds to the Euler characteristic of the sphere $\chi_E = 2$. However, the 3D volume structure of these points contains both incoming and outgoing field lines. At the North pole, the polarization streamline originating from the interior terminates as it approaches zero from below, while a set of streamlines radiates outward from this zero point along the surface of the sphere. The structure of the vector field near this point is similar to that of the S_- point at the North pole of the sphere D^3 shown in Fig. 1(e), and its 3D surface index is $\text{Ind}_3(N) = -1$, as discussed in Section 2.2.4. Similarly, the 3D index of the singularity at the South pole is $\text{Ind}_3(S) = +1$. Since the total 3D index of the surface points vanishes, $\text{Ind}_3(N) + \text{Ind}_3(S) = 0$, according to the generalized Hopf–Poincaré theorem (7), the total index of the singularities inside the sphere, counted with a coefficient of 2 in Eq. (7), must also sum to zero. This implies that either no singularities exist within the ball, as in the case of a single Hopfion, or any occurring singularities must compensate each other, appearing as saddle points of types S_- and S_+ in equal numbers.

Fig. 11(c) presents a different configuration, where two Hopfions with opposite polarities coexist inside a spherical nanoparticle. In this configuration, both surface singularities at the poles are unstable foci, F_{out} , and their combined 2D surface index remains equal to two. From the perspective of 3D volume classification, both points correspond to saddle points of type S_+ , resulting in a total 3D index of +2. According to the generalized Hopf–Poincaré theorem (7), the compensating total index of singular points in the volume must be -1 . This is realized by the central saddle point of type S_- with $\text{Ind}_3(S_-) = -1$, located, as shown in Fig. 11(c), at the junction of two Hopfions.

Another example is a vortex state inside D^3 , as shown in Fig. 6(b). Although this state is not topologically stable within a manifold of 3D vector fields, see Section 2.3.5, it can still be energetically favored by interactions within the system, such as crystal anisotropy. The core singularity of the vortex is a line that begins and ends at terminal points, located either on the surface of the particle or at the boundaries of the cells separating different topological states. Fig. 8(e,f) shows the formation of small vortices (depicted in yellow) from the polar point-like singularities of the single-state Hopfion (Fig. 6(d)). The vortices push the Hopfion (shown in green) toward the interior of the nanoparticle in these regions. Notably, the length of the vortex stays restricted since it is constrained by the linearly increasing energy of the core. A similar process has been discussed in nematic liquid crystals, where a surface singularity, known as a boojum, detaches from the surface and penetrates a short distance into the sample while remaining bound to the surface by a linear singularity, the disclination [84]. More examples of vortices with endpoints and their coexistence with Hopfion states in ferroelectric nanoparticles are shown in Fig. 11(a,b). The emergence of the Bloch-like singularities at the vortex endpoints in core-shell $\text{BaTiO}_3/\text{SrTiO}_3$ nanoparticles and their manipulation by electric field was studied in [79]. The topological features of vortices with endpoints have been also extensively discussed in relation to vortices in magnetic systems and linear topological defects in superfluid ^3He [97,98]. Vortices with endpoints can be included in the general Hopf–Poincaré classification of vector field singularities if the terminal points of the vortex are merged into a single point,

Table 4

Uniform polarization \mathcal{F}_P , gradient \mathcal{F}_{grad} , elastic \mathcal{F}_{elast} , and depolarization \mathcal{F}_{dep} contributions to the total energy \mathcal{F}_{tot} , of the uniform and Hopfion states in a $\text{PbZr}_{0.6}\text{Ti}_{0.4}\text{O}_3$ nanoparticle of radius $R = 10$ nm at room temperature. The expressed in units of 10^{-18}J energies are found according to the full energy functional minimization as described in the Supplemental Material.

	\mathcal{F}_P	\mathcal{F}_{grad}	\mathcal{F}_{elast}	\mathcal{F}_{dep}	\mathcal{F}_{tot}
Uniform	−34.64	0	−4.28	4540.14	4501.22
Hopfion	−15.49	4.79	−10.22	0.011	−20.91

effectively shortening the vortex line and treating it as a unified singular point of the vector field. In a different case of a looped vortex with no endpoints, such as a doughnut-shaped vortex, see Fig. 7(b), the vortex core singularity can be easily eliminated by introducing a toroidal component of the polarization field, and thus does not contribute to the overall topological index of the system.

On a global scale, the nanoparticle's space, according to Arnold theorem, is divided into multiple cells, each containing either a Hopfion or a vortex, see Section 4.3.3. As previously indicated, the singular points of the vector field, particularly those of the Hopfion vector field, must lie on the boundaries of the cells separating the neighbor topological states, see Fig. 10(c). An especially interesting situation occurs at points where three or more cell boundaries intersect. These points are classified as either saddle points or degenerate points of the Bernoulli function, in accordance with Morse theory in differential topology [59]. These points cannot be nondegenerate maxima or minima because the nearby levels of the Bernoulli function, as stated by Arnold theorem, must form tori or cylinders, while nondegenerate extrema would imply the presence of topological spheres. At the same time, these points are also singularities of the polarization field, tangential to the level lines of the Bernoulli function. This reveals a profound topological connection between these two types of singularities, reflecting their intertwined structure in the overall topological landscape.

5. Extensions of topological hydrodynamics in ferroelectrics

5.1. Perturbative approach

In Section 4 we have provided a hydrodynamic approach for the description of topological properties of nanostructured ferroelectrics based on the selection of specific low-energy polarization states $\mathbf{P}(\mathbf{r})$ in which the strong depolarization effects, arising from the emerging bound charges $\rho = -\text{div } \mathbf{P}$, are essentially reduced. The key aspect of our approach is focusing on a subset of integrable polarization fields that satisfy the condition $\text{div } \mathbf{P} = 0$ and wind around nested tori or cylinders.

We discuss now the extent of the effectiveness of the imposed constraints. We employ the standard approach in physics exploring first the major effect, which, in our case, is the impact of the depolarization fields, and then taking into account the effects bringing in certain necessary corrections. We, thus, first find the divergence-free fields corresponding to the geometry of the problem and then consider the interplay of other energies, like polarization energy, gradient energy, and anisotropic elastic energy that define the resulting state of the system.

The material-specific functionals presented in Section 3.1 and in Supplemental Material, which account for the multi-component nature of the order parameter, are used to investigate the impact of the perturbations. We analyze the stable Hopfion topological state that emerges in a $\text{PbZr}_{0.6}\text{Ti}_{0.4}\text{O}_3$ nanoparticle with a radius of $R = 10$ nm at room temperature. In Table 4, we present the relevant contributions to the total energy, \mathcal{F}_{tot} , including the uniform polarization energy, \mathcal{F}_P , and gradient energy, \mathcal{F}_{grad} , as described by Eqs. (9),(10). Additionally, we provide the elastic energy, $\mathcal{F}_{elast} = (1/2) \int F_{elast} dV = (1/2) \int S_{ijkl} \sigma_{ij} \sigma_{kl} dV$, – here, $S_{ijkl} = C_{ijkl}^{-1}$ is the elastic compliance tensor – and the depolarization energy, \mathcal{F}_{dep} , from Eq. (16). In the same table, we also present the corresponding energy values for the unstable uniform states. As explained above, the positive depolarization energy of the uniform state exceeds by two orders of magnitude the negative polarization energy, making the uniform state highly unstable with respect to swirling to the almost divergence-free polarization texture. In the final Hopfion state, the unfavorable for ferroelectrics depolarization energy, \mathcal{F}_{dep} , almost vanishes, whereas the beneficial negative sum, $\mathcal{F}_P + \mathcal{F}_{elast}$, increases only slightly. Importantly, the positive gradient energy is concentrated in the region of the pole singularities, giving a small contribution $\sim \xi_0/R$. Nevertheless, together with the polarization energy and elastic energy, the magnitude of which is also smaller than \mathcal{F}_P , it plays the decisive role in defining which of the almost divergence-free swirled states is the most stable one.

In fact, we construct the perturbation approach with respect to the small parameter $\kappa^{-1} = \varepsilon_p T_c / 2C \simeq 10^{-2}$ or even less, in which the states with $\text{div } \mathbf{P} = 0$ correspond to the zero-order approximation. The next-order corrections will slightly modify the spatial distribution $\mathbf{P}(\mathbf{r})$, resulting, in particular, in the emergence of the small bound charges. However, such corrections will not change the overall structure of the described topological states.

Analysis of the experimental data from [209] provides a quantitative estimate of the magnitude of the depolarization effects emerging in the vortex phase realized in a $\text{PbTiO}_3/\text{SrTiO}_3$ superlattice. We compare the experimentally measured characteristic value of an internal electric field in the vortex phase, $E_i \simeq 2$ MV/cm, with the characteristic value of the depolarization field that would exist in the uniformly-polarized slab, $E_{dep} = -P_0/(\varepsilon_0 \varepsilon_b) \simeq 80$ MV/cm, where $P_0 \simeq -70$

$\mu\text{C}/\text{cm}^2$. Notably, the value of E_i is 40 times smaller than E_{dep} ; this indicates that the bound charges inducing the field E_i are smaller than the bound charges expected for the uniformly polarized ferroelectric over approximately the same factor. Unfortunately, experimentally available data do not enable access to the bound charges, in particular, to the surface bound charges related to the normal polarization component. Notably, the piezoresponse force microscopy (PFM) measures the average values within the finite penetration depth-thick, about 30nm [210], layer, which is larger than the characteristic coherence length ξ_0 , constituting several nanometers. From the instrumental perspective, it is important to have the possibility of extracting these data from direct measurements.

Another factor that perturbs the polarization streamlines of the divergence-free polarization field is the electric charges, which are either externally introduced into the system or inherent to the considered ferroelectric material. The emergence of volume and surface charges, either of intrinsic, external, or electrode-induced origin, breaks down the condition for the field to be divergence-free. However, in realistic systems where the charge concentration is not extensively high, this breakdown only slightly changes the texture of the polarization field, and is, hence, a perturbation.

In this Section, we explore the stability of polarization topological states under various perturbations, including crystal lattice anisotropy and electrostatic forces, based on the fundamental theorem of Kolmogorov, Arnold, and Moser. This theorem, applicable to integrable systems and commonly referred to as the KAM theorem, underpins our analysis. It helps to explain why the orbits of planets in the Solar System remain stable over billions of years despite strong and complex gravitational interactions between them. According to the KAM theorem, in ferroelectrics, small disturbances do not affect the topological tori winding states but can lead to reconfiguration of polarization streamlines.

5.2. Ergodicity, anisotropy, and the KAM theorem

In Section 4.2.1 we demonstrated that in small nanoparticles, the polarization streamlines form highly structured patterns by winding around nested tori or cylinders. The line localization is a notable outcome of the properties of integrable dynamical equations, specifically Euler-type equations that describe the mechanical stability of polarization streamlines, see Section 4.1.3. Such type of integrability results in very broad implications in physics, including the construction of devices like tokamaks and stellarators that explore this toroidal arrangement of magnetic fields and phenomena of celestial mechanics [211,212]. The property of localization of a streamline in the specific part of the space, often referred to as non-ergodicity, presents significant interest in studying stochastic systems.

Ergodicity, in its most general sense, describes the ability of a physical system to explore all possible states over time, ensuring the equivalence of time and statistical averages. This principle is widely applied in statistical physics to describe the dynamics of thermodynamic systems and phase transitions. In the context of streamlines of the vector field [52], ergodicity takes on specific characteristics. While the concept of the stable distribution of field lines typically refers to their tendency to settle into energy-minimizing spatial configurations, ergodicity introduces a temporal aspect, in a sense of the time-like streamline parametrization introduced in Section 4.1.1, which suggests that streamlines can transition through various configurations, exploring all possible points at the system manifold. Streamline ergodicity, though not yet widely applied in ferroelectrics, plays a crucial role in understanding non-uniform polarization states in ferroelectrics, including complex topological structures. It offers insights into how these states transition under external fields and helps explain the dynamic behavior of systems such as relaxors [213,214], where polarization fluctuations and chaotic states are prominent. Thermodynamics and topological transitions in ferroelectrics are closely tied to ergodicity. The phase transition between different non-ergodic topological states can proceed either smoothly through the formation of intermediate ergodic configurations or abruptly, involving a complete reconstruction of the host cells, as demonstrated, for example, in Fig. 11(a,b).

The non-ergodicity of field lines in a closed space means that the field lines do not pass through all accessible regions of the space uniformly. Instead, they may concentrate in certain regions, winding, for instance, quasi-periodically around the invariant tori, retrace the same paths, and fail to entirely cover certain parts of the space. Furthermore, it appears that even under perturbations, many of the quasi-periodic winding trajectories do persist, implying that the system still retains a certain degree of regularity and non-ergodicity. This property has been mathematically formulated and proved by Kolmogorov, Arnold, and Moser and is known as the KAM theorem [215,216]. The KAM theorem asserts that in a fully integrable system, regular, quasi-periodic trajectories wind on the set of invariant tori. When small perturbations are applied to such a system, most of these invariant tori remain intact, preserving the regular quasi-periodic structure of trajectories. Only significant perturbation can break out the tori winding. Applying a version of the KAM theory adapted for the divergence-free vector fields [52,159–161] to ferroelectrics, one explains how the observed periodic invariant tori structure of polarization persists under divergence-free perturbations, even in the case of a small diffusion of numerical viscosity of the system. When these perturbations become significant, the invariant tori winding may break down.

The emergence of crystal anisotropy causes an essential perturbation in ferroelectrics. As we discussed in Section 4.1.3, the full account of the anisotropic terms in the elastic stability conditions (23) may disturb its Euler structure, hence integrability. However, at a numerical level, we do not observe a significant anisotropic perturbation of the streamline tori-winding foliation in small, 50–60 nm size, nanoparticles, as shown in Fig. 8, which indicates that anisotropic perturbations are too weak to destroy the invariant tori in nanosized systems. At the same time, the anisotropy-caused breakdown of the regular tori winding is clearly seen in bigger particles of radius $R = 100$ nm, see Fig. 12. The side-view of the nanoparticle shows now the more irregular texture of polarization streamlines, see Fig. 12(a), with a proliferation of surface singular

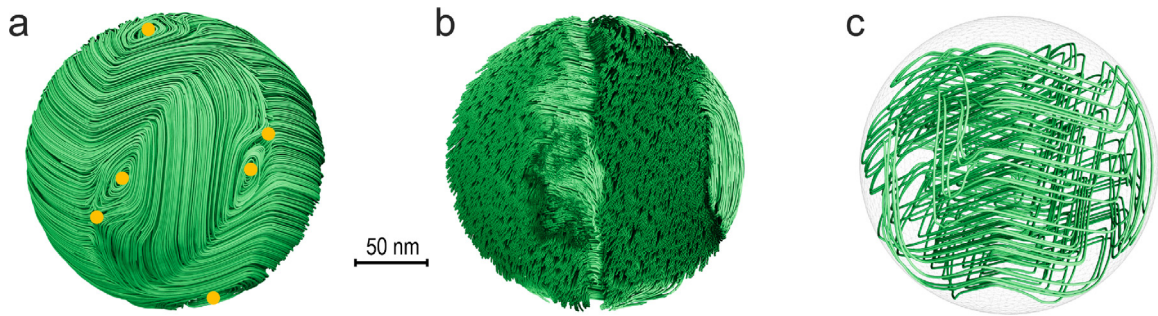


Fig. 12. Ergodicity of streamlines in a big PZT nanoparticle. Numerical simulations. (a) Side-view of the irregular pattern of the streamlines. Surface singular points are shown in yellow. (b) Poincaré map of streamlines at the vertical cross-cut of the nanoparticle. (c) One single streamline passes through the entire volume of the nanoparticle.

points, shown in yellow. The toroidal winding pattern completely disappears from the cross-cut Poincaré map, Fig. 12(b). Furthermore, tracing only one streamline reveals that it displays a rather chaotic behavior, see Fig. 12(c). The line tends to pass through all regions accessible for the nanoparticle without favoring any specific part. We conclude here with the observation that as the size of the particle increases, the anisotropy influence becomes significant, leading to the destruction of the invariant tori, predicted by the KAM theorem. In particular, the anisotropy causes the field lines to deflect in one direction and then encounter anisotropy of another orientation. This can lead to a uniform distribution of lines across the entire space and indicates the possible ergodicity of the system. Further, in Section 5.3.1, we provide more examples of the destruction of regular tori by the introduction of electrical charges into the system.

5.3. Electric charges in ferroelectrics

5.3.1. Residual bound charges

As we previously discussed in Section 4.2.3, the geometry of a nanoparticle can disrupt the ideal divergence-free nature of the polarization distribution. This disruption leads to the formation of residual bound charges and the corresponding depolarization field. Fig. 8(h) illustrates the residual electric field and charge distribution within a cubic ferroelectric nanoparticle, arising due to the geometry-induced perturbations of the polarization field. In Fig. 8(h), the red and blue regions represent the volume and surface charges within and on the nanoparticle, respectively. The red regions correspond to positive charges, while the blue regions indicate negative charges. These charges generate the residual depolarization fields, which are illustrated by the green streamlines in Fig. 8(h). It is noteworthy that the densities of the emergent volume and surface charges, with typical values of $\rho \simeq 10^7 \text{ C m}^{-3}$ and $\sigma \simeq 10^{-2} \text{ C m}^{-2}$, as well as the typical values of the depolarization fields, $E_{\text{dep}} \simeq 2 \times 10^2 \text{ kV cm}^{-1}$, are approximately two orders of magnitude smaller than what would be expected if the polarization exhibited a unscreened divergence.

In the case of strong anisotropy in the sample, whether of natural or strain-induced origin, substantial bound charges can be restored, manifesting as either head-to-head or tail-to-tail charged domain walls [11], distributed depolarization charges in soft Kittel domains [140], or polar topological defects [217], particularly when the anisotropic energy becomes comparable to the screened electrostatic energy. The situation may change even more in an atomically thin ferroelectric layer. As the thickness of the ferroelectric layer becomes smaller than the coherence length, the creation of a non-uniform texture requires considerable gradient energy. Essentially, the sizes of the vortex domains may not fit within the ferroelectric film thickness. In such cases, a monodomain state can become more favorable, especially if the depolarization field is further screened by conducting electrodes [218]. A similar transition from a multidomain to a monodomain state has been predicted for ferroelectric/dielectric superlattices with an atomically small period [219]. Notably, due to image forces, the electrostatics of a ferroelectric film confined between two non-perfect electrodes is equivalent to that of a periodically repeating heterostructure.

5.3.2. Intrinsic free charges

Next, we describe the effects of electric screening caused by the presence of semiconducting or impurity-induced free charges within ferroelectric materials. The concentration of these free charges is quantified by the Debye–Huckel or Thomas–Fermi screening length, δ , see Eq. (15). For typical charge concentrations ranging from 10^{18} to 10^{14} cm^{-3} , the screening length δ typically varies between 5 to 20 nm. In nanostructured ferroelectrics, this range is insufficient to fully screen the depolarization fields or destroy the topological states. However, at higher concentrations of free charges, the topological states may be disrupted, leading to the untwining of polarization streamlines into a uniformly polarized state.

Panels (a)–(d) in Fig. 13 illustrate the impact of intrinsic free charges on the Hopfion topological state confined within a PZT nanoparticle with a radius of $R = 25 \text{ nm}$. For typical PZT materials, where the screening length is approximately $\delta = 80\text{--}100 \text{ nm}$ [220,221], the screening has a minimal impact on the Hopfion texture. However, at a higher density of free

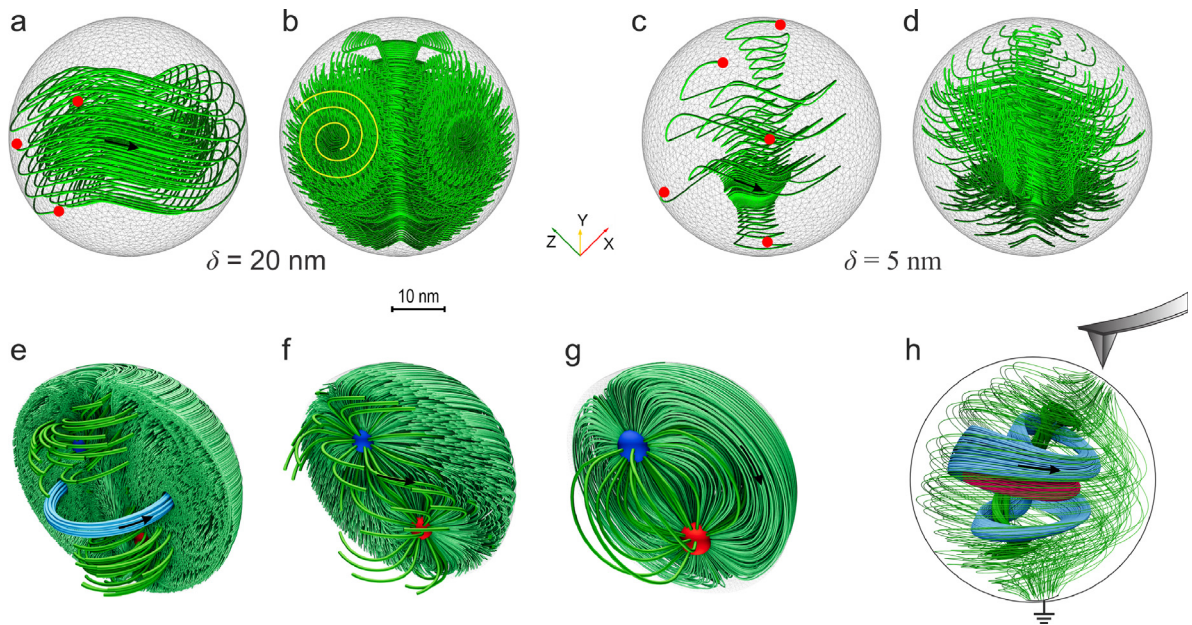


Fig. 13. Effect of electrical charges on topological states in a ferroelectric PZT nanoparticle. Numerical simulations. (a) Slight distortion of the tori texture caused by moderate screening with screening length $\delta = 20$ nm. The red points depict the spots where polarization lines thrust the surface of the nanoparticle. (b) Poincaré cross-section of the nanoparticle demonstrating the details of the tori distortion at $\delta = 20$ nm. The concentric nested tori sections transform into the snail-like convolving configuration, visualized by the yellow spiral line. The polarization lines creep from torus to torus. (c) Breakdown of the toroidal structure at stronger screening with $\delta = 5$ nm. (d) Poincaré cross-section of the nanoparticle at $\delta = 20$ nm demonstrating the tearing of the torus and formation of the helicoidal structure. (e) Emergence of the positive and negative localized electric charges $Q_0 = \pm 1.7 \times 10^{-17}$ C, shown by small red and blue spheres, perturbs and starts to disturb the tori winding of the streamlines, while certain toroidal configurations are still conserved; the exemplary torus is shown in blue. (f) Increasing the localized charges to $4.5Q_0$ destroy the tori winding. The polarization lines are still swirled, forming the helical structure. (g) Stronger localized charges with magnitude $16Q_0$ polarize the nanoparticle, forming the dipolar pattern of streamlines. (h) Application of the PFM tip to the nanoparticle surface creates the mixed structure of the helical polarization flux and polarization lines winding around the linked tori, shown in blue and red.

charges, reducing the screening length to around $\delta \simeq 20$ nm, the polarization lines still maintain their winding texture, although the volume and surface charges begin to disrupt the condition for the field to be divergence-free. This disruption allows the polarization lines to thrust through the nanoparticle's surface, causing a slight distortion of the fibered nested tori structure, according to the KAM theorem. The polarization lines may then convolve or untwine along spiral-like paths, transitioning from torus to torus and forming a snail-like Poincaré map, as shown in Fig. 13(a,b).

As the density of free charges increases further, resulting in a screening length of $\delta \lesssim 5$ nm, Hopfions become increasingly disrupted, and helicoidal textures begin to emerge within the nanoparticle. Achieving a complete unwinding of the polarization lines into a monodomain structure requires an extremely high concentration of free carriers, comparable to their concentration in a good metal, where $\delta < 0.05$ nm, see Fig. 13(c,d).

5.3.3. Localized remanent charges

Another important issue is the emergence of localized charges due to impurities, ion vacancies, or surface-reconstruction defects. These impurities can also serve as sources of free charges. Recent work [164] has identified several factors that contribute to the presence of remnant-bound charges at interfaces or within the material's interior. These factors include (i) epitaxial strains, which can induce stress in the material, leading to the alignment of dipoles in specific orientations; (ii) the interplay of different structural phases, which can affect the arrangement of charges and dipoles, contributing to the persistence of remnant-bound charges; (iii) the chemical composition of ferroelectric materials, such as PbTiO_3 or Ti-rich PZT solid solutions, which favors the tetragonal orientation of dipoles; and (iv) partial screening of bound charges or the influence of a symmetry-breaking electric field (e.g., built-in bias), which can promote Ising-like symmetry, where dipoles are constrained to point “up” or “down”, hindering the complete rotation of interfacial dipoles.

To minimize electrostatic energy, polarization dipoles tend to align in ways that counterbalance the electric fields generated by these charges. This alignment naturally introduces sources and sinks into the consideration of the divergence-free polarization field. While a small concentration of localized charges may not significantly disrupt the long-range polarization topological states, a high concentration of such charges has the potential to destabilize this ordering and significantly alter the topological landscape.

Fig. 13(e–g) demonstrates how the tori winding topological structure of polarization streamlines inside of a spherical PZT nanoparticle evolves and breaks down upon the emergence of the localized remanent charges. The testing positive and

negative charges, depicted as red and blue spheres respectively, are introduced into the system, and their value decreases from panel (e) to panel (g). These charges influence the polarization vector field, leading to changes in the structure and intensity of the field lines. When the value of the charges is not too large, as shown in Fig. 13(e), only a portion of the tori is disrupted. The constituent lines that form the tori are torn apart, with their ends being drawn toward the charges. These lines now begin at the positive charge and terminate at the negative charge, thus forming bound charges at their endpoints that effectively screen the remaining localized charges. Another part of the winded tori, for instance, the torus shown in blue, is not broken but is only slightly distorted, indicating the system's robustness at this configuration, in accordance with the KAM theorem.

As the charge magnitude increases, as shown in Fig. 13(f), the charges destroy the tori winding and cause the lines to be more tightly packed at the charged endpoints. The formed by $\text{div}\mathbf{P}$ bound charges are more effective in screening the remanent localized charges, leading to a more complex and tightly-knit swirled polarization field structure around the charges. Fig. 13(g) shows that the further increase of the magnitude of the introduced charges results in a profound reconstruction of the polarization vector field. The nanoparticle becomes fully polarized by the introduced local charges and the polarization streamlines align to form a dipolar-like pattern.

A key new circumstance is that the polarization field, $\mathbf{P}(\mathbf{r})$, contains not only a divergence-free part but also a charge-related divergent, curl-free component, enabling Helmholtz–Hopf decomposition as described in Section 2.1.3. This divergent component is characterized by streamlines that originate from negative charges and terminate at positive charges. Consequently, in addition to the non-divergent saddle singular points of types S_+ and S_- , as indicated in Table 3, the singular points of repelling, R , and attractive, A , type, corresponding to negative and positive bound charges, emerge in the divergent component of polarization. These surface-located and volume-located singularities correspond to the respective surface charges, see Fig. 13(e–g), and volume charges, see Fig. 13(a,c). Importantly, the indices of all singular points in the system remain connected by the generalized Poincaré–Hopf theorem (7).

5.3.4. Screening electrodes

While it might seem that the screening of the emergent depolarization field by short-circuited electrodes would destroy non-uniform polarization states, a more realistic scenario, where electrode-induced screening is imperfect, reveals that topological states can persist even in systems with highly conductive electrodes. The study [10] demonstrated that partial screening by electrodes, quantified by an effective screening parameter β , allows topological states to exist near $\beta \simeq 90\%$, with complete screening characterized by $\beta = 100\%$. Furthermore, the structure of the emerging topological states can be tuned by varying the screening parameter β .

The impact of surface-deposited electrodes on the periodic vortex-domain structure in compressively strained ferroelectric films was also explored in [222]. It was shown that for non-ideal electrode materials, the emergence of a monodomain state is unlikely. The realistic metallic properties of electrodes are typically characterized by the Thomas–Fermi screening length δ . Energetic considerations presented in [222] demonstrate that even for very small values of δ on the order of an Ångström, which is typical for good metals, the domain structure remains stable. In addition, it may also be stabilized by imperfections at the electrode–ferroelectric junction, which is typically sandwiched by a dielectric atomically-thin dead layer present in real systems. Similarly, feasible semiconducting charges within ferroelectric materials are generally insufficient to fully screen the depolarization fields and do not significantly alter the periodic polarization vortices.

Notably, the interaction of charges within a few-nanometer-thick dielectric or ferroelectric film sandwiched between two metallic or semiconducting electrodes is governed by quasi-2D electrostatics. Specifically, the 3D Coulomb electrostatic potential, which decays as $\varphi_{3D} \propto 1/r$, evolves into a logarithmic potential $\varphi_{2D} \propto \ln(r/\Lambda)$ for $r < \Lambda$, transitioning to an exponentially-decaying potential $\varphi_{2D} \propto \exp(-r/\Lambda)$ for $r > \Lambda$, where the screening length Λ is determined by the material properties and system geometry [223].

Recent simulations have demonstrated the potential for the existence of Bloch-type skyrmions, which produce substantial bound charges, $\simeq 0.6e/\text{uc}$, in ultra-thin films of $\text{PbZr}_{0.4}\text{Ti}_{0.6}\text{O}_3$ with approximately $\beta = 90\%$ screening of polarization-induced surface charges, similar to the effect of electrodes [82]. Furthermore, residual bound charges, albeit of lesser magnitude, $\simeq 0.45e/\text{uc}$, have been observed in simulations of a ferroelectric PbTiO_3 layer sandwiched between realistic electrodes with $\beta = 80\%$ screening, as well as in $\text{PbTiO}_3/\text{SrTiO}_3$ multilayers [217]. These charges were associated with the vector field of topologically protected states, dipolar waves, and disclination patterns. All these systems with partial screening are of significant interest as they offer the potential to observe a crossover from topological hydrodynamics to a topological vector field approach by varying the screening parameters.

Utilizing external biased electrodes offers a powerful method for the efficient manipulation of topological states within ferroelectric nanostructures. Fig. 13(h) demonstrates the result of the application of a 10 V bias, using, say, the aside PFM tip, to a spherical PZT nanoparticle, while the bottom point of the nanoparticle is grounded. These two localized electrodes create small surface regions on the nanoparticle where the polarization streamlines can enter and exit. The presence of surface sources and sinks of polarization, as depicted in Fig. 13(h), generates a helical arrangement of polarization streamlines that carry the polarization flux between these singular points. Yet, despite the disturbance caused by the electrodes, the Hopfion topological states remain partially preserved. Two toroidal structures, depicted in blue and red in Fig. 13(h), not only survive but also become entangled due to the interlinking of the streamlines.

5.4. About terminology

Discovery of the topological structures in ferroelectrics, like any great discovery in science, follows an internal logic of epistemology. Unequivocally, we are now passing the period of the observation and obtaining the empirical evidence of a multitude of topological formations, sometimes looking as objects having essentially different characteristics and aspects. While an initial empirical taxonomy is helpful in identifying the objects, it has certain limitations complicating further research progress. Usually, limitations are based on the subjective characteristics of the appearance of the objects and, sometimes, on the straightforward transferring of concepts from the other branches of knowledge. The intrinsic subjectivity of such a transferring may lead to the multiplication of the terminological entities without the proper necessity¹ and to attribute to the objects the properties that they do not necessarily possess. For instance, as we described in Section 3.3, the formal transposition of skyrmion terminology from magnetism to ferroelectricity immediately raises questions about the electrostatic stability of ferroelectric skyrmions (a concern less relevant in magnetism), about whether their topological description via the homotopy groups formalism is similar (actually not), and about the intrinsic mechanisms of their formation (which would replace the Dzyaloshinskii–Moriya interaction mechanisms in magnetism).

The subjectivity in the appellation “by similarity” results in a seeming richness of the taxonomy, causing, however, difficulties in understanding. For instance, the same vortex state with the circular vortex axis entwining into a ring appears under a multitude of names brought by different authors. Namely, it is called central domain, bubble domain, electrical skyrmion bubble, skyrmion bubble, polar bubble skyrmion, polar skyrmion bubble [164], toron, [165] etc. In our description of topological states in ferroelectrics, we prefer to use the approach of the hydrodynamic topology. The topological classification, which is indeed more concise than a broad spectrum of the suggested empirical names, is a rigorous approach, based on the mathematical theorems that we provide in Section 4.3.3, within the limits of its applicability (Section 5). Namely, this approach allows us to consider all examples of the polarization distribution in confined ferroelectrics from a unique topological viewpoint. Furthermore, the calculated vector fields in ferroelectric nanoparticles and nanodots (Section 7.2), as well as the reconstruction of the experimentally obtained polarization vector fields of vortex stripe domains and vortex bubbles (Section 7.4), show that most probably they do have the Hopfion-like or vortex-like configurations.

6. Quantification of topological states

6.1. Numerical indicators

Characterizing the topological states in confined ferroelectrics necessitates numerical indicators that enable the quantification of properties such as the degree of emergent polarization swirling and chirality within the system. The swirling of polarization can be characterized locally by the vorticity of the field, ω , and globally by the parameter Ω , which represents the integral of the vorticity over the entire volume V of the coordinate manifold space \mathcal{M} of the system. These parameters are expressed as follows [162]:

$$\Omega = \int_{\mathcal{M}} \omega dV, \quad \omega = \nabla \times \mathbf{P}. \quad (33)$$

Nonzero Ω indicates the presence of vortices. Note that we apply the hydrodynamic terminology for vorticity ω [152], while in magnetism, vorticity refers to the winding number N_1 [102], see Section 2.3.2.

Notably, the sign of the vorticity does not necessarily reflect the direction of the rotation, clockwise (CW), or counterclockwise (CCW). To illustrate this, let us consider a polarization vortex confined in a cylinder of radius R and length L with an exemplary radial dependence of the polarization $\mathbf{P}(\rho) = P(\rho)\mathbf{e}_\varphi$ in cylindrical coordinates ρ and φ . The ferroelectric cylinder is surrounded by the dielectric material with zero spontaneous polarization, resulting in the suppression of the polarization amplitude in the vicinity of the cylinder surface, and hence in the non-monotonous behavior of $P(\rho)$ through the whole vortex. Then, the radial distribution of the vortex polarization in the near-surface region, $\mathbf{P}(\rho) \simeq (P(R) + C_1(R - \rho))\mathbf{e}_\varphi$, provides the vorticity $\omega = -C_1\mathbf{e}_z$ with the sign opposite to that realized in the vortex core, where $\mathbf{P}(\rho) \simeq C_0\rho\mathbf{e}_\varphi$ and $\omega = C_0\mathbf{e}_z$. Here, the magnitude of the vortex polarization at the surface, $P(R)$, and numerical coefficients, C_0 and C_1 , are either all positive, in the case of the CCW vortices, or all negative, in the case of the CW vortices. As an example, the decrease of the order parameter far from the vortex core can be facilitated by the elastic coupling of the polarization with crystal lattice [41].

In general, the swirling parameter of the whole system, Ω , is equal to zero. According to the Stokes theorem, Eq. (33) transforms to polarization circulation around a remote circular contour C , encircling the cylinder and lying far away in the dielectric region, $\Omega = \mathbf{e}_z L \oint_C \mathbf{P} d\mathbf{l}$, which vanishes because of the suppression of the polarization in the external dielectric media. Here, $d\mathbf{l}$ is the differential length along C . The equality to zero of the swirling parameter implies that within the vortex area, having the definite direction of the polarization rotation, CW or CCW, the sign of the vorticity is

¹ The maxim “*Entia non sunt multiplicanda praeter necessitatem*”, which serves as the cornerstone of modern research methodology, is attributed to the 14th-century friar William of Ockham. However, the origins of this statement are more ambiguous [224].

not homogeneously defined. Namely, the vorticity of the vortex core region is compensated by the vorticity of the outer region, having the opposite sign.

The vortex structure can also be characterized by the toroidal, \mathbf{T} , and hypertoroidal, \mathbf{G} , moments [225], that we define as the integrals of the corresponding toroidal, \mathfrak{T} , and hypertoroidal, \mathfrak{G} , moment densities

$$\mathbf{T} = \int_{\mathcal{M}} \mathfrak{T} dV, \quad \mathfrak{T} = \frac{1}{2} \mathbf{r} \times (\mathbf{P} - \bar{\mathbf{P}}), \quad (34)$$

$$\mathbf{G} = \int_{\mathcal{M}} \mathfrak{G} dV, \quad \mathfrak{G} = \frac{1}{4} \mathbf{r} \times (\mathbf{r} \times (\mathbf{P} - \bar{\mathbf{P}})). \quad (35)$$

To reflect the absence of the depolarization field in the confined system, we have to put the condition $\bar{\mathbf{P}} = 0$ for the average polarization. Unlike the swirling parameter Ω , the signs of toroidal and hypertoroidal moments discriminate between CW and CCW rotation of the polarization vector.

Note, however, that none of the described indicators can be used for the detection of the handedness of the system since the mirror images of the corresponding expressions can be overlaid onto the originals after the proper turn. In principle, the handedness of topological states can be quantified by the chirality, X , as an integral of the corresponding chirality density,

$$X = \int_{\mathcal{M}} \chi dV, \quad \chi = \mathbf{P} \cdot (\nabla \times \mathbf{P}). \quad (36)$$

The introduced scalar indicator, chirality, has, however, the same shortcoming as vorticity Ω . While being capable of detecting the presence of the chirality itself, it cannot unambiguously determine the sign of the handedness because the differential vorticity density $\nabla \times \mathbf{P}$ does not univocally determine the direction of rotation of the polarization vector. Let us consider, for instance, a right-handed helicoidal structure formed by the bounded CCW vortex, nucleating within the uniformly polarized state, $\mathbf{P} = P_z \mathbf{e}_z + P(\rho) \mathbf{e}_\varphi$, where the uniform z -directed component of polarization, $P_z = \text{const}$ and the perpendicular vortex component, $P(\rho)$, vanishes at the vortex core and also at the infinity, as we described above. The total chirality can be calculated using again the Stokes theorem, $X = LP_z \oint_C \mathbf{P} d\mathbf{l}$. Then, similar to the swirling parameter, the total chirality vanishes for the remote enough contour C , not allowing to determine the handedness of the system.

6.2. Topological charges

Other types of parameters quantifying the properties of the topological states are the so-called topological charges or topological indices, characterized by their invariance with respect to small continuous deformation of the system, in particular with respect to the volume-preserving diffeomorphisms, keeping the divergence-free character of the vector fields.

It is of fundamental importance in ferroelectrics to utilize another characteristic value, the vector potential \mathbf{A} of the divergence-free polarization vector field, introduced in Section 4.2.2. Defining \mathbf{A} in an analogy with electromagnetism, via $\mathbf{P} = \nabla \times \mathbf{A}$, we straightforwardly obtain $\text{div } \mathbf{P} = 0$. Note that in a particular case of the uniform distribution of polarization, the vector potential can be presented as $\mathbf{A} = (1/2)[\mathbf{r} \times \mathbf{P}]$ that coincides with the density of the toroidal moment, Eq. (34). For the axisymmetric Hopfion, described by Eqs. (25), (26) the vector potential is

$$\mathbf{A} = \alpha_t \xi \mathbf{e}_r + \alpha_p \zeta \mathbf{e}_\varphi, \quad (37)$$

where the function ξ is calculated from $\eta = -r^{-1} \partial \xi / \partial \theta$, and for the particular choice of η and ζ (26) is given by

$$\xi = r \sin\left(\frac{\pi r}{2R}\right) \cos \theta. \quad (38)$$

The use of the vector potential \mathbf{A} allows for the introduction of another topological characteristic, helicity \mathcal{H} , determined by Eq. (27) in Section 4.2.2. This topological characteristic, emerging also in topological hydrodynamics and electromagnetism, changes sign when transitioning from a left-handed to a right-handed coordinate system. Consequently, like chirality, X , specifies the handedness of the system. In the particular case of the axisymmetric Hopfion (25), the calculation of helicity is simplified to [226]

$$\mathcal{H} = 2 \alpha_p \alpha_t \int_{\mathcal{M}} \zeta \eta dV. \quad (39)$$

In Section 4.3.2, a deep internal connection between the system's helicity and the linking number of the streamlines, \bar{L}_P , was described. Identifying the linking number from experimental data or simulation results appears to be a promising approach. Furthermore, measurements of \bar{L}_P in simulation experiments could be technically simpler than measuring \mathcal{H} . This parameter may serve as an independent numerical characteristic of the system's complexity, manifesting even in cases where charges or electrodes disrupt the internal topological states of the system, see Section 5.3.1.

Recall that, as previously noted in Section 4.2.2, in this Review, we adhere to the hydrodynamic definition of helicity, as defined by equation (27), that differs from the helicity in magnetism. However, even in hydrodynamics, sometimes another definition of helicity, coinciding with the introduced in Eq. (36) chirality parameter, is used for characterization

Table 5

Parameters quantifying the swirling and handedness of the model Hopfion.

Swirling parameter	$\Omega = 8.38 \alpha_t R^2 \mathbf{e}_z$
Toroidal moment	$\mathbf{T} = 0.96 \alpha_t R^4 \mathbf{e}_z$
Hypertoroidal moment	$\mathbf{G} = 1.19 \alpha_p R^5 \mathbf{e}_z$
Chirality	$X = 43.72 \alpha_p \alpha_t R^2$
Helicity	$\mathcal{H} = 4.09 \alpha_p \alpha_t R^4$

of the handedness of ferroelectric topological states, see, e.g., [227]. An ambiguity in the definition of \mathcal{H} appears due to the existence of two different approaches in hydrodynamics. In one approach, the velocity field of the liquid, $\mathbf{v}(r)$, is used as a principal vector field, characterizing the system. Then, the helicity, defined as $\mathcal{H} = \int_{\mathcal{M}} \mathbf{v} \cdot \mathbf{A} dV$, where the vector potential \mathbf{A} , coming from the relation $\mathbf{v} = \nabla \times \mathbf{A}$, characterizes the average linking number of the streamlines of the field $\mathbf{v}(r)$ [52]. In another approach, it is the vorticity field, $\boldsymbol{\omega} = \nabla \times \mathbf{v}$, that is considered as a principal vector field. The corresponding helicity, defined as $\mathcal{H} = \int_{\mathcal{M}} \boldsymbol{\omega} \cdot \mathbf{v} dV$, characterizes the average linking number of the vortex tubes, formed by the streamlines of the field $\boldsymbol{\omega}(r)$ [162]. We follow the first approach taking into account that this is the polarization vector field $\mathbf{P}(r)$ in ferroelectricity which is an analog of the divergence-free velocity field $\mathbf{v}(r)$ in hydrodynamics. Then, the helicity defined by Eq. (27) provides a distinct topological characterization of the handedness and the linking number of the streamlines of the field $\mathbf{P}(r)$. Another definition of helicity operates with the streamlines of the vorticity field $\boldsymbol{\omega} = \nabla \times \mathbf{P}$ which do not have a clear physical meaning and, hence, cannot be used for judging about the total handedness of the system, as we have already discussed above.

Although, as discussed in Section 3.3, the coordinate space of nanostructured ferroelectrics is a 3D space, certain polarization textures – such as vortex-like, skyrmion-like, or meron-like structures – can, to some extent, be qualitatively characterized using the real-space winding numbers, described in Section 2.3, typically applied in magnetism to states, confined in 2D spaces. In particular, the vortex winding number, N_1 , see Section 2.3.2, can be used to describe the swirling of the polarization vector within the system. For coreless topological states, such as skyrmion- or meron-like tubes displayed in Fig. 3, the appropriate winding number is the Pontryagin index N_2 , see Section 2.3.3. It was successfully used in [17] to test the behavior of the vector field in the cross-sectional areas of the chiral bubbles, called polar skyrmions. However, unlike 2D magnetic skyrmions, N_2 may take arbitrary values when the direction of \mathbf{P} at the tube's periphery is not fixed.

6.3. Application of quantification parameters

The parameters represented above well describe the variance of the properties of the polarization field in nanostructured systems and are widely used to treat the experimental and simulation data. Yet, for the most efficient use of these parameters, one has to set up their respective areas and conditions of applicability. To illustrate this, we consider the model Hopfion, in which the distributions of polarization and vector potential are given by Eqs. (25), (26), and (37), (38) respectively. The quantitative parameters are calculated using the corresponding Eqs. (33)–(36), and (27). The results are given in Table 5.

As follows from Table 5, the swirling parameter and toroidal moment are sensitive to the toroidal component of the Hopfion, i.e., they are effective for straight vortices where $\alpha_p = 0$, $\alpha_t \neq 0$ and vanish for the doughnut vortices where $\alpha_p \neq 0$, $\alpha_t = 0$. The hypertoroidal moment, in contrast, is sensitive to the poloidal component, hence to the emergence of doughnut vortices. Note that neither toroidal nor hypertoroidal moments can be used to discriminate between the chiral and achiral states since they remain non-zero in the states with no handedness, straight vortices and doughnut vortices, respectively. The handedness is characterized by the chirality and helicity parameters that are both non-zero in the chiral state, where both α_t , $\alpha_p \neq 0$, and vanish in the achiral state of the straight or doughnut vortex where one of the components, α_t or α_p , is equal to zero. Note, however, that although the indicated parameters can be used for the characterization of particular properties of the polarization distribution, their full relevance realizes when one does associate the measurable physical parameter with them. For instance, having similar integral expressions in Table 5, the chirality and helicity may be very different in terms of the distribution of their densities over the sample volume. Which precisely parameter becomes most significant depends on the concrete realization of the experiment that reveals handedness, for instance, on the type of the chiral fields testing the handedness [228].

7. From theory and simulations to experiment

7.1. Topology of nanostructured ferroelectrics

This Section focuses on the manifestation of topological states in specific ferroelectric nanostructures, using selected materials and configurations to bring the conceptual understanding of the topology in ferroelectrics to life. We explore how these states arise in confined geometries such as nanoparticles, nanorods, thin films, heterostructures, and certain bulk systems. A key objective is to investigate how shape and geometry influence the formation of topological states,

with particular emphasis on the distinct characteristics associated with topological connectivity of the system coordinate manifolds, see Section 2.1. We demonstrate that, unlike the simply connected spaces of nanoparticles, multi-connected topologies – typically realized in nanorods and heterostructures – introduce additional complexity in the behavior of polarization fields, significantly affecting the stability and transitions in these topological states.

We begin by examining ferroelectric nanoparticles and nanodots, where confinement leads to the emergence of vortex and Hopfion states. We then move to nanorods, where the combination of axial symmetry and multi-connected space results in more complex topological configurations. The discussion continues with topological states in thin films and heterostructures, highlighting the influence of periodic boundary conditions and multi-connectivity on the emergence of topological states. Finally, we address bulk systems and composites, where the distribution of the polarization flux throughout the volume leads to even more intricate topological states.

In this Section, we do not aim at providing a comprehensive review of experimental and modeled materials or the exhausting covering of the rapidly developing field of ferroelectric nanostructures. We illustrate fundamental topological phenomena in ferroelectrics, described in previous Sections, using selected experimental materials as examples. For readers seeking a detailed description of the experimental state-of-the-art, we highly recommend the nice reviews mentioned in the Introduction, Section 1.

7.2. Nanoparticles and nanodots

7.2.1. Simply connected nanostructures

Ferroelectric free-standing nanoparticles and substrate-deposited nanodots were among the first systems that were utilized to investigate polarization behavior in confined geometries. The term nanoparticles is generally used to refer to small particles with various shapes, typically ranging in size from 1 to 100 nm, and can be free-standing or embedded in a matrix. The term nanodots is usually employed to describe the specifically disk-shaped or dot-like nanostructures that are typically deposited on a substrate. All these nanoparticle-based systems are described by simply connected coordinate manifolds, which ensures reliable ways to analyze and understand their topological structures building on the topological approaches outlined in Sections 4 and 5. These systems offer a rich platform for studying the emergence of topological states, characterized by the non-uniform distribution of the polarization field.

7.2.2. Nanoparticles

An efficient exploration of topological states in ferroelectric nanoparticles has begun with simulations that demonstrated the existence of vortex states in disk-shaped nanoparticles of $\text{PbZr}_{0.5}\text{Ti}_{0.5}\text{O}_3$ [37], see Fig. 14(a). This finding marked a significant step forward, although early experimental observations of size effects on thermodynamic properties of ferroelectric nanoparticles were initially interpreted in terms of a uniform state [229–231]. Subsequent developments in simulation works revealed the inherently inhomogeneous vortex states in cubic nanoparticles of $\text{PbZr}_{0.4}\text{Ti}_{0.6}\text{O}_3$ [33], spherical nanoparticles of PbTiO_3 and BaTiO_3 [30,79], cylindrical nanoparticles of PbTiO_3 [32,41], and vortex domain states in ferroelectric nanodiscs of TGS and PbTiO_3 [32,34]. The topological states with doughnut vortex configurations of polarization vector, in which the vortex axis is bent into a torus, were discovered in rectangular nanoparticles of PbTiO_3 [29], see Fig. 14(b), and in $\text{BiFeO}_3/\text{BaTiO}_3$ core-shell nanoparticles [165].

These two types of polarization vector winding, the straight vortex winding and toroidal-vortex one, represent the particular configurations of a more general Hopfion texture, where the polarization streamlines realize the helical windings around a set of nested tori as was discussed in Section 4.2.1. This Hopfion texture was simulated in spherical nanoparticles of $\text{PbZr}_{0.6}\text{Ti}_{0.4}\text{O}_3$, in which the closeness to the morphotropic phase boundary reduces the polarization anisotropy [21]. In this compound, used in Sections 4 and 5 as a model exemplary system for describing topological states in ferroelectrics, the main part of the volume is occupied by a Hopfion state, slightly deformed by residual crystal anisotropy, while two smaller regions near the poles contain vortex states.

Furthermore, as demonstrated in Section 4.3.3, the internal cells inside the nanoparticle, which host either vortices or Hopfions, can assume different vortex/Hopfion configurations with approximately the same energy but separated by energy barriers. Transitions between these configurations occur through the reconnection of streamlines, implying a topological phase transition that can be induced by an electric field, elastic deformation, or other external driving forces. A diverse range of topological structures, including vortices, antivortices, hedgehogs, antihedgehogs, and skyrmions, was simulated in conical BaTiO_3 nanoparticles embedded in an SrTiO_3 matrix [26]. They were collectively referred to as a topological eclecton, which aligns with the broader concept of confinement-induced topological states varying with the nanoparticle geometry. The observed mixture of elementary topological states suggests the need for further analysis of streamline configurations and their decomposition on vortices and Hopfions, based on the general Arnold theorem.

The topological states in ferroelectric nanoparticles were observed in the work [31], which demonstrated the presence of a polarization vortex state in BaTiO_3 nanoparticles using Bragg coherent diffractive imaging, see Fig. 14(c). Another significant progress was recently achieved by the 3D reconstruction of polarization topology in BaTiO_3 nanoparticles using annular dark-field scanning transmission electron microscopy (ADF-STEM) [232]. The multiple vortex arrangement was demonstrated through the analysis of the set of sliced polarization maps of Ti atomic displacements, see Fig. 14(d). This work confirmed the initial prediction of the emergence of the vortex matter in confined ferroelectric nanoparticles [37].

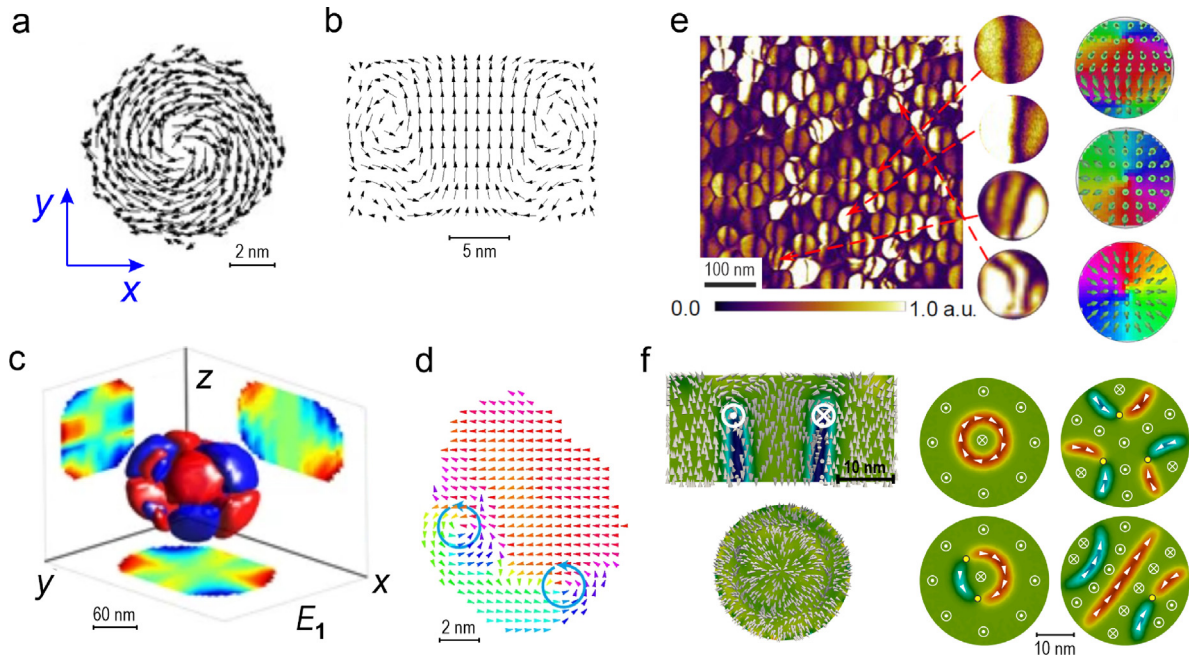


Fig. 14. Ferroelectric nanoparticles and nanodots. (a) Simulations of local dipoles distribution in a disk-shaped nanoparticle of $\text{PbZr}_{0.5}\text{Ti}_{0.5}\text{O}_3$. From Ref. [37]. (b) Simulations of a doughnut vortex in a cubic nanodot of PbTiO_3 . From Ref. [29]. (c) Experimental observation of a three-dimensional nanodomain in a BaTiO_3 spherical nanoparticle. Color map shows x, y, and z components of polarization. From Ref. [31]. (d) Sliced map showing the in-plane distribution of Ti atomic displacements in a BaTiO_3 nanoparticle. The counterclockwise vortices are marked with blue circular arrows. From Ref. [232]. (e) Experimental PFM analysis of the vector field distribution in a cylindrical nanodot of BiFeO_3 , top view. Color vector maps on the right show the reconstructed 2D polarization vector texture. From Ref. [35]. (f) Topological state in a cylindrical nanodot of PbTiO_3 : vertical cross-section view (top left) and top view (bottom left). The right panels demonstrate the field-tuned polarization distribution at the bottom cross-section of the nanodot. From Ref. [16].

The identification of the vortex-like topological states was facilitated by using the unit vector field topological charges, described in Section 2.3.

The obtained experimental results call for the extension of methodologies of the identification and 3D visualization of polarization topological states in nanoparticles. Although the application of numerical indicators characterizing certain features of the polarization vector field serves as a good tool for the initial recognition of the topological states, as we already discussed in Section 6, they do not necessarily capture all essential features. For instance, the calculation of the non-zero vorticity winding number, $N_1 = \deg f_1$, Eq. (3), does not necessarily recognize the presence of the singular vortex inside the integration contour. A meron, see Fig. 2(d), and a helical flux of the vector field, see Fig. 5(d), may give the same value N_1 . The calculation of the toroidal and hypertoroidal moments allows for the identification of the swirling of the polarization field but, at the same time, it does not recognize the chiral states, in particular, those related to the formation of Hopfions. Furthermore, the topological charge N_3 of the homotopy group $S^3 \rightarrow S^2$ in real vector space, given by Eq. (8), does not necessarily detect the ferroelectric Hopfion. In this respect, the described helicity parameter \mathcal{H} defined by Eq. (27) is more useful. However, the calculation of \mathcal{H} requires knowledge of the vector potential \mathbf{A} of the polarization field, which is related to the polarization via $\mathbf{P} = \nabla \times \mathbf{A}$. This requires a complex numerical procedure. Finally, it should be noted that characteristics such as the toroidal and hypertoroidal moments, as well as helicity, provide integral characteristics of a nanoparticle but do not allow for a detailed analysis of the local polarization configurations within nanoparticles.

For identifying internal topological formations, it would be useful to visualize the polarization field, reconstructed from experimental data, using streamlines. As we discussed in this Review, this is a powerful tool for representing polarization fields in ferroelectrics. It may happen, however, that the structure of nanoparticles is not ideal. For example, nanoparticles may contain internal localized charges, or free semiconducting charges, or be in contact with the external charged or conducting nanospecies. Although these effects would perturb the polarization field distribution, as we discussed in Section 5.3.1, small perturbations can be addressed by applying the Helmholtz–Hodge decomposition, as described in Section 2.1.3, to the polarization field, separating it into divergence-free and curl-free components. Topological analysis should be performed on the divergence-free component, while the curl-free component can be used to identify the locations of internal charges. Additionally, regions where the polarization leaks from the nanoparticle may indicate the presence of external electrodes or charges.

7.2.3. Nanodots

The precise control over the positions of nanodots and the distances between them allows to use the efficient advanced microscopy-based characterization techniques for the study of the polarization distribution hosted by nanodots. A significant advancement in the study of topological polarization states in high-density arrays of BiFeO₃ ferroelectric nanodots, with lateral sizes around 60 nm, has been achieved using the advanced technique of vector piezoresponse force microscopy (PFM) imaging [35,36], see Fig. 14(e), left part. The processing of the PFM images enabled the discovery of formation of different types of polarization arrangements, including center-convergent, center-divergent, and double-center domains, as illustrated in the right part of Fig. 14(e).

Unfortunately, the existing PFM images treatment makes visible only the averaged near-surface distribution of the polarization. To reconstruct the full three-dimensional polarization distribution within the nanodots, the more detailed analysis is necessary. To develop such an analysis it is useful to compare the existing experimental material with the phase-field simulations, which were performed in disk-shaped nanodots of PbTiO₃ deposited on a conducting substrate [16]. Chiral bubbles were shown to emerge under appropriate compressive misfit strain, $u_m \simeq -0.002$, with a nanodot diameter of 40 nm and a thickness of 20 nm. The left part of Fig. 14(f) presents the top- and vertical cut views of the polarization distribution. These structures were termed “skyrmions” based on their polarization distribution at the bottom horizontal cross-sections. However, they actually represent the 3D structure of a half-Hopfion, which transforms into a complete chiral Hopfion due to the mirror boundary condition at the conducting substrate plane. Notably, a broader range of possible topological states, driven by the electric field, was discovered in this system, exhibiting textures similar to those observed experimentally in [35,36].

7.3. Nanorods and nanowires

Nanorods and nanowires, long cylindrical nanoparticles with cross-sections on the order of tens of nanometers, represent another family of nanostructured ferroelectrics [235]. Synthesized already in the 90's [236], they remain underexplored compared to other nanostructured ferroelectrics, especially regarding polarization distribution. Theoretical considerations indicate that there are two possible principal directions of polarization promoted by the axial symmetry of the nanorods, namely, either along or perpendicular to their axis. Similarly to magnetism, we refer to the first case as an easy-axis symmetry and to the second one as an easy-plane symmetry. The realization of either possibility depends on the polarization anisotropic energy induced by the surface tension [231,237] or external uniaxial tension [40].

Fig. 15(a) illustrates the diverse polarization states that emerge in ferroelectric nanorods under varying applied tensions. The tensile tension along the nanotube axis induces an easy-axis anisotropy causing the polarization to elongate uniformly along the entire length of the nanorod, resulting in a uniform *c*-phase. In contrast, compressive tension orients the polarization perpendicular to the nanotube axis. However, this orientation leads to polarization impinging on the nanorod walls, generating energetically costly bound charges and the associated depolarization fields. To avoid the formation of the bound charges, polarization may swirl into a vortex, coaxial with the nanorod axis [38], forming the vortex *v*-phase. Both phases, *c* and *v*, are achiral. However, at certain tensions, the intermediate state between the *c*- and *v*-phases in which the polarization is inclined with respect to the nanorod axis is also possible. Similar to the vortex case, to avoid the emergence of bound charges at the boundary, the polarization rotates around the nanotube axis, forming the helical chiral *h*-phase [40].

In theoretical considerations, the nanotube is assumed to be infinitely long, leading to a polarization distribution that typically appears either uniform or periodic along its length. This scenario can be described using the concept of identifying and matching certain cylindrical cross-sections of the nanotube where the polarization distribution is identical, as illustrated in Fig. 15(b). The resulting configuration is equivalent to a solid torus, as depicted in Fig. 15(c). Such mapping is useful for applying the topological formalism described in this Review. Since the full toroidal space is bounded, the confined space topological hydrodynamics is fully applicable. Indeed, in accordance with Arnold theorem, the streamlines of the uniform *c*-phase are now winding around cylinders, coaxial to the solid torus axis, whereas the streamlines of the *v*-phase and *h*-phase realize the tori winding around the toroidal body of the mapped nanorod.

Importantly, unlike the simply connected space of nanoparticles, the solid torus is a doubly connected manifold which means that not every closed contour inside the solid torus, for instance, the circles surrounding the solid torus hole, can be continuously contracted to a point. On such types of manifolds, the Helmholtz–Hopf decomposition, see Section 2.1.3, allows for the existence of a special class of harmonic vector fields that are simultaneously divergence-free and curl-free. An example of such a field is the toroidal distribution of polarization, see the top panel of Fig. 15(c), in which $\mathbf{P} \sim r^{-1} \mathbf{e}_\varphi$. Here, \mathbf{e}_φ is the unit vector that loops around the central axis of the solid torus, and r is the distance from this axis.

Furthermore, multiply connected manifolds extend the applicability of Arnold theorem beyond the simply connected nanoparticles and suggest the emergence of more complex topological states. A very interesting configuration was discovered already in the first simulation of the polarization in rectangular nanorods of PbZr_{0.5}Ti_{0.5}O₃ [37]. This state presents the system of coupled vortices elongated along the axis *z* of the nanorod with the square cross-section *x*-*y*, as shown in Fig. 15(d). The edges of the vortices on the *x*-plane go through the centers of the vortices in the *y*-plane; two sets of vortices are therefore interconnected like links in a chain. The topological mapping of this structure onto a solid torus with a square cross-section reveals the intricate interweaving of four helical streams, which pierce the solid torus in both the radial and axial directions, see Fig. 15(e).

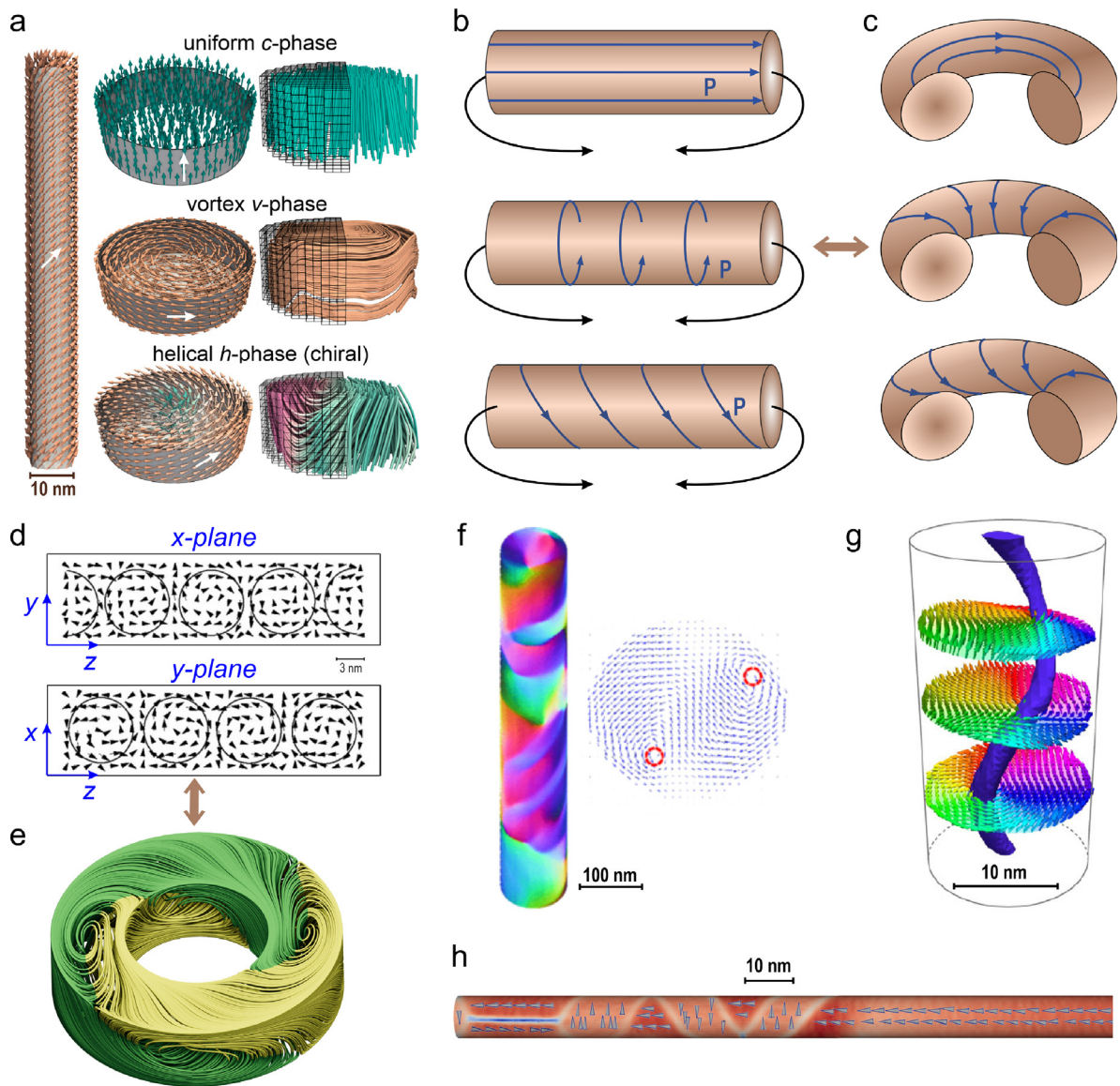


Fig. 15. Ferroelectric nanorods. (a) Simulated strain-driven topological states in a cylindrical nanorod of PbTiO_3 . The right panel shows the uniform c -phase, vortex v -phase, and helical h -phase. The total view of a nanorod hosting h -phase is shown on the left. From Ref. [40]. (b) Matching the equivalent cylindrical cross-sections of a nanotube for topological identification of the emerging phases. (c) Polarization states in the full toroidal manifolds, topologically equivalent to emerging polarization phases in infinite nanotubes. (d) Simulation of local dipoles distribution in a rectangular nanorod of $\text{PbZr}_{0.5}\text{Ti}_{0.5}\text{O}_3$. From Ref. [37]. (e) Mapping the polarization states shown in the previous panel (d) onto a full toroidal manifold. (f) Simulation of a multi-vortex structure in BaTiO_3 nanowires. The color map visualizes domains with different vortex configurations. The right panel shows the horizontal polarization distribution, featuring two vortices at the top face of the nanowire. From Ref. [233]. (g) Simulated helical polarization vortex in nanowires composed of alternating BaTiO_3 and $\text{BaZr}_{0.05}\text{Ti}_{0.95}\text{O}_3$ cylinders. From Ref. [234]. (h) The terminal part of a PbTiO_3 nanorod demonstrating the domain segregation of the c -phase due to depolarization effects is shown on the right. From Ref. [41].

Other complex topological structures that can appear in ferroelectric nanorods have been discussed. In works [15,238], chiral skyrmion-like tubes were revealed in nanocomposites composed of periodic square arrays of BaTiO_3 nanowires embedded within matrices of $\text{Ba}_{0.15}\text{Sr}_{0.85}\text{TiO}_3$ solid solution. It was demonstrated that BaTiO_3 nanowires can host multiple coupled vortices [233], see Fig. 15(f). This finding confirmed earlier predictions of multi-vortex states in nanorods with easy-plane anisotropy [38]. Textures where the core of the h -phase helically rotates around the nanorod axis were discovered in nanorods composed of alternating BaTiO_3 and $\text{BaZr}_{0.05}\text{Ti}_{0.95}\text{O}_3$ cylinders [234], see Fig. 15(g). Another interesting and still underexplored aspect is the structure of chiral domain walls that can arise when helical polarization segments with opposite helicities meet in nanorods, as suggested in magnetic nanotubes [239]. The complete understanding of

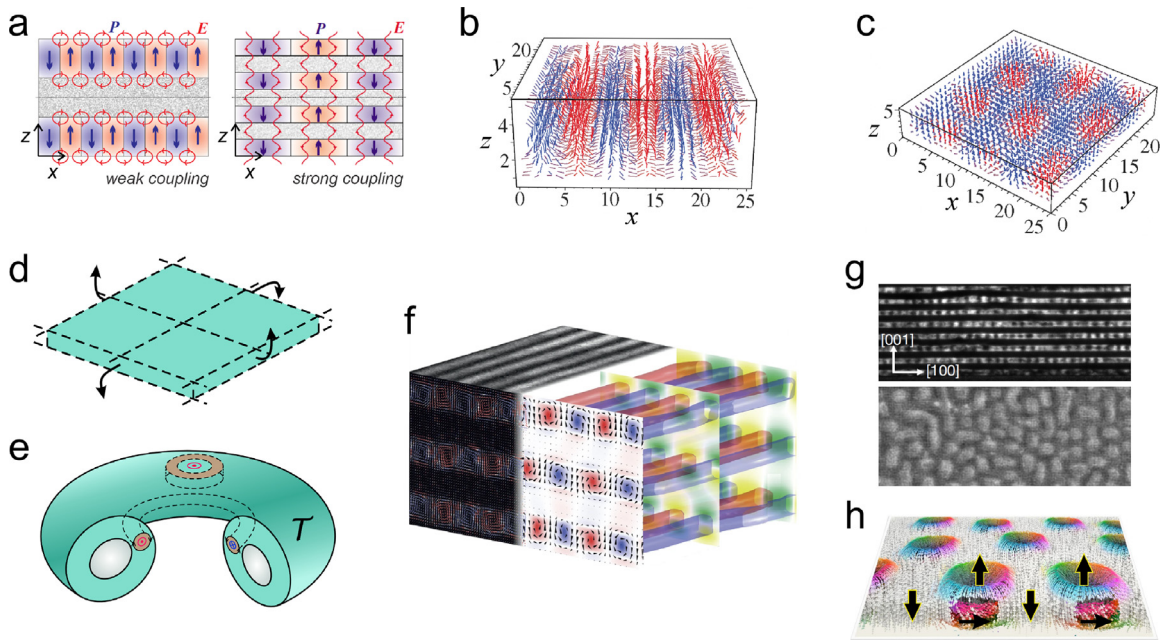


Fig. 16. Ferroelectric heterostructures. (a) The side view of the polarization domains (blue arrows) and depolarization fields (red arrows) in ferroelectric layers in a ferroelectric/dielectric superlattice in weak-coupling and in strong-coupling regimes. The smooth distribution of the spontaneous polarization is demonstrated by varying the color intensity. From Ref. [9,219]. (b) First-principle simulations of polarization stripe vortices in strained films of $\text{PbZr}_{0.5}\text{Ti}_{0.5}\text{O}_3$. From Ref. [10]. (c) First-principle simulations of polarization bubbles in strained films of $\text{PbZr}_{0.5}\text{Ti}_{0.5}\text{O}_3$. From Ref. [10]. (d) The periodic unit cell of the vortex or bubble array and the procedure of adjusting the opposite edges together to make a toroidal shell. (e) Toroidal shell, with the finite-thickness surface, τ , topologically equivalent to the periodic unit cell in the ferroelectric layer. A bubble preserves its Hopfion structure, and a vortex assumes a toroidal winding around a toroidal shell. (f) Experimentally observed vortices in a $\text{SrTiO}_3/\text{PbTiO}_3$ (STO/PTO) superlattice (left) and their phase-field simulation (right). From Ref. [13]. (g) Observation of the ordered structure of polarization bubbles in a STO/PTO superlattice. From Ref. [17]. (h) Simulated bubble array in a STO/PTO superlattice revealing the tori winding polarization structure. The black arrows indicate the polarization direction in the core of the bubble and outside the bubble. From Ref. [18].

the topology of these structures needs further analysis using the mapping on the full toroidal manifold reflecting the connectivity of topological states in the system.

Note, finally, that chiral states can arise at the ends of nanorods hosting the uniform c -phase. The emergence of the depolarization fields at the terminal points at the tops and bottoms of the nanorods leads to the swirling of the polarization at the terminal regions and to the formation of the chiral domains, shown in Fig. 15(h) [41]. The effect of the emergence of specific terminal chiral polarization domains, referred to as flexons, can also be associated with the intervening flexoelectric effect [39].

7.4. Heterostructures

7.4.1. From domains to vortex matter

Over the past two decades, research on ferroelectric systems has primarily concentrated on ferroelectric thin films and ferroelectric/dielectric superlattices, both of which are commonly referred to as heterostructures. The discovery of the polarization domains in ferroelectric heterostructures [8,9,140,219], see Fig. 16(a), remarkably confirmed the applicability of the seminal concept of the Landau–Kittel domain formation [5,139] to ferroelectrics [8,140], resulting from the minimization of the depolarization energy. Atomistic simulations demonstrated that domains in ferroelectrics have the structure of either alternatively rotating vortex stripes, directed along the ferroelectric layers, see Fig. 16(b), or polarization bubbles, Fig. 16(c). The existence of topological states in ferroelectric heterostructures in the form of periodic vortex arrays and periodically arranged polarization bubbles was experimentally confirmed a decade later and has become a central focus in the research of ferroelectric nanostructures. A comprehensive list of reviews on this exciting topic is given in the Introduction, Section 1.

Here we explore the key topological characteristics of vortex matter in ferroelectric heterostructures, focusing on the specific topological properties of the manifolds associated with these structures and highlighting the unique features relevant to each particular type of topological state. The methods of topological hydrodynamics are used for the description. Notably, the close hydrodynamic analogy of the observed polarization patterns is a self-organizing nonlinear convection pattern emerging in a liquid heated from the bottom, known as Bénard cells [240]. Each cell is a “vortex-like” formation with rotating convection: the convection fluxes go up at cells’ borders and fall through to the bottom at the cell centers. Similar to ferroelectric vortices, the cells may be arranged in stripes, bubbles, or disordered labyrinths.

7.4.2. Topological manifolds of heterostructures

We characterize now the topological features of the coordinate space manifolds, corresponding to ferroelectric heterostructures. We start with ferroelectric films, by noting that they differ from nanoparticles by the type of confinement. While particles are confined in all three spatial directions, films are confined in the dimension perpendicular to the film and extend to infinity in two others. This change in confinement dimensionality extends the original assumption of the bounding of the system space which we apply to nanoparticles.

To realize this extension, note that most of the observed topological states form periodic structures, allowing us to adjust the boundaries of the periodically repeating rectangular unit cell, see Fig. 16(d). This maps the system onto a toroidal shell, \mathcal{T} , having a structure of torus with the finite-thickness surface corresponding to the thickness of the film, see Fig. 16(e). In other words, the system becomes topologically equivalent to a bounded nanoparticle shaped like a toroidal shell, where topological states can have two orientations: longitudinal and transversal. The axis of these states either loops around the hole of the torus, corresponding to stripe vortex domains, or pierces through the toroidal shell, corresponding to vortex bubbles, as illustrated in Fig. 16(e). In both scenarios, these states are structured as nested toroidal surfaces, around which polarization lines wind, representing unique toroidal or cylindrical winding topological states.

Turning now to ferroelectric/dielectric superlattices, we note that in these structures, the polarization field of the periodic ferroelectric domains may slightly extend into the adjacent dielectric layers. This phenomenon appears as the fringing of the polar vortices beyond the boundaries of the ferroelectric layer. Such spreading of the polarization field reduces the gradient energy of confined vortices, shifting the polarization surface singularities to the points where the interfaces of two oppositely winding vortices meet the ferroelectric surface. However, the additional polarization of the dielectric space costs substantial energy. Accordingly, the value of the emerging flux is small and does not exceed 8%–10% of the total flux confined inside the ferroelectric layer. Nevertheless, the interaction between polarization fluxes emerging from adjacent ferroelectric layers separated by a dielectric layer can lead to the coupling of domain polarization structures within these layers. The strength of this coupling is determined by the degree of the flux overlap.

Two different regimes of coupling of the domain structures are depicted in Fig. 16(a), [219]. In a weak coupling regime, realized typically in cases where the characteristic period of the domain structure is smaller than the thickness of the dielectric layer, each ferroelectric layer can be considered as a practically independent ferroelectric film. In the opposite limit of the strong coupling, the emerging polarization structures in adjoining ferroelectric layers interact more noticeably with each other. This regime is realized when the thickness of the ferroelectric/dielectric layers becomes comparable to or smaller than the period of the polarization domain structure. In such a strong coupling regime, the polarization fluxes of domains not only escape from the original ferroelectric layer but also enter the next ferroelectric layer, propagating from one layer to another. Furthermore, the coherent polarization periodicity in the third, out-of-plane direction, may appear, and when the coupling becomes dominating, the system may recover the uniform polarization distribution. These structures predicted in [219] were then simulated in [241,242].

The established periodicity in all three directions is described by the 3D elementary cell with periodic boundary conditions. Topologically it corresponds to the 3D toroidal manifold, T^3 , obtained by the adjustment of the opposite faces of this cell, see Section 2.1.2. This manifold serves as an effective manifold for analyzing the emergent topological states in strongly coupled ferroelectric superlattices.

7.4.3. Vortex arrays

The polarization stripe domains in ferroelectric heterostructures have the structure of arrays of periodically arranged vortices with alternating clockwise (CW) and counterclockwise (CCW) polarization rotations, with each pair of vortices forming one unit cell. They can have either a singular structure of their cores, as was originally observed in [13], see Fig. 16(f), or have the polarization component tangential to the core, allowing to avoid the singularity and providing the vortex with the helical chiral structure. Experiments show that the direction of this tangential component in the core can either alternatively vary from vortex to vortex [227] or maintain the same direction for all vortices [175]. Accordingly, after topological mapping of the two-vortex unit cell onto the toroidal shell manifold of the system, \mathcal{T} , the CC and CCW rotating vortex pairs enclose into two longitudinal tori with central axes forming concentric circles, each with oppositely oriented poloidal polarization winding around these central axes. One of these tori is shown in Fig. 16(e). The necessarily pairwise emergence of the polarization-winding tori inside the toroidal shell is the direct consequence of the multi-connectivity of the coordinate space of the system, ensuring the continuity of the vector field through the whole multiply connected manifold.

7.4.4. Skyrmion bubbles

A periodic system of cylindrical polarization bubbles was first experimentally observed in [17,18], see Fig. 16(g), and Fig. 16(h) for corresponding simulations. As shown in Fig. 16(h), the polarization within the central core part of the bubble domains is oriented in the upward out-of-plane direction, while the polarization between the bubbles is directed downward. Inside the bubbles, the simulated polarization streamlines wind around nested tori. This indicates that the polarization bubble possesses the structure of a complete Hopfion, as described in Section 4.2.1. Notably, in the horizontal cross-sections of a bubble, the polarization makes a 180° U-turn when going from its axis to the periphery similar to what happens in 2D skyrmions. Accordingly, these bubbles were called “skyrmions” or “skyrmion bubbles”.

All skyrmion bubbles in such a configuration are identical implying that an elementary cell of the periodic lattice of the bubbles contains only one item per unit cell. This corresponds to a single transversal Hopfion in the toroidal shell after mapping the unit cell to \mathcal{T} , see Fig. 16(e). However, the state formed by such a configuration may not be the most stable state because the surface bound charges produced by the downcoming polarization flux, located in the inter-bubble space, substantially exceeds the surface bound charges produced by the oppositely oriented polarization flux, located in the bubble cores, see Fig. 16(h). This results in the uncompensated depolarization fields in the ferroelectric layer, hence in the large depolarization energy.

The reduction of depolarization energy, resulting from an excess of surface bound charges in the inter-bubble space, may be achieved by densifying the bubble array. This densifying can be, in turn, accomplished by packing bubbles with alternating CW and CCW vorticity. Notably, in this case, the polarization vector does not realize a full U-turn when transitioning from one Hopfion to another, resulting in their incompleteness. This imposes certain conditions on matching the polarization vector fields created by the neighboring bubbles. In this case, the 2D projection of the polarization field for the entire system resembles the texture of a periodic array of merons, referred to as meron bubbles in experimental works [23–25].

7.4.5. Meron bubbles

Fig. 17(a) displays the 4D STEM observation of a periodic array of meron bubbles appearing in a strain-free STO/PTO superlattice, obtained in experiments conducted at temperature $T = 298\text{ K}$ [25]. The enlarged image of the in-plane mapping of the polarization field is shown in Fig. 17(b). The reconstructed distribution of the polarization vector field, as shown in Fig. 17(c), identifies the observed structure as an array of the bubbles with alternative CW and CCW rotations and upcoming flux at the cores of the bubbles. Notably, this flux is compensated by the downward flux at the interstitial sites of the bubble lattice, where the polarization of the in-plane component exhibits an antivortex structure.

It is important that the vector field configuration in Fig. 17(c) presents the 2D projection of the STEM image on the horizontal plane of the ferroelectric layer. The reconstruction of the 3D structure of the polarization vector field, achieved through the phase-field simulation, reveals a significantly more complex structure. As shown in Fig. 17(d), the streamlines of the reconstructed polarization have the Hopfion structure characterized by their toroidal winding. In such a structure, the polarization streamlines are localized within a single Hopfion and do not jump to its neighbors, as shown in Fig. 17(e). Fig. 17(f) demonstrates the image of the vector field resulting from the averaging of the reconstructed 3D vector over the film thickness. It assumes the structure of an array composed of CW and CCW merons with upward polarization at the cores, closely resembling the experimental observation shown in panels (a)–(c) of Fig. 17.

Fig. 17(g) displays another arrangement of CCW and CW skyrmion bubbles, possible but not yet observed experimentally. This configuration differs from the previous ones by the polarity of the bubble cores. The upward polarization flux in CCW bubbles spreads over to adjacent CW bubbles, merging into downward polarization fluxes in their cores. Then, this flux completes a circuit by reconnecting to the upward flux at the bottom of the bubble. Meanwhile, the interstitial sites of the bubble lattice remain flux-neutral. Such sharing of polarization flux between the bubbles links them into a coherent collective array through the interconnected polarization field lines, as shown in Fig. 17(h). Notably, the interlinked polarization bubbles shown in Fig. 17(g) cannot be described as a single Hopfion located within a simply connected coordinate topological manifold. Similar to the chain-linked topological states in nanorods, shown in Fig. 15(d), there is a need to extend Arnold theorem to accommodate the polarization topological states within the multi-connected manifold of toroidal shell, shown in Fig. 16(e). From an experimental perspective, identifying the interlinked meron bubbles can be achieved using the image of the vector field averaged over the film thickness, as shown in Fig. 17(i). This is particularly relevant for the 3D reconstruction of polarization fields from STEM or PFM data.

7.4.6. Labyrinths

Fig. 17(g) presents an experimental STEM image of the polarization bubble array obtained in the same system as the system shown in Fig. 17(a), but at temperature $T = 373\text{ K}$ [25]. Here, in addition to the regular bubble structure, exemplified by the yellow square, one observes also the disordered pattern of the bubbles, exemplified by the blue square and referred to as a labyrinth structure. The similar disordered labyrinth-like texture of the polarization bubbles was characterized in [22] as a self-patterned domain structure harboring concave and convex disclinations, saddle defects, meron-antimeron pairs, bimerons, skyrmions, target skyrmions, and dislocations.

Yet the phase-field modeling of this structure, displayed in Fig. 17(k,l), shows that the polarization texture extended to the 3D volume of the ferroelectric layer can be decomposed into an array of Hopfion cells. Furthermore, despite the seemingly chaotic structure of the polarization vector field, the repartition of the system into the cells implies the nonergodicity of the system, as described in Section 5.2. It is likely that structural transitions between different regular polarization configurations, such as between regular vortex arrays and regular skyrmion/meron bubble arrays, occur through such an intermediate labyrinth state. This transition happens via the rearrangement of topological cells and the Hopfions within these cells.

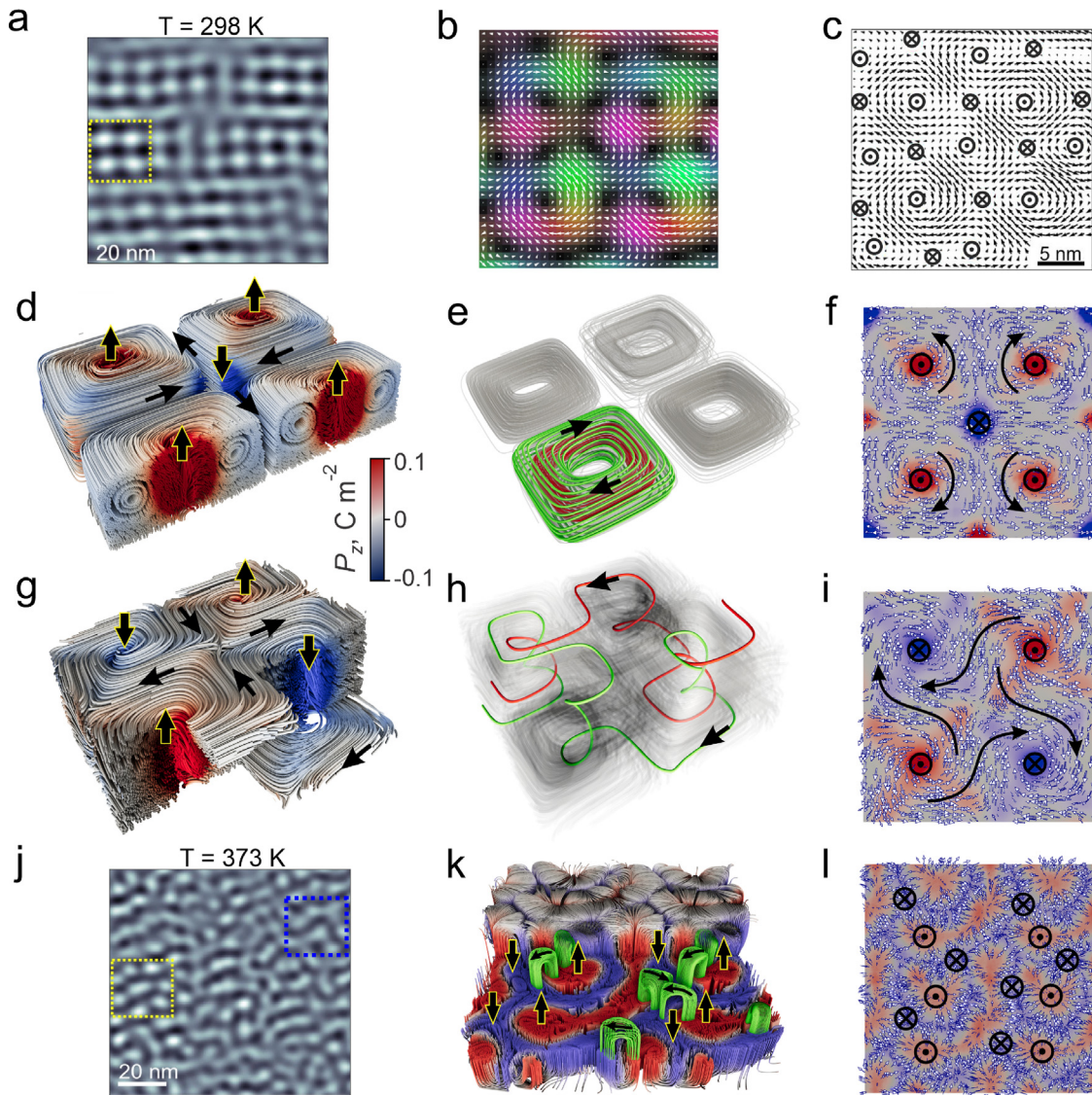


Fig. 17. Meron bubbles and labyrinths in ferroelectric heterostructures. (a) The experimental observation of a regular array of meron bubbles in a strain-free STO/PTO superlattice. From Ref. [25]. (b) Enlarged in-plane polarization mapping of the yellow box region in panel a. From Ref. [25]. (c) Schematic presentation of the distribution of the polarization vector field in the meron bubble array, shown in panels a and b. Dots within circles represent polarization fluxes pointing out of the page, while crosses within circles indicate fluxes pointing into the page. From Ref. [25]. (d) Cross-cut view of the phase-field reconstruction of polarization structure in a periodic cell of the dense array of the polarization bubbles with the same core polarity, demonstrating the torus-winding of the polarization streamlines. The black arrows show the direction of the polarization vector field. The color corresponds to the value of the P_z component. (e) Families of streamlines, depicted in red and green, wind around nested tori sets that are localized within one of the bubbles in the meron bubble array, as shown in panel d. (f) The thickness-averaged vector field shown in panel d demonstrates similarity to the experimental observations presented in panel c. (g) Cross-sectional view of the polarization structure in the periodic cell of a dense array of bubbles with alternating core polarities, demonstrating the coupling of bubbles through the overflow of polarization streamlines. (h) Exemplary red and green streamlines migrating from one bubble to another in the bubble array, shown in panel g. (i) Thickness average of the shown in the panel g vector field. (j) The labyrinth-like disordered array of polarization bubbles (blue square) and regular array of skyrmion bubbles (yellow square), observed in a strain-free STO/PTO superlattice. From Ref. [25]. (k) Corner-cut view of the same system demonstrates that the actual polarization texture consists of an array of tori-winding cells, with exemplary Hopfions highlighted in green. (l) Thickness average of the vector field shown in panel k demonstrates a similarity to the experimental observation presented in panel j.

7.5. Bulk

As discussed in the previous sections, the confinement of ferroelectric materials is a crucial factor for the formation of polarization topological states. Topological states can also emerge in bulk systems under specific conditions where the system imposes certain geometrical constraints or non-uniformities. In this Section, we explore such examples of bulk

systems in which the interplay between geometry, internal structuring of the material, and depolarization effects leads to intricate topological phenomena.

Nanocomposite ferroelectrics, in which ferroelectric nanoparticles are embedded within a matrix of other materials, are of significant interest for various applications due to their unique properties. The influence of nanoparticle confinement on the emergence of topological polarization states is strongly affected by the nanoparticles packing density, as illustrated in Fig. 18(a). As a representative example, we consider inclusions of spherical nanoparticles of $\text{PbZr}_{0.4}\text{Ti}_{0.4}\text{O}_3$, of radius $R = 25$ nm, embedded into a matrix of dielectric material with $\varepsilon \simeq 10$. In this configuration, the polarization field confined within each nanoparticle can transfer between adjacent nanoparticles through “hot spots” at their junctions, forming chiral helical streams. The topological states within these nanoparticles resemble those observed in isolated nanoparticles with external electrodes or external sources of charge, see Section 5.3.4.

Phase-field simulations of such structures [21] reveal that topological states hosted by the network of connected spherical nanoparticles are highly sensitive to the degree of densification. The left panel of Fig. 18(b) illustrates the configuration of streamlines in adjacent nanoparticles under moderate densification conditions. In this scenario, only a portion of the helical polarization streamlines passes through the interfacial apertures. The resulting helical vortex either pierces or surrounds a localized Hopfion. Therefore, within each nanoparticle, the polarization texture splits into two distinct chiral topological states: a localized Hopfion, which does not contribute to flux transfer between nanoparticles, and a flux-transferring helical vortex that traverses the nanoparticle and connects with other nanoparticles via the hot spots. In contrast, when nanoparticles are densely packed, all polarization field lines form helices that flow through the contact areas between nanoparticles, as depicted in the right panel of Fig. 18(b).

A similar configuration of inter-communication between nanoparticles by virtue of the helically screwed streamlines was studied in [243], see Fig. 18(c). The remarkable feature of such systems is that depending on the strength of electrostatic interaction between nanoparticles, the topological states emerging in individual nanoparticles get combined into the complex global topological network of the polarization streamlines. Furthermore, these states can be switched by external fields either on the individual or on the collective level, offering a platform for the perspective of optoelectronic and computing devices.

An interesting situation arises in the bulk of disordered ferroelectric materials where the structural or compositional disorder is coupled with the polar degrees of freedom. Then, in order to avoid the formation of depolarization charges, the non-uniform polarization field swirls into the bubble configurations, either vortices or Hopfions. Such self-confined bubble-like features with multiple polar topologies were recently observed in bulk $\text{Bi}_{0.5}\text{Na}_{0.5}\text{TiO}_3$ relaxor-ferroelectric, having chemically-driven disorder morphology [19], see Fig. 18(d). Fig. 18(e) presents the simulation of polarization distribution in $\text{PbZr}_{0.6}\text{Ti}_{0.4}\text{O}_3$ ferroelectrics, in which the spatially non-uniform Gaussian distribution of critical temperature mimics the structural disorder, and shows the highly entangled structure of the streamlines which tangle into toroidal knots, forming the Hopfion tori winding streamlines configurations. Understanding the topology of disordered ferroelectrics as a composition of the Hopfion topological states is important not only because it holds high potential for applications but since it posits a deep fundamental appeal. This concept offers ways of targeted manipulation of space-disordered chirality by operating individual Hopfions, thus enabling the groundbreaking technology of neuromorphic nano-optoelectronics. On the other hand, it sheds light on the seminal problem of the physics of ferroelectric relaxors.

Topological consideration of the highly branched polarization fluxes in bulk ferroelectrics has been recently employed in the uniaxial ferroelectric lead germanate, $\text{Pb}_5\text{Ge}_3\text{O}_{11}$ (PGO), to explain the puzzling phenomenon of experimentally observed head-to-head and tail-to-tail meetings of oppositely oriented polarization domains [80]. Such a configuration is well known to lead to uncompensated bound charges at the domain wall surface, resulting in the emergence of strong depolarization fields that can destroy ferroelectricity [8,222]. However, comparing the polarization structures of meeting oppositely oriented domains with the encounter of fluid streams, where instead of colliding they bifurcate and freely separate, provides a simple and intuitively clear solution to this paradox using the approach of topological hydrodynamics. In this configuration, as shown in Fig. 18(f), the polarization vector field remains divergence-free, and bound charges do not emerge. Importantly, the ∇ -point of domain bifurcation corresponds to the singular saddle point of the polarization vector field, $\mathbf{P}(\mathbf{r})$, described in Section 2.2.2. The topological stability of this point secures the topological stability of the entire system involving intersecting fluxes. The presence of this singular saddle point at the interface between encountering domains has been confirmed [80] both by the numerical simulation of the domain wall, see Fig. 18(g), and experimentally, Fig. 18(h).

To conclude here, the topological methods covering the intricate interplay between geometry, internal structuring, and dynamics play an exclusively important role in exploiting the unique properties of confined and bulk ferroelectrics.

8. Conclusion

Thanks to recent theoretical predictions and experimental discoveries of novel exotic polarization nanostructures in ferroelectrics, the investigation of ferroelectrics has become a fast-growing direction of physics. The interest is motivated not only by an intellectual appeal of the involved fundamental problems but also by the high potential that this field holds for key modern technologies, especially nanoelectronics. At the same time, the fast development of the field may result in the natural flip side of the coin, which is the use of different approaches to the same physical phenomena that sometimes may demonstrate seeming contradictions because of utilizing different terms. For instance, the interpretation

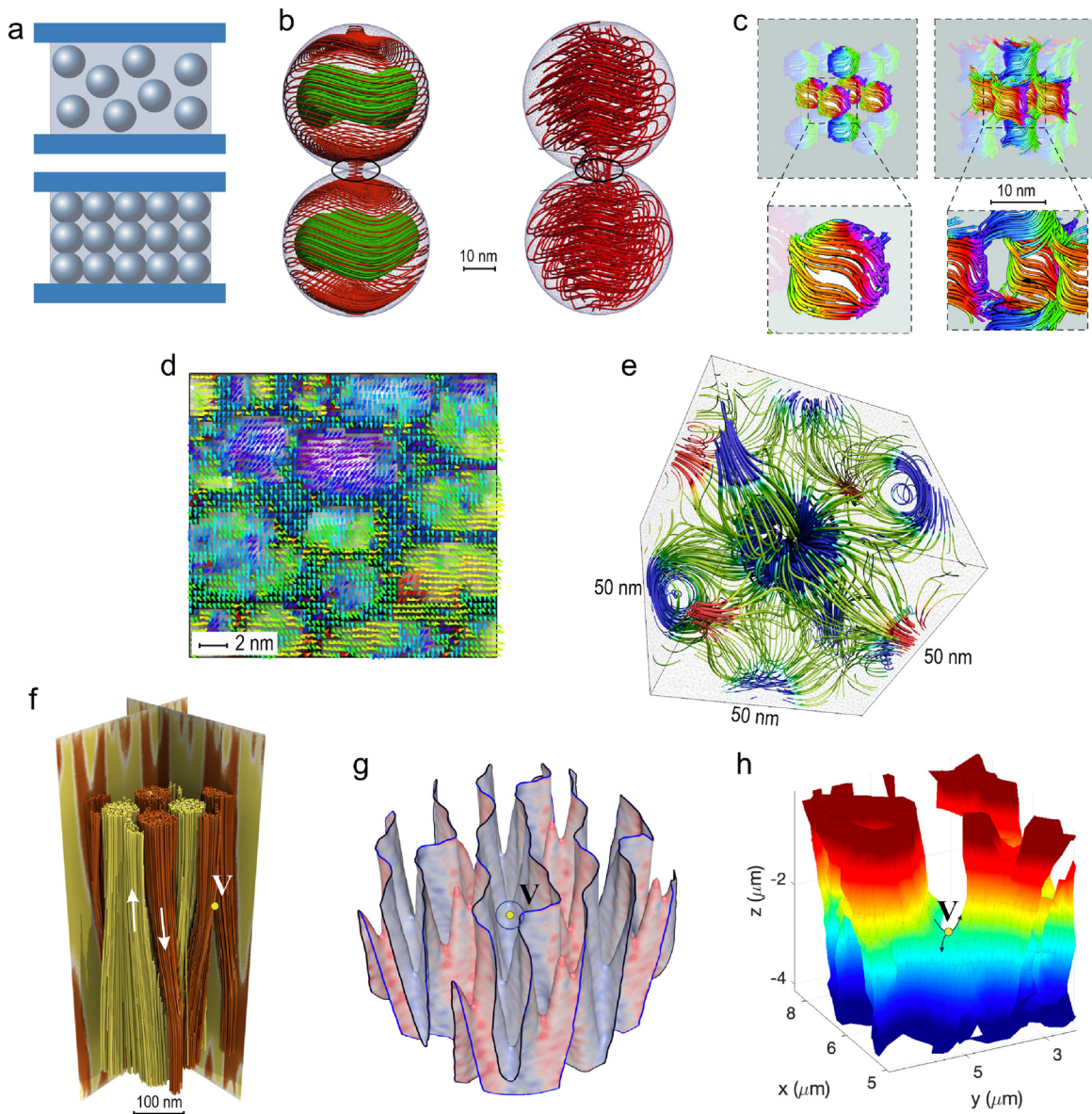


Fig. 18. Polarization structures in composites and disordered bulk ferroelectrics. (a) Dilute composite of isolated nanoparticles in a capacitor and sintered composite of contacting nanoparticles. (b) (Left part) Field lines' flow between moderately densified nanoparticles of $\text{PbZr}_{0.6}\text{Ti}_{0.4}\text{O}_3$ with radius $R = 25$ nm, contacted along the $[111]$ direction. The densification degree is characterized by the thickness of the connecting neck $2h = 0.4$ nm. The delocalized helical lines flowing between the particles are embraced by the localized lines forming the toroidal Hopfion-like states. (Right part) In a composite of strongly densified nanoparticles of the same size and material but with the thickness of the connecting neck $2h = 2$ nm, all the field lines form delocalized helices flowing across the entire composite. From Ref. [21]. (c) Polarization distribution in ferroelectric nanostructures formed in the face-centered cubic nanoporous SrTiO_3 . From Ref. [243]. (d) Atomically resolved contrast-inverted STEM ABF image of bulk $\text{Bi}_{0.5}\text{Na}_{0.5}\text{TiO}_3$ sample with ferroelectric bubbles. The $\delta_{\text{Ti-O}}$ displacement vector maps overlaid on their corresponding polarization intensity; the displacement vectors are indicated as colored arrows according to their rotation angles, and the polarization intensity is indicated by bright–dark contrast. From Ref. [19]. (e) Simulation of the polarization distribution in $\text{PbZr}_{0.6}\text{Ti}_{0.4}\text{O}_3$ ferroelectrics where the space non-uniform Gaussian distribution of critical temperature mimics structural disorder. (f) Visualization of the complex network of polarization lines formed by the counter-flowing polarization fluxes in uniaxial ferroelectric crystal $\text{Pb}_5\text{Ge}_3\text{O}_{11}$ (PGO), corresponding to the “up” and “down” polarization domains, encountering and diverging at the singular saddle point ∇ . (h) The simulated domain wall between the “up” and “down” polarization domains in PGO. (g) 3D domain wall reconstruction obtained from PFM tomography in PGO. The color scale represents the height along the crystal axis. Panels (f)–(g) are adopted from Ref. [80].

of the observed polarization states may be based on the surface-imaging experiments, in which the effects of the 3D confinement are difficult to realize because of insufficient development of analytical topological methods.

Our Review addresses this issue and proposes a general topological approach to the physics of ferroelectrics. Based on the in-depth review of the state-of-the-art experimental and modeling results and building on their synergy with a

pioneering mathematical discipline, topological hydrodynamics, we reveal that the emerging structures in ferroelectrics are the embodiments and manifestations of the fundamental topological hydrodynamics formations, like vortices and Hopfions. The discovered principles pave the way for further developing a quantitative description of ferroelectrics by exploring the crossroads of advanced mathematical branches such as Lie groups, knot theory, stability theory, theory of volume-preserving diffeomorphisms, systems integrability, geometric inequalities, and symplectic geometry. The topological hydrodynamic approach enables a profound understanding of the functional properties of ferroelectrics, especially, those related to the dynamics and plasticity of polarization fluxes that are of prime importance for emergent applications, including neuromorphic and multilevel-logics computing and ultrafast terahertz communications.

CRedit authorship contribution statement

Igor A. Lukyanchuk: Conceptualization, Data curation, Formal analysis, Investigation, Methodology, Resources, Software, Supervision, Validation, Writing – original draft, Writing – review & editing. **Anna G. Razumnaya:** Conceptualization, Data curation, Formal analysis, Investigation, Methodology, Resources, Software, Validation, Visualization, Writing – original draft, Writing – review & editing. **Svitlana Kondovych:** Conceptualization, Data curation, Formal analysis, Investigation, Methodology, Software, Validation, Visualization, Writing – original draft, Writing – review & editing. **Yuri A. Tikhonov:** Conceptualization, Data curation, Formal analysis, Investigation, Methodology, Software, Validation, Visualization, Writing – original draft, Writing – review & editing. **Boris Khesin:** Conceptualization, Data curation, Formal analysis, Investigation, Methodology, Software, Supervision, Visualization, Writing – review & editing. **Valerii M. Vinokur:** Conceptualization, Data curation, Formal analysis, Investigation, Methodology, Software, Supervision, Writing – original draft, Writing – review & editing.

Declaration of competing interest

The authors declare that they have no known competing financial interests or personal relationships that could have appeared to influence the work reported in this paper.

Acknowledgments

This research was financially supported by the European Union HORIZON-WIDERA-2022-TALENTS-ERA Fellowship-FerroChiral (GA 101090285), by Terra Quantum AG, and by the European Union H2020-MSCA-RISE-MELON action, project number 872631. S.K. acknowledges the support from the Alexander von Humboldt Foundation. A.R. acknowledges the Slovenian Research Agency support (P1-0125). This work was granted access to HPC resources of “Plateforme MatriCS” within University of Picardie Jules Verne. “Plateforme MatriCS” is co-financed by the European Union with the European Regional Development Fund (FEDER) and the Hauts-De-France Regional Council among others.

Appendix A. Supplementary data

Supplementary material related to this article can be found online at <https://doi.org/10.1016/j.physrep.2025.01.002>.

References

- [1] Jorge V. Jos, *40 Years of Berezinskii-Kosterlitz-Thouless Theory*, World Scientific, 2013.
- [2] Lars Brink, Mike Gunn, Jorge V Jose, John Michael Kosterlitz, Kok Khoo Phua, *Topological Phase Transitions and New Developments*, World Scientific, 2019.
- [3] Roderich Moessner, Joel E. Moore, *Topological Phases of Matter*, Cambridge University Press, 2021.
- [4] S Das, Z Hong, M McCarter, P Shafer, Yu-Tsun Shao, DA Muller, LW Martin, R Ramesh, A new era in ferroelectrics, *APL Mater.* 8 (12) (2020) 120902.
- [5] Lev Davidovich Landau, Evgeny M. Lifshitz, On the theory of the dispersion of magnetic permeability in ferromagnetic bodies, *Phys. Z. Sowjetunion* 8 (153) (1935) 101–114.
- [6] Rudolf Huebener, *Magnetic Flux Structures in Superconductors: Extended Reprint of a Classic Text*, vol. 6, Springer Science & Business Media, 2001.
- [7] Alex Hubert, Rudolf Schäfer, *Magnetic Domains: the Analysis of Magnetic Microstructures*, Springer Science & Business Media, 2008.
- [8] A.M. Bratkovsky, A.P. Levanyuk, Abrupt appearance of the domain pattern and fatigue of thin ferroelectric films, *Phys. Rev. Lett.* 84 (14) (2000) 3177–3180.
- [9] V.A. Stephanovich, I.A. Lukyanchuk, M.G. Karkut, Domain proximity and ferroelectric transition in ferro-paraelectric superlattices, *Ferroelectrics* 291 (1) (2003) 169–175.
- [10] Igor Kornev, Huaxiang Fu, L. Bellaiche, Ultrathin films of ferroelectric solid solutions under a residual depolarizing field, *Phys. Rev. Lett.* 93 (19) (2004) 196104.
- [11] Alexander Kirillovich Tagantsev, L. Eric Cross, Jan Fousek, *Domains in Ferroic Crystals and Thin Films*, vol. 13, Springer, 2010.
- [12] Pavlo Zubko, N Jecklin, Almudena Torres-Pardo, P Aguado-Puente, A Gloter, Céline Lichtensteiger, J Junquera, O Stéphan, J-M Triscone, Electrostatic coupling and local structural distortions at interfaces in ferroelectric/paraelectric superlattices, *Nano Lett.* 12 (6) (2012) 2846–2851.
- [13] AK Yadav, CT Nelson, SL Hsu, Z Hong, JD Clarkson, CM Schlepütz, AR Damodaran, P Shafer, E Arenholz, LR Dedon, et al., Observation of polar vortices in oxide superlattices, *Nature* 530 (7589) (2016) 198.
- [14] Qi Zhang, Lin Xie, Guangqing Liu, Sergei Prokhorenko, Yousra Nahas, Xiaoqing Pan, Laurent Bellaiche, Alexei Gruverman, Nagarajan Valanoor, Nanoscale bubble domains and topological transitions in ultrathin ferroelectric films, *Adv. Mater.* 29 (46) (2017) 1702375.

- [15] Y Nahas, S Prokhorenko, L Louis, Z Gui, Igor Kornev, Laurent Bellaiche, Discovery of stable skyrmionic state in ferroelectric nanocomposites, *Nature Commun.* 6 (2015) 8542.
- [16] Yu Tikhonov, S Kondovych, J Mangeri, M Pavlenko, Laurent Baudry, A Sené, A Galda, S Nakhmanson, O Heinonen, A Razumnaya, I Luk'yanchuk, VM Vinokur, Controllable skyrmion chirality in ferroelectrics, *Sci. Rep.* 10 (1) (2020) 8657.
- [17] S Das, YL Tang, Z Hong, MAP Gonçalves, MR McCarter, C Klewe, KX Nguyen, F Gómez-Ortiz, P Shafer, E Arenholz, et al., Observation of room-temperature polar skyrmions, *Nature* 568 (7752) (2019) 368.
- [18] Sujit Das, Zijian Hong, VA Stoica, MAP Gonçalves, Yu-Tsun Shao, Eric Parsonnet, Eric J Marks, Sahar Saremi, M.R. McCarter, A. Reynoso, et al., Local negative permittivity and topological phase transition in polar skyrmions, *Nature Mater.* 20 (2) (2021) 194–201.
- [19] Jie Yin, Hongxiang Zong, Hong Tao, Xuefei Tao, Haijun Wu, Yang Zhang, Li-Dong Zhao, Xiangdong Ding, Jun Sun, Jianguo Zhu, et al., Nanoscale bubble domains with polar topologies in bulk ferroelectrics, *Nature Commun.* 12 (1) (2021) 1–8.
- [20] S Prokhorenko, Y Nahas, V Govinden, Q Zhang, N Valanoor, L Bellaiche, Motion and teleportation of polar bubbles in low-dimensional ferroelectrics, *Nature Commun.* 15 (1) (2024) 412.
- [21] I. Luk'yanchuk, Y. Tikhonov, A. Razumnaya, V.M. Vinokur, Hopfions emerge in ferroelectrics, *Nature Commun.* 11 (1) (2020) 1–7.
- [22] Y Nahas, S Prokhorenko, Q Zhang, V Govinden, N Valanoor, L Bellaiche, Topology and control of self-assembled domain patterns in low-dimensional ferroelectrics, *Nature Commun.* 11 (1) (2020) 1–8.
- [23] YJ Wang, YP Feng, YL Zhu, YL Tang, LX Yang, MJ Zou, WR Geng, MJ Han, XW Guo, B Wu, et al., Polar meron lattice in strained oxide ferroelectrics, *Nature Mater.* 19 (8) (2020) 881–886.
- [24] Daniel Bennett, Gaurav Chaudhary, Robert-Jan Slager, Eric Bousquet, Philippe Ghosez, Polar meron-antimeron networks in strained and twisted bilayers, *Nature Commun.* 14 (1) (2023) 1629.
- [25] Yu-Tsun Shao, Sujit Das, Zijian Hong, Ruijuan Xu, Swathi Chandrika, Fernando Gómez-Ortiz, Pablo García-Fernández, Long-Qing Chen, Harold Y Hwang, Javier Junquera, et al., Emergent chirality in a polar meron to skyrmion phase transition, *Nature Commun.* 14 (1) (2023) 1355.
- [26] Sergey Prosandeev, S. Prokhorenko, Y. Nahas, L. Bellaiche, Prediction of a novel topological multidefect ground state, *Phys. Rev. B* 100 (14) (2019) 140104.
- [27] Y Nahas, S Prokhorenko, J Fischer, B Xu, C Carrétéro, S Prosandeev, M Bibes, S Fusil, B Dkhil, V Garcia, et al., Inverse transition of labyrinthine domain patterns in ferroelectric thin films, *Nature* 577 (7788) (2020) 47–51.
- [28] Igor Lukyanchuk, Elena Zaitseva, Vitaly Levashenko, Miroslav Kvassay, Svitlana Kondovych, Yuri Tikhonov, Laurent Baudry, Anna Razumnaya, Ferroelectric multiple-valued logic units, *Ferroelectrics* 543 (1) (2019) 213–221.
- [29] M.G. Stachiotti, M. Sepiarsky, Toroidal ferroelectricity in PbTiO_3 nanoparticles, *Phys. Rev. Lett.* 106 (13) (2011) 137601.
- [30] John Mangeri, Yomery Espinal, Andrea Jokisaari, S Pamir Alpaly, Serge Nakhmanson, Olle Heinonen, Topological phase transformations and intrinsic size effects in ferroelectric nanoparticles, *Nanoscale* 9 (4) (2017) 1616–1624.
- [31] D Karpov, Z Liu, T dos Santos Rolo, R Harder, PV Balachandran, D Xue, T Lookman, E Fohntung, Three-dimensional imaging of vortex structure in a ferroelectric nanoparticle driven by an electric field, *Nature Commun.* 8 (1) (2017) 280.
- [32] F. Di Rino, M. Sepiarsky, M.G. Stachiotti, Topology of the polarization field in PbTiO_3 nanoparticles of different shapes by atomic-level simulations, *J. Appl. Phys.* 127 (14) (2020) 144101.
- [33] S. Prosandeev, L. Bellaiche, Characteristics and signatures of dipole vortices in ferroelectric nanodots: First-principles-based simulations and analytical expressions, *Phys. Rev. B* 75 (9) (2007) 094102.
- [34] Pierre-William Martelli, Séraphin M Mefire, Igor A Luk'yanchuk, Multidomain switching in the ferroelectric nanodots, *EPL (Eur. Lett.)* 111 (5) (2015) 50001.
- [35] Zhongwen Li, Yujia Wang, Guo Tian, Peilian Li, Lina Zhao, Fengyuan Zhang, Junxiang Yao, Hua Fan, Xiao Song, Deyang Chen, et al., High-density array of ferroelectric nanodots with robust and reversibly switchable topological domain states, *Sci. Adv.* 3 (8) (2017) e1700919.
- [36] Zhongwen Li, Siyi Zhang, Xiaofen Li, Yangjiang Wu, Haiou Wang, Hao Liu, Center-type topological domain states in ferroelectric nanodots tailored from thin films, *Phys. Status Solidi Rapid Res. Lett.* 17 (4) (2023) 2200424.
- [37] Ivan I. Naumov, L. Bellaiche, Huaxiang Fu, Unusual phase transitions in ferroelectric nanodisks and nanorods, *Nature* 432 (7018) (2004) 737.
- [38] L. Lahoche, I. Luk'yanchuk, G. Pascoli, Stability of vortex phases in ferroelectric easy-plane nano-cylinders, *Integr. Ferroelectr.* 99 (1) (2008) 60–66.
- [39] Anna N Morozovska, Riccardo Hertel, Salia Cherifi-Hertel, Victor Yu Reshetnyak, Eugene A Eliseev, Dean R Evans, Chiral polarization textures induced by the flexoelectric effect in ferroelectric nanocylinders, *Phys. Rev. B* 104 (5) (2021) 054118.
- [40] Maksim A Pavlenko, Franco Di Rino, Leo Boron, Svitlana Kondovych, Anaïs Sené, Yuri A Tikhonov, Anna G Razumnaya, Valerii M Vinokur, Marcelo Sepiarsky, Igor A Lukyanchuk, Phase diagram of a strained ferroelectric nanowire, *Crystals* 12 (4) (2022) 453.
- [41] Svitlana Kondovych, Maksim Pavlenko, Yurii Tikhonov, Anna Razumnaya, Igor Lukyanchuk, Vortex states in a PbTiO_3 ferroelectric cylinder, *SciPost Phys.* 14 (3) (2023) 056.
- [42] Yue Zheng, W.J. Chen, Characteristics and controllability of vortices in ferromagnetics, ferroelectrics, and multiferroics, *Rep. Progr. Phys.* 80 (8) (2017) 086501.
- [43] Sujit Das, Anirban Ghosh, Margaret R McCarter, Shang-Lin Hsu, Yun-Long Tang, Anoop R Damodaran, R Ramesh, Lane W Martin, Perspective: Emergent topologies in oxide superlattices, *APL Mater.* 6 (10) (2018) 100901.
- [44] Ramamoorthy Ramesh, Darrell G. Schlom, Creating emergent phenomena in oxide superlattices, *Nat. Rev. Mater.* 4 (4) (2019) 257–268.
- [45] G. Tian, W.D. Yang, X.S. Gao, J.-M. Liu, Emerging phenomena from exotic ferroelectric topological states, *APL Mater.* 9 (2) (2021) 020907.
- [46] Congbing Tan, Yongqi Dong, Yuanwei Sun, Chang Liu, Pan Chen, Xiangli Zhong, Ruixue Zhu, Mingwei Liu, Jingmin Zhang, Jinbin Wang, et al., Engineering polar vortex from topologically trivial domain architecture, *Nature Commun.* 12 (1) (2021) 1–8.
- [47] Shanquan Chen, Shuai Yuan, Zhipeng Hou, Yunlong Tang, Jinping Zhang, Tao Wang, Kang Li, Weiwei Zhao, Xingjun Liu, Lang Chen, et al., Recent progress on topological structures in ferroic thin films and heterostructures, *Adv. Mater.* 33 (6) (2021) 2000857.
- [48] Xiangwei Guo, Linming Zhou, Basanta Roul, Yongjun Wu, Yuhui Huang, Sujit Das, Zijian Hong, Theoretical understanding of polar topological phase transitions in functional oxide heterostructures: A review, *Small Methods* 6 (9) (2022) 2200486.
- [49] Javier Junquera, Yousra Nahas, Sergei Prokhorenko, Laurent Bellaiche, Jorge Íñiguez, Darrel G Schlom, Long-Qing Chen, Sayeef Salahuddin, David A Muller, Lane W Martin, R Ramesh, Topological phases in polar oxide nanostructures, *Rev. Modern Phys.* 95 (2) (2023) 025001.
- [50] Y.J. Wang, Y.L. Tang, Y.L. Zhu, X.L. Ma, Entangled polarizations in ferroelectrics: A focused review of polar topologies, *Acta Mater.* 243 (2023) 118485.
- [51] Igor Luk'yanchuk, Anna Razumnaya, Svitlana Kondovych, Yurii Tikhonov, Valerii M Vinokur, Topological ferroelectric chirality, 2024, arXiv preprint arXiv:2406.19728.
- [52] Vladimir I. Arnold, Boris A. Khesin, *Topological Methods in Hydrodynamics*, vol. 125, Springer Science & Business Media, 2021.
- [53] Jacques Friedel, *Dislocations: International Series of Monographs on Solid State Physics*, vol. 3, Elsevier, 2013.
- [54] Pierre-Gilles De Gennes, Jacques Prost, *The Physics of Liquid Crystals*, Oxford University Press, 1993.
- [55] Maurice Kleman, Oleg D. Lavrentovich, *Soft Matter Physics: an Introduction*, Springer, 2003.
- [56] Grigory E. Volovik, *The Universe in a Helium Droplet*, vol. 117, OUP Oxford, 2003.

- [57] G.E. Volovik, V.P. Mineev, Investigation of singularities in superfluid ^3He and liquid crystals by homotopic topology methods, *Zh. Eksp. Teor. Fiz.* 72 (6) (1977) 2256–2274.
- [58] N. David Mermin, The topological theory of defects in ordered media, *Rev. Modern Phys.* 51 (3) (1979) 591.
- [59] Boris A Dubrovin, Anatolij T Fomenko, Sergei Petrovich Novikov, *Modern Geometry – Methods and Applications: Part II: The Geometry and Topology of Manifolds*, vol. 104, Springer Science & Business Media, 2012.
- [60] Philip McCord Morse, Herman Feshbach, *Methods of Theoretical Physics*, Technology Press, 1946.
- [61] Harsh Bhatia, Gregory Norgard, Valerio Pascucci, Peer-Timo Bremer, The Helmholtz-Hodge decomposition – a survey, *IEEE Trans. Vis. Comput. Graphics* 19 (8) (2012) 1386–1404.
- [62] Vladimir Igorevich Arnold, *Geometrical Methods in the Theory of Ordinary Differential Equations*, vol. 250, Springer Science & Business Media, 2012.
- [63] Russel Caflisch, George C. Papanicolaou, *Singularities in Fluids, Plasmas and Optics*, vol. 404, Springer Science & Business Media, 2012.
- [64] Ernst Feldtkeller, Mikromagnetisch stetige und unstetige magnetisierungskonfigurationen, *Z. Angew. Phys.* 19 (6) (1965) 530.
- [65] W. Döring, Point singularities in micromagnetism, *J. Appl. Phys.* 39 (2) (1968) 1006–1007.
- [66] E.G. Galkina, B.A. Ivanov, V.A. Stephanovich, Phenomenological theory of Bloch point relaxation, *J. Magn. Magn. Mater.* 118 (3) (1993) 373–378.
- [67] Peter Milde, Denny Köhler, Joachim Seidel, LM Eng, Andreas Bauer, Alfonso Chacon, Jonas Kindervater, Sebastian Mühlbauer, Christian Pfleiderer, Stefan Bührandt, et al., Unwinding of a skyrmion lattice by magnetic monopoles, *Science* 340 (6136) (2013) 1076–1080.
- [68] Sandrine Da Col, Ségolène Jamet, Nicolas Rougemaille, Andrea Locatelli, Tevfik Onur Montes, B Santos Burgos, Raja Afid, Michael Darques, Laurent Cagnon, Jean-Christophe Toussaint, et al., Observation of Bloch-point domain walls in cylindrical magnetic nanowires, *Phys. Rev. B* 89 (18) (2014) 180405.
- [69] Mi-Young Im, Hee-Sung Han, Min-Seung Jung, Young-Sang Yu, Sooseok Lee, Seongsoo Yoon, Weilun Chao, Peter Fischer, Jung-Il Hong, Ki-Suk Lee, Dynamics of the Bloch point in an asymmetric permalloy disk, *Nature Commun.* 10 (1) (2019) 593.
- [70] Marijan Beg, Ryan A Pepper, David Cortés-Ortuño, Bilal Atie, Marc-Antonio Bisotti, Gary Downing, Thomas Kluyver, Ondrej Hovorka, Hans Fangohr, Stable and manipulable Bloch point, *Sci. Rep.* 9 (1) (2019) 7959.
- [71] F Tejo, R Hernández Heredero, O Chubykalo-Fesenko, KY Guslienko, The Bloch point 3D topological charge induced by the magnetostatic interaction, *Sci. Rep.* 11 (1) (2021) 21714.
- [72] Guidobeth Sáez, Eduardo Saavedra, Nicolás Vidal-Silva, Juan Escrig, Eugenio E Vogel, Dynamic susceptibility of a Bloch point singularity confined in a magnetic nanowire, *Results Phys.* 37 (2022) 105530.
- [73] Guidobeth Sáez, Pablo Díaz, Nicolás Vidal-Silva, Juan Escrig, Eugenio E Vogel, Bloch points stabilization by means of diameter modulations in cylindrical nanowires, *Results Phys.* 39 (2022) 105768.
- [74] Diego Caso, Pablo Tuero, Javier García, Konstantin Y Guslienko, Farkhad G Aliev, Dynamics and reversible control of the Bloch-point vortex domain wall in short cylindrical magnetic nanowires, *Phys. Rev. Appl.* 19 (6) (2023) 064030.
- [75] F Tejo, C Zambrano-Rabanal, VL Carvalho-Santos, N Vidal-Silva, Bloch point nanospheres for the design of magnetic traps, *Appl. Phys. Lett.* 123 (10) (2023).
- [76] Cristobal Zambrano-Rabanal, Boris Valderrama, Felipe Tejo, Ricardo Gabriel Elías, Alvaro S Nunez, Vagson L Carvalho-Santos, Nicolás Vidal-Silva, Magnetostatic interaction between Bloch point nanospheres, *Sci. Rep.* 13 (1) (2023) 7171.
- [77] OA Tretiakov, D Clarke, Gia-Wei Chern, Ya B Bazaliy, O Tchernyshyov, Dynamics of domain walls in magnetic nanostrips, *Phys. Rev. Lett.* 100 (12) (2008) 127204.
- [78] E.K.H. Salje, J.F. Scott, Ferroelectric Bloch-line switching: A paradigm for memory devices? *Appl. Phys. Lett.* 105 (25) (2014) 252904.
- [79] Anna N Morozovska, Eugene A Eliseev, Riccardo Hertel, Yevhen M Fomichov, Viktoriia Tulaidan, Victor Yu Reshetnyak, Dean R Evans, Electric field control of three-dimensional vortex states in core-shell ferroelectric nanoparticles, *Acta Mater.* 200 (2020) 256–273.
- [80] Yurii Tikhonov, Jesi R Maguire, Conor J McCluskey, James PV McConville, Amit Kumar, Haidong Lu, Dennis Meier, Anna Razumnaya, John Martin Gregg, Alexei Gruverman, et al., Polarization topology at the nominally charged domain walls in uniaxial ferroelectrics, *Adv. Mater.* 34 (45) (2022) 2203028.
- [81] Yu-Jia Wang, Yan-Peng Feng, Yun-Long Tang, Yin-Lian Zhu, Yi Cao, Min-Jie Zou, Wan-Rong Geng, Xiu-Liang Ma, Polar Bloch points in strained ferroelectric films, *Nature Commun.* 15 (1) (2024) 3949.
- [82] Lingyuan Gao, Sergei Prokhorenko, Yousra Nahas, Laurent Bellaiche, Dynamical control of topology in polar skyrmions via twisted light, *Phys. Rev. Lett.* 132 (2) (2024) 026902.
- [83] N. David Mermin, E pluribus boojum: the physicist as neologist, *Phys. Today* 34 (4) (1981) 46–53.
- [84] G.E. Volovik, O.D. Lavrentovich, Topological dynamics of defects: boojums in nematic drops, *Zh. Eksp. Teor. Fiz.* 85 (6) (1983) 1997–2010.
- [85] L.D. Faddeev, Some comments on the many-dimensional solitons, *Lett. Math. Phys.* 1 (4) (1976) 289–293.
- [86] A.A. Thiele, Steady-state motion of magnetic domains, *Phys. Rev. Lett.* 30 (6) (1973) 230.
- [87] Alexis P. Malozemoff, John C. Slonczewski, *Magnetic Domain Walls in Bubble Materials: Advances in Materials and Device Research*, vol. 1, Academic Press, 2013.
- [88] K.Y. Guslienko, Gauge and emergent electromagnetic fields for moving magnetic topological solitons, *EPL (Eur. Lett.)* 113 (6) (2016) 67002.
- [89] Jladomyr Kravchuk, *Problems in micromagnetism*, 2023, <http://dx.doi.org/10.13140/RG.2.2.22653.74728>.
- [90] Henri Poincaré, Sur les courbes définies par les équations différentielles, *J. Math. Pures Appl.* 1 (1885) 167–244.
- [91] H. Hopf, Über die Abbildungen der dreidimensionalen Sphäre auf die Kugelfläche, *Math. Ann.* 104 (1931) 637–665.
- [92] Tian Ma, Shouhong Wang, A generalized Poincaré-Hopf index formula and its applications to 2-D incompressible flows, *Nonlinear Anal. Real World Appl.* 2 (2001) 467–482.
- [93] Liviu I. Nicolaescu, *Lectures on the Geometry of Manifolds*, World Scientific, 2020.
- [94] Oleg Tchernyshyov, Gia-Wei Chern, Fractional vortices and composite domain walls in flat nanomagnets, *Phys. Rev. Lett.* 95 (19) (2005) 197204.
- [95] Daniel Henry Gottlieb, Vector fields and classical theorems of topology, *Milan J. Math.* 1 (1990) 1–11.
- [96] Hiroaki Kamae, Masayuki Yamasaki, Local indices of a vector field at an isolated zero on the boundary, 2008, arXiv preprint arXiv:0803.2139.
- [97] G.E. Volovik, Topological singularities on the surface of an ordered system, *JETP Lett.* 28 (1978) 59–63.
- [98] Vladimir P. Mineev, *Topologically Stable Defects and Solitons in Ordered Media*, vol. 1, CRC Press, 1998.
- [99] Vladimir I. Arnold, Indices of singular points of 1-forms on a manifold with boundary, convolution of invariants of reflection groups, and singular projections of smooth surfaces, *Russian Math. Surveys* 34 (2) (1979) 1.
- [100] Jiadong Zang, Vincent Cros, Axel Hoffmann, *Topology in Magnetism*, vol. 192, Springer, 2018.
- [101] Sebastian Mühlbauer, Benedikt Binz, Florian Jonietz, Christian Pfleiderer, Achim Rosch, Anja Neubauer, Robert Georgii, Peter Böni, Skyrmion lattice in a chiral magnet, *Science* 323 (5916) (2009) 915–919.
- [102] Naoto Nagaosa, Yoshinori Tokura, Topological properties and dynamics of magnetic skyrmions, *Nat. Nanotechnol.* 8 (12) (2013) 899–911.
- [103] Joseph Barker, Oleg A. Tretiakov, Static and dynamical properties of antiferromagnetic skyrmions in the presence of applied current and temperature, *Phys. Rev. Lett.* 116 (14) (2016) 147203.

- [104] Kai Litzius, Ivan Lemesh, Benjamin Krüger, Pedram Bassirian, Lucas Caretta, Kornel Richter, Felix Büttner, Koji Sato, Oleg A Tretiakov, Johannes Förster, et al., Skyrmion hall effect revealed by direct time-resolved X-ray microscopy, *Nat. Phys.* 13 (2) (2017) 170–175.
- [105] Albert Fert, Nicolas Reyren, Vincent Cros, Magnetic skyrmions: advances in physics and potential applications, *Nat. Rev. Mater.* 2 (7) (2017) 1–15.
- [106] Shilei Zhang, *Chiral and Topological Nature of Magnetic Skyrmions*, Springer, 2018.
- [107] Borge Göbel, Ingrid Mertig, Oleg A. Tretiakov, Beyond skyrmions: Review and perspectives of alternative magnetic quasiparticles, *Phys. Rep.* 895 (2021) 1–28.
- [108] Xichao Zhang, Jing Xia, Oleg A Tretiakov, Motohiko Ezawa, Guoping Zhao, Yan Zhou, Xiaoxi Liu, Masahito Mochizuki, Chiral skyrmions interacting with chiral flowers, *Nano Lett.* 23 (24) (2023) 11793–11801.
- [109] O.A. Tretiakov, O. Tchernyshyov, Vortices in thin ferromagnetic films and the skyrmion number, *Phys. Rev. B* 75 (1) (2007) 012408.
- [110] Y.A. Kharkov, O.P. Sushkov, M. Mostovoy, Bound states of skyrmions and merons near the Lifshitz point, *Phys. Rev. Lett.* 119 (20) (2017) 207201.
- [111] Borge Göbel, Alexander Mook, Jürgen Henk, Ingrid Mertig, Oleg A Tretiakov, Magnetic bimerons as skyrmion analogues in in-plane magnets, *Phys. Rev. B* 99 (6) (2019) 060407.
- [112] Kentaro Ohara, Xichao Zhang, Yinling Chen, Satoshi Kato, Jing Xia, Motohiko Ezawa, Oleg A Tretiakov, Zhipeng Hou, Yan Zhou, Guoping Zhao, et al., Reversible transformation between isolated skyrmions and bimerons, *Nano Lett.* 22 (21) (2022) 8559–8566.
- [113] Xiuzhen Yu, Naoya Kanazawa, Xichao Zhang, Yoshio Takahashi, Konstantin V Iakoubovskii, Kiyomi Nakajima, Toshiaki Tanigaki, Masahito Mochizuki, Yoshinori Tokura, Spontaneous vortex-antivortex pairs and their topological transitions in a chiral-lattice magnet, *Adv. Mater.* 36 (1) (2024) 2306441.
- [114] Hyun Soon Park, Xiuzhen Yu, Shinji Aizawa, Toshiaki Tanigaki, Tetsuya Akashi, Yoshio Takahashi, Tsuyoshi Matsuda, Naoya Kanazawa, Yoshinori Onose, Daisuke Shindo, et al., Observation of the magnetic flux and three-dimensional structure of skyrmion lattices by electron holography, *Nature Nanotechnol.* 9 (5) (2014) 337–342.
- [115] Fumitaka Kagawa, Hiroshi Oike, Wataru Koshibae, Akiko Kikkawa, Yoshihiro Okamura, Yasujiro Taguchi, Naoto Nagaosa, Yoshinori Tokura, Current-induced viscoelastic topological unwinding of metastable skyrmion strings, *Nature Commun.* 8 (1) (2017) 1332.
- [116] MT Birch, D Cortés-Ortuño, LA Turnbull, MN Wilson, F Groß, N Träger, A Laurensen, N Bukin, SH Moody, M Weigand, et al., Real-space imaging of confined magnetic skyrmion tubes, *Nature Commun.* 11 (1) (2020) 1726.
- [117] Volodymyr P. Kravchuk, Nonlinear dynamics of skyrmion strings, *Phys. Rev. B* 108 (14) (2023) 144412.
- [118] Kejing Ran, Wancong Tan, Xinyu Sun, Yizhou Liu, Robert M Dalglish, Nina-Juliane Steinke, Gerrit van der Laan, Sean Langridge, Thorsten Hesjedal, Shilei Zhang, Bending skyrmion strings under two-dimensional thermal gradients, *Nature Commun.* 15 (1) (2024) 4860.
- [119] N.R. Cooper, Propagating magnetic vortex rings in ferromagnets, *Phys. Rev. Lett.* 82 (7) (1999) 1554.
- [120] Paul Sutcliffe, Knots in the Skyrme–Faddeev model, *Proc. R. Soc. A: Math. Phys. Eng. Sci.* 463 (2087) (2007) 3001–3020.
- [121] Aleksandr Borisovich Borisov, F.N. Rybakov, Dynamical toroidal hopfions in a ferromagnet with easy-axis anisotropy, *JETP Lett.* 90 (2009) 544–547.
- [122] Robert Voinescu, Jung-Shen B. Tai, Ivan I. Smalyukh, Hopf solitons in helical and conical backgrounds of chiral magnetic solids, *Phys. Rev. Lett.* 125 (5) (2020) 057201.
- [123] Yizhou Liu, Hikaru Watanabe, Naoto Nagaosa, Emergent magnetomultipoles and nonlinear responses of a magnetic hopfion, *Phys. Rev. Lett.* 129 (26) (2022) 267201.
- [124] Philipp N Rybakov, Nikolai S Kiselev, Aleksandr B Borisov, Lukas Döring, Christof Melcher, Stefan Blügel, Magnetic hopfions in solids, *APL Mater.* 10 (11) (2022) 111113.
- [125] Moritz Sallermann, Hannes Jónsson, Stefan Blügel, Stability of hopfions in bulk magnets with competing exchange interactions, *Phys. Rev. B* 107 (10) (2023) 104404.
- [126] Konstantin Y. Guslienko, Emergent magnetic field and vector potential of the toroidal magnetic hopfions, *Chaos Solit. Fractals* 174 (2023) 113840.
- [127] Fengshan Zheng, Nikolai S Kiselev, Philipp N Rybakov, Luyan Yang, Wen Shi, Stefan Blügel, Rafal E Dunin-Borkowski, Hopfion rings in a cubic chiral magnet, *Nature* 623 (7988) (2023) 718–723.
- [128] Konstantin Guslienko, Magnetic hopfions: A review, *Magnetism* 4 (4) (2024) 383–399.
- [129] Ross Knapman, Timon Tausendpfund, Sebastián A Díaz, Karin Everschor-Sitte, Spacetime magnetic hopfions from internal excitations and braiding of skyrmions, *Commun. Phys.* 7 (1) (2024) 151.
- [130] JHC Whitehead, An expression of Hopf's invariant as an integral, *Proc. Natl. Acad. Sci.* 33 (5) (1947) 117–123.
- [131] Frank Wilczek, Anthony Zee, Linking numbers, spin, and statistics of solitons, *Phys. Rev. Lett.* 51 (25) (1983) 2250.
- [132] Lev Davidovich Landau, L.P. Pitaevskii, E.M. Lifshitz, *Electrodynamics of Continuous Media*, Elsevier, 2013.
- [133] Boris A. Strukov, Arkadi P. Levanyuk, *Ferroelectric Phenomena in Crystals: Physical Foundations*, Springer, Berlin, 2012.
- [134] Karin M. Rabe, Charles H. Ahn, Jean-Marc Triscone, *Physics of Ferroelectrics: A Modern Perspective*, Springer Berlin Heidelberg, 2007.
- [135] Bo Wang, Yijia Gu, Shujun Zhang, Long-Qing Chen, *Flexoelectricity in solids: Progress, challenges, and perspectives*, *Prog. Mater. Sci.* 106 (2019) 100570.
- [136] Wanfeng Zhou, Pan Chen, Baojin Chu, Flexoelectricity in ferroelectric materials, *IET Nanodielectr.* 2 (3) (2019) 83–91.
- [137] Pavel Mokry, Tomáš Sluka, Identification of defect distribution at ferroelectric domain walls from evolution of nonlinear dielectric response during the aging process, *Phys. Rev. B* 93 (2016) 064114.
- [138] T. Mitsui, S. Nomura, *Ferroelectrics and Related Substances*, subvolume a: Oxides, in *Landolt-Bornstein Numerical Data and Functional Relationships*, vol. 16, Springer, Berlin, Heidelberg, and New York, 1981.
- [139] Charles Kittel, Theory of the structure of ferromagnetic domains in films and small particles, *Phys. Rev.* 70 (11–12) (1946) 965.
- [140] F. De Guerville, I. Lukyanchuk, L. Lahoche, M. El Marssi, Modeling of ferroelectric domains in thin films and superlattices, *Mater. Sci. Eng. B* 120 (1–3) (2005) 16–20.
- [141] Igor A. Lukyanchuk, Laurent Lahoche, Anaïs Sené, Universal properties of ferroelectric domains, *Phys. Rev. Lett.* 102 (14) (2009) 147601.
- [142] I Lukyanchuk, A Razumnaya, Anaïs Sené, Y Tikhonov, VM Vinokur, The ferroelectric field-effect transistor with negative capacitance, *Npj Comput. Mater.* 8 (1) (2022) 1–8.
- [143] Robert M. White, Robert M. White, Bradford Bayne, *Quantum Theory of Magnetism*, vol. 1, Springer, 1983.
- [144] Seonghoon Woo, Kai Litzius, Benjamin Krüger, Mi-Young Im, Lucas Caretta, Kornel Richter, Maxwell Mann, Andrea Krone, Robert M Reeve, Markus Weigand, et al., Observation of room-temperature magnetic skyrmions and their current-driven dynamics in ultrathin metallic ferromagnets, *Nature Mater.* 15 (5) (2016) 501–506.
- [145] Ivan Lemesh, Felix Büttner, Geoffrey S.D. Beach, Accurate model of the stripe domain phase of perpendicularly magnetized multilayers, *Phys. Rev. B* 95 (17) (2017) 174423.
- [146] Felix Büttner, Ivan Lemesh, Geoffrey S.D. Beach, Theory of isolated magnetic skyrmions: From fundamentals to room temperature applications, *Sci. Rep.* 8 (1) (2018) 1–12.

- [147] Jörg Schöpf, Arsha Thampi, Peter Milde, Dmytro Ivaneyko, Svitlana Kondovych, Denys Y Kononenko, Lukas M Eng, Lei Jin, Lin Yang, Lena Wysocki, et al., Néel skyrmion bubbles in $\text{La}_{0.7}\text{Sr}_{0.3}\text{Mn}_{1-x}\text{Ru}_x\text{O}_3$ multilayers, *Nano Lett.* 23 (8) (2023) 3532–3539.
- [148] Anne Bernand-Mantel, Lorenzo Camosi, Alexis Wartelle, Nicolas Rougemaille, Michaël Darques, Laurent Ranno, The skyrmion-bubble transition in a ferromagnetic thin film, *SciPost Phys.* 4 (5) (2018) 027.
- [149] Marine Schott, Anne Bernand-Mantel, Laurent Ranno, Stefania Pizzini, Jan Vogel, Hélène Béa, Claire Baraduc, Stéphane Auffret, Gilles Gaudin, Dominique Givord, The skyrmion switch: turning magnetic skyrmion bubbles on and off with an electric field, *Nano Lett.* 17 (5) (2017) 3006–3012.
- [150] Yuan Yao, Bei Ding, Jinjing Liang, Hang Li, Xi Shen, Richeng Yu, Wenhong Wang, Chirality flips of skyrmion bubbles, *Nature Commun.* 13 (1) (2022) 5991.
- [151] Claire Donnelly, Konstantin L. Metlov, Valerio Scagnoli, Manuel Guizar-Sicairos, Mirko Holler, Nicholas S Bingham, Jörg Raabe, Laura J Heyderman, Nigel R Cooper, Sebastian Gliga, Experimental observation of vortex rings in a bulk magnet, *Nat. Phys.* 17 (3) (2021) 316–321.
- [152] Lev Davidovich Landau, Evgenii Mikhailovich Lifshitz, *Fluid Mechanics*, vol. 6, Elsevier, 1987.
- [153] John B. Etnyre, Robert Christ, Contact topology and hydrodynamics II: solid tori, *Ergod. Theory Dyn. Syst.* 22 (1999) 819–833.
- [154] Alberto Enciso, Daniel Peralta-Salas, Knots and links in steady solutions of the Euler equation, *Ann. Math.* 175 (2012) 345–367.
- [155] Alberto Enciso, Daniel Peralta-Salas, Existence of knotted vortex tubes in steady Euler flows, *Acta Math.* 214 (1) (2015) 61–134.
- [156] Vladimir Arnold, Sur la géométrie différentielle des groupes de Lie de dimension infinie et ses applications à l'hydrodynamique des fluides parfaits, in: *Annales de l'institut Fourier*, vol. 16, (1) 1966, pp. 319–361.
- [157] James F Scott, Donald M Evans, J Marty Gregg, Alexei Gruverman, Hydrodynamics of domain walls in ferroelectrics and multiferroics: Impact on memory devices, *Appl. Phys. Lett.* 109 (4) (2016).
- [158] James F Scott, Donald M Evans, Miryam Arredondo-Arechavala, Ram S Katiyar, Raymond GP McQuaid, J Marty Gregg, Nonequilibrium ferroelectric-ferroelastic 10 nm nanodomains: wrinkles, period-doubling, and power-law relaxation, *J. Condens. Matter Phys.* 29 (30) (2017) 304001.
- [159] Oscar P. Bruno, Peter Laurence, Existence of three-dimensional toroidal MHD equilibria with nonconstant pressure, *Comm. Pure Appl. Math.* 49 (7) (1996) 717–764.
- [160] Chong-Qing Cheng, Yi-Sui Sun, Existence of invariant tori in three-dimensional measure-preserving mappings, *Celest. Mech. Dyn. Astron.* 47 (1990) 275–292.
- [161] Boris Khesin, Sergei Kuksin, Daniel Peralta-Salas, KAM theory and the 3D Euler equation, *Adv. Math.* 267 (2014) 498–522.
- [162] Henry Keith Moffatt, G.M. Zaslavsky, P. Comte, M. Tabor, *Topological Aspects of the Dynamics of Fluids and Plasmas*, vol. 218, Springer Science & Business Media, 1992.
- [163] Vladimir I. Arnold, The asymptotic hopf invariant and its applications, in: *Proc. Summer School in Diff. Equations at Dilizhan*, 1973, Erevan; *Sel. Math. Sov.*, vol. 5, 1986, pp. 327–345.
- [164] Vivasha Govinden, Sergei Prokhorenko, Qi Zhang, Suyash Rijal, Yousra Nahas, Laurent Bellaiche, Nagarajan Valanoor, Spherical ferroelectric solitons, *Nature Mater.* 22 (5) (2023) 553–561.
- [165] Le Van Lich, Ha Thi Dang, Van-Hai Dinh, Polar toron structure in ferroelectric core-shell nanoparticles, *Scr. Mater.* 236 (2023) 115641.
- [166] Ia B. Zel'dovich, Electromagnetic interaction with parity violation, *J. Exp. Theor. Phys.* 33 (1957) 1531–1533.
- [167] Subrahmanyam Chandrasekhar, *Hydrodynamic and Hydromagnetic Stability*, Courier Corporation, 2013.
- [168] Stephen F. Mason, Origins of biomolecular handedness, *Nature* 311 (5981) (1984) 19–23.
- [169] Michael Monastyrsky, *Topology in Molecular Biology*, Springer, 2007.
- [170] Roger A. Hegstrom, Dilip K. Kondepudi, The handedness of the universe, *Sci. Am.* 262 (1) (1990) 108–115.
- [171] Georges H. Wagnière, *On Chirality and the Universal Asymmetry: Reflections on Image and Mirror Image*, John Wiley & Sons, 2008.
- [172] Anthony Zee, *Quantum Field Theory in a Nutshell*, Princeton University Press, 2010.
- [173] Igor Luk'yanchuk, Valerii M. Vinokur, Dynamics of polarization vortices revealed in a ferroelectric material, *Nature* 592 (7854) (2021) 359–360.
- [174] Igor Lukyanchuk, Yurii Tikhonov, Anna Razumnaya, Valery Vinokour, Thermal and electromagnetic generation and switching of chirality in ferroelectrics, 2021, European Patent App. 21199906.5.
- [175] Piush Behera, Molly A May, Fernando Gómez-Ortiz, Sandhya Susarla, Sujit Das, Christopher T Nelson, Lucas Caretta, Shang-Lin Hsu, Margaret R McCarter, Benjamin H Savitzky, et al., Electric field control of chirality, *Sci. Adv.* 8 (1) (2022) eabj8030.
- [176] Jing Wang, Deshan Liang, Jing Ma, Yuanyuan Fan, Ji Ma, Hasnain Mehdi Jafri, Huayu Yang, Qinghua Zhang, Yue Wang, Changqing Guo, et al., Polar solomon rings in ferroelectric nanocrystals, *Nature Commun.* 14 (1) (2023) 3941.
- [177] Bo Xu, Zhanpeng Gong, Jingran Liu, Yunfei Hong, Yang Yang, Lou Li, Yilun Liu, Junkai Deng, Jefferson Zhe Liu, Tunable ferroelectric topological defects on 2D topological surfaces: Complex strain engineering skyrmion-like polar structures in 2D materials, *Adv. Funct. Mater.* (2024) 2311599.
- [178] Arthur Chaudron, Zixin Li, Aurore Finco, Pavel Marton, Pauline Dufour, Amr Abdelsamie, Johanna Fischer, Sophie Collin, Brahim Dkhil, Jirka Hlinka, et al., Electric-field-induced multiferroic topological solitons, *Nature Mater.* 23 (2024) 905–911.
- [179] Bo Ruan, Pengcheng Xiong, Qingyuan Liu, Ye Ji, Shuai Yuan, Collective control of a vortex array in a ferroelectric ultrathin film, *Appl. Phys. Lett.* 124 (20) (2024).
- [180] Jianhua Ren, Linjie Liu, Fei Sun, Qian He, Mengjun Wu, Weijin Chen, Yue Zheng, Stabilization and control of weakly correlated polar skyrmions in ferroelectric thin films, *Acta Mater.* 276 (2024) 120154.
- [181] Haojie Han, Wei Li, Qinghua Zhang, Shiyu Tang, Yue Wang, Zongqi Xu, Yiqun Liu, Hetian Chen, Jingkun Gu, Jing Wang, et al., Electric field-manipulated optical chirality in ferroelectric vortex domains, *Adv. Mater.* (2024) 2408400.
- [182] Gerald Teschl, *Ordinary Differential Equations and Dynamical Systems*, vol. 140, American Mathematical Society, 2024.
- [183] Evgenii A. Kuznetsov, Aleksandr V. Mikhailov, On the topological meaning of canonical clebsch variables, *Phys. Lett. A* 77 (1) (1980) 37–38.
- [184] H.K. Moffatt, The degree of knottedness of tangled vortex lines, *J. Fluid Mech.* 35 (1) (1969) 117–129.
- [185] Martin W Scheeler, Dustin Kleckner, Davide Proment, Gordon L Kindlmann, William TM Irvine, Helicity conservation by flow across scales in reconnecting vortex links and knots, *Proc. Nat. Acad. Sci.* 111 (43) (2014) 15350–15355.
- [186] Yuki Kawaguchi, Muneto Nitta, Masahito Ueda, Knots in a spinor Bose-Einstein condensate, *Phys. Rev. Lett.* 100 (18) (2008) 180403.
- [187] David S Hall, Michael W Ray, Konstantin Tiurev, Emmi Ruokokoski, Andrei Horia Gheorghe, Mikko Möttönen, Tying quantum knots, *Nat. Phys.* 12 (5) (2016) 478–483.
- [188] Dustin Kleckner, Louis H. Kauffman, William T.M. Irvine, How superfluid vortex knots untie, *Nat. Phys.* 12 (7) (2016) 650–655.
- [189] Julien Garaud, Anatolii Korneev, Albert Samoilenko, Alexander Molochkov, Egor Babaev, Maxim Chernodub, Counterpart of the Chandrasekhar-Kendall state in noncentrosymmetric superconductors, *Phys. Rev. B* 108 (1) (2023) 014504.
- [190] Gianni Blatter, Mikhail V Feigel'man, Vadim B Geshkenbein, Anatoly I Larkin, Valerii M Vinokur, Vortices in high-temperature superconductors, *Rev. Modern Phys.* 66 (4) (1994) 1125.
- [191] Egor Babaev, Dual neutral variables and knot solitons in triplet superconductors, *Phys. Rev. Lett.* 88 (17) (2002) 177002.
- [192] A.M. Kamchatnov, Topological solitons in magnetohydrodynamics, *Zh. Eksp. Teor. Fiz.* 82 (1982) 117–124.
- [193] Antonio F. Ranada, A topological theory of the electromagnetic field, *Lett. Math. Phys.* 18 (1989) 97–106.

- [194] Atta Y.K. Chui, Henry Keith Moffatt, The energy and helicity of knotted magnetic flux tubes, *Proc. R. Soc. Lond. A: Math. Phys. Sci.* 451 (1943) (1995) 609–629.
- [195] William T.M. Irvine, Dirk Bouwmeester, Linked and knotted beams of light, *Nat. Phys.* 4 (9) (2008) 716–720.
- [196] Hridesh Kedia, Iwo Bialynicki-Birula, Daniel Peralta-Salas, William T.M. Irvine, Tying knots in light fields, *Phys. Rev. Lett.* 111 (15) (2013) 150404.
- [197] Amy Thompson, Joe Swearingin, Alexander Wickes, Dirk Bouwmeester, Constructing a class of topological solitons in magnetohydrodynamics, *Phys. Rev. E* 89 (4) (2014) 043104.
- [198] Manuel Arrayás, José L. Trueba, A class of non-null toroidal electromagnetic fields and its relation to the model of electromagnetic knots, *J. Phys. A* 48 (2) (2014) 025203.
- [199] Ludvig Faddeev, Antti J. Niemi, Stable knot-like structures in classical field theory, *Nature* 387 (6628) (1997) 58.
- [200] Richard A. Battye, Paul M. Sutcliffe, Solitons, links and knots, *Proc. R. Soc. Lond. A: Math. Phys. Eng. Sci.* 455 (1992) (1999) 4305–4331.
- [201] Uroš Tkalec, Miha Ravnik, Simon Čopar, Slobodan Žumer, Igor Muševič, Reconfigurable knots and links in chiral nematic colloids, *Science* 333 (6038) (2011) 62–65.
- [202] Angel Martínez, Miha Ravnik, Brice Lucero, Rayshan Visvanathan, Slobodan Žumer, Ivan I. Smalyukh, Mutually tangled colloidal knots and induced defect loops in nematic fields, *Nature Mater.* 13 (3) (2014) 258–263.
- [203] Jung-Shen B. Tai, Ivan I. Smalyukh, Three-dimensional crystals of adaptive knots, *Science* 365 (6460) (2019) 1449–1453.
- [204] Ivan I. Smalyukh, Knots and other new topological effects in liquid crystals and colloids, *Rep. Progr. Phys.* 83 (10) (2020) 106601.
- [205] Ye Yuan, Ivan I. Smalyukh, Chiral, topological, and knotted colloids in liquid crystals, *Crystals* 14 (10) (2024) 885.
- [206] Luca Tubiana, Gareth P. Alexander, Agnese Barbensi, Dorothy Buck, Julian H.E. Cartwright, Mateusz Chwastyk, Marek Cieplak, Ivan Coluzza, Simon Čopar, David J. Craik, et al., Topology in soft and biological matter, *Phys. Rep.* 1075 (2024) 1–137.
- [207] Boris Khesin, Nicolau C. Saldanha, Relative helicity and tiling twist, 2024, arXiv:2408.00522.
- [208] Bernard F. Schutz, *Geometrical Methods of Mathematical Physics*, Cambridge University Press, 1980.
- [209] Ajay K. Yadav, Kayla X. Nguyen, Zijian Hong, Pablo García-Fernández, Pablo Aguado-Puente, Christopher T. Nelson, Sujit Das, Bhagwati Prasad, Daewoong Kwon, Suraj Cheema, et al., Spatially resolved steady-state negative capacitance, *Nature* 565 (7740) (2019) 468–471.
- [210] C. Harnagea, A. Pignolet, Challenges in the analysis of the local piezoelectric response, in: *Nanoscale Characterisation of Ferroelectric Materials: Scanning Probe Microscopy Approach*, Springer, 2004, pp. 45–85.
- [211] Henry Keith Moffatt, Magnetic Field Generation in Electrically Conducting Fluids, in: *Cambridge Monogr. Mech. and Appl. Math.*, 1978.
- [212] Alessandra Celletti, Luigi Chierchia, *KAM Stability and Celestial Mechanics*, American Mathematical Society, 2007.
- [213] R.A. Cowley, S.N. Gvasaliya, S.G. Lushnikov, B. Roessli, G.M. Rotaru, Relaxing with relaxors: a review of relaxor ferroelectrics, *Adv. Phys.* 60 (2) (2011) 229–327.
- [214] Chang Won Ahn, Chang-Hyo Hong, Byung-Yul Choi, Hwang-Pill Kim, Hyoung-Su Han, Younghun Hwang, Wook Jo, Ke Wang, Jing-Feng Li, Jae-Shin Lee, et al., A brief review on relaxor ferroelectrics and selected issues in lead-free relaxors, *J. Korean Phys. Soc.* 68 (2016) 1481–1494.
- [215] H. Scott Dumas, *The KAM Story: A Friendly Introduction to The Content, History, And Significance Of Classical Kolmogorov-Arnold-Moser Theory*, World Scientific Publishing Company, 2014.
- [216] Vladimir Igorevich Arnol'd, *Mathematical Methods of Classical Mechanics*, vol. 60, Springer Science & Business Media, 2013.
- [217] Lu Lu, Yousra Nahas, Ming Liu, Hongchu Du, Zhijun Jiang, Shengping Ren, Dawei Wang, Lei Jin, Sergei Prokhorenko, Chun-Lin Jia, et al., Topological defects with distinct dipole configurations in $\text{PbTiO}_3/\text{SrTiO}_3$ multilayer films, *Phys. Rev. Lett.* 120 (17) (2018) 177601.
- [218] Pablo Aguado-Puente, Javier Junquera, Ferromagnetic-like closure domains in ferroelectric ultrathin films: First-principles simulations, *Phys. Rev. Lett.* 100 (17) (2008) 177601.
- [219] V.A. Stephanovich, I.A. Luk'yanchuk, M.G. Karkut, Domain-enhanced interlayer coupling in ferroelectric/paraelectric superlattices, *Phys. Rev. Lett.* 94 (4) (2005) 047601.
- [220] Vladimir M. Fridkin, *Photoferroelectrics*, vol. 9, Springer Science & Business Media, 2012.
- [221] Orlando Auciello, Carlos A. Paz de Araujo, Jolanta Celinska, Review of the science and technology for low-and high-density nonvolatile ferroelectric memories, in: *Emerging Non-Volatile Memories*, Springer, 2014, pp. 3–35.
- [222] A.M. Bratkovsky, A.P. Levanyuk, Continuous theory of ferroelectric states in ultrathin films with real electrodes, *J. Comput. Theor. Nanosci.* 6 (3) (2009) 465–489.
- [223] Svitlana Kondovych, Igor Luk'yanchuk, Tatyana I. Baturina, Valerii M. Vinokur, Gate-tunable electron interaction in high- κ dielectric films, *Sci. Rep.* 7 (1) (2017) 42770.
- [224] William M. Thorburn, The myth of Occam's razor, *Mind* 27 (107) (1918) 345–353.
- [225] S. Prosandeev, L. Bellaiche, Order parameter in complex dipolar structures: Microscopic modeling, *Phys. Rev. B* 77 (6) (2008) 060101.
- [226] John M. Finn, Thomas M. Antonsen, Jr., Magnetic helicity: what is it and what is it good for? *Comments Plasma Phys. Control. Fusion* 9 (1985) 111–126.
- [227] Padraic Shafer, Pablo García-Fernández, Pablo Aguado-Puente, Anoop R. Damodaran, Ajay K. Yadav, Christopher T. Nelson, Shang-Lin Hsu, Jacek C. Wojdeł, Jorge Iñiguez, Lane W. Martin, et al., Emergent chirality in the electric polarization texture of titanate superlattices, *Proc. Natl. Acad. Sci.* 115 (5) (2018) 915–920.
- [228] Neel Mackinnon, On the differences between helicity and chirality, *J. Opt.* 21 (12) (2019) 125402.
- [229] Zhe Zhao, Vincenzo Buscaglia, Massimo Viviani, Maria Teresa Buscaglia, Liliana Mitoseriu, Andrea Testino, Mats Nygren, Mats Johnsson, Paolo Nanni, Grain-size effects on the ferroelectric behavior of dense nanocrystalline BaTiO_3 ceramics, *Phys. Rev. B* 70 (2) (2004) 024107.
- [230] Emre Erdem, Hans-Christoph Semmelhack, Rolf Böttcher, Holger Rumpf, Juras Banys, Anke Matthes, Hans-Jürgen Gläsel, Dietmar Hirsch, Eberhard Hartmann, Study of the tetragonal-to-cubic phase transition in PbTiO_3 nanopowders, *J. Phys.: Condens. Matter.* 18 (15) (2006) 3861.
- [231] M.D. Glinchuk, A.V. Ragulya, V.A. Stephanovich, *Nanoferroics*, Springer, 2013.
- [232] Chaehwa Jeong, Juhyeok Lee, Hyesung Jo, Jaewhan Oh, Hionsuck Baik, Kyoung-June Go, Junwoo Son, Si-Young Choi, Sergey Prosandeev, Laurent Bellaiche, et al., Revealing the three-dimensional arrangement of polar topology in nanoparticles, *Nature Commun.* 15 (1) (2024) 3887.
- [233] Zhen Liu, Bin Yang, Wenwu Cao, Edwin Fohtung, Turab Lookman, Enhanced energy storage with polar vortices in ferroelectric nanocomposites, *Phys. Rev. Appl.* 8 (3) (2017) 034014.
- [234] Le Van Lich, Trong-Giang Nguyen, Van-Hai Dinh, Manh-Huong Phan, Theoretical studies on controlling the chirality of helical polarization vortices in ferroelectric nanowires: Implications for reconfigurable electronic devices, *ACS Appl. Nano Mater.* 5 (11) (2022) 16509–16518.
- [235] Per Martin Rørvik, Tor Grande, Mari-Ann Einarsrud, One-dimensional nanostructures of ferroelectric perovskites, *Adv. Mater.* 23 (35) (2011) 4007–4034.
- [236] Humin Cheng, Jiming Ma, Zhenguo Zhao, Di Qiang, Yongxiang Li, Xi Yao, Hydrothermal synthesis of acicular lead titanate fine powders, *J. Am. Chem. Soc.* 75 (5) (1992) 1123–1128.
- [237] F. Di Rino, I. Boron, M. Pavlenko, Y. Tikhonov, A. Razumnaya, M. Sepiarsky, A. Sené, I. Luk'yanchuk, S. Kondovych, Topological states in ferroelectric nanorods tuned by the surface tension, 2024, submitted for publication.
- [238] Sergey Prosandeev, Andrei Malashevich, Zhigang Gui, Lydie Louis, Raymond Walter, Ivo Souza, L. Bellaiche, Natural optical activity and its control by electric field in electrotoroidic systems, *Phys. Rev. B* 87 (19) (2013) 195111.

- [239] Arseni Goussev, Jonathan M Robbins, Valeriy Slastikov, Oleg A Tretiakov, Dzyaloshinskii-moriya domain walls in magnetic nanotubes, *Phys. Rev. B* 93 (5) (2016) 054418.
- [240] Ernst L. Koschmieder, *Bénard Cells and Taylor Vortices*, Cambridge University Press, 1993.
- [241] Pablo Aguado-Puente, Javier Junquera, Structural and energetic properties of domains in $\text{PbTiO}_3/\text{SrTiO}_3$ superlattices from first principles, *Phys. Rev. B* 85 (18) (2012) 184105.
- [242] Adeel Y Abid, Yuanwei Sun, Xu Hou, Congbing Tan, Xiangli Zhong, Ruixue Zhu, Haoyun Chen, Ke Qu, Yuehui Li, Mei Wu, et al., Creating polar antivortex in $\text{PbTiO}_3/\text{SrTiO}_3$ superlattice, *Nature Commun.* 12 (1) (2021) 2054.
- [243] Kairi Masuda, Lich Le Van, Takahiro Shimada, Takayuki Kitamura, Topological ferroelectric nanostructures induced by mechanical strain in strontium titanate, *Phys. Chem. Chem. Phys.* 21 (40) (2019) 22420–22428.